

University of Louisville

ThinkIR: The University of Louisville's Institutional Repository

Electronic Theses and Dissertations

8-2016

A non-invasive diagnostic system for early assessment of acute renal transplant rejection.

Mohamed Nazih Mohamed Ibrahim Shehata
University of Louisville

Follow this and additional works at: <https://ir.library.louisville.edu/etd>



Part of the [Electrical and Computer Engineering Commons](#)

Recommended Citation

Shehata, Mohamed Nazih Mohamed Ibrahim, "A non-invasive diagnostic system for early assessment of acute renal transplant rejection." (2016). *Electronic Theses and Dissertations*. Paper 2540.
<https://doi.org/10.18297/etd/2540>

This Master's Thesis is brought to you for free and open access by ThinkIR: The University of Louisville's Institutional Repository. It has been accepted for inclusion in Electronic Theses and Dissertations by an authorized administrator of ThinkIR: The University of Louisville's Institutional Repository. This title appears here courtesy of the author, who has retained all other copyrights. For more information, please contact thinkir@louisville.edu.

A NON-INVASIVE DIAGNOSTIC SYSTEM FOR EARLY
ASSESSMENT OF ACUTE RENAL TRANSPLANT REJECTION

By

Mohamed Nazih Mohamed Ibrahim Shehata
B.Sc., CECS, Mansoura University, Mansoura, Egypt, 2009

A Thesis Submitted to the Faculty of
J. B. Speed School of Engineering, University of Louisville
in Partial Fulfillment of the Requirements
for the Degree of

Master of Science in Electrical Engineering

Department of Electrical and Computer Engineering
University of Louisville
Louisville, Kentucky

August 2016

A NON-INVASIVE DIAGNOSTIC SYSTEM FOR EARLY
ASSESSMENT OF ACUTE RENAL TRANSPLANT REJECTION

By

Mohamed Nazih Mohamed Ibrahim Shehata
B.Sc., CECS, Mansoura University, Mansoura, Egypt, 2009

A Thesis Approved on

July 15, 2016

by the Following Thesis Committee:

Ayman El-Baz, Ph.D., Thesis Director

Tamer Inanc, Ph.D.

Hermann Frieboes, Ph.D.

DEDICATION

This thesis is dedicated to my beloved parents who brought me up in obeying the orders of Allah. They said and they are still saying, “ Oh Mohamed, do not despair of Allah’s mercy. Go, work hard and pay more effort and Allah will not let you down.” I wish they were here sharing with me these important moments of happiness and success in my life.

ACKNOWLEDGMENTS

In the name of Allah the Most Merciful, the Most Compassionate. All the praises and deepest thanks are due to Almighty Allah for the uncountable gifts given to me.

I would like to express my deepest gratitude to my thesis advisor, Dr. Ayman El-Baz, for his continuous encouragement, guidance, advice, and support during my M.Sc. studies.

I want to give my appreciation to Dr. Tamer Inanc and Dr. Hermann Frieboes for being on my thesis committee with enthusiasm and for taking interest in my research in the midst of many other responsibilities and commitments.

I would like to thank Dr. Georgy Gimel'farb and Dr. Robert Keynton for their useful discussions and valuable comments and feedback. I also would like to thank Dr. Mohamed Abou El-Ghar of the Radiology Department, Urology and Nephrology Center, University of Mansoura, Mansoura, Egypt, for being helpful and letting me gain from his wide experience. They all spent much of their valuable time providing advice for my work in the analysis of diffusion MR images.

I also express my deepest thanks to all members of the research group in the BioImaging Laboratory at the University of Louisville. They have been a tremendous source of support and a lot of fun to work with. Special thanks to Dr. Ahmed Elnakib, Dr. Fahmi Khalifa, Ahmed Soliman, Amir Alansary, Mahmoud Mostapha, Matthew Nitzken, Marwa Ismail, Andy Switala, Islam Abdelmaksoud, Ahmed Eltanboly, Dr. Ahmed Shalaby, and Ahmed Shaffie whose encouragement, help, and support during hard times was especially valuable.

Last but not least, I am especially grateful to all of my family members: my father Dr. Nazih Shehata, my mother Dr. Mervat Nouh, my loving wife Yasmin Moustafa, my sisters Sara Shehata and Manar Shehata, and my precious daughters Kenzi Shehata and

Carla Shehata for their great patience and encouragement with me all these years. Completing my M.Sc. degree would not have been possible without their unconditional support and love.

Finally, I would like to send a brief message to my very close friends who supported and encouraged me during my M.Sc. period, “I value your friendship and I missed you very much.”

ABSTRACT

A NON-INVASIVE DIAGNOSTIC SYSTEM FOR EARLY ASSESSMENT OF ACUTE RENAL TRANSPLANT REJECTION

Mohamed Nazih Mohamed Ibrahim Shehata

July 15, 2016

Early diagnosis of acute renal transplant rejection (ARTR) is of immense importance for appropriate therapeutic treatment administration. Although the current diagnostic technique is based on renal biopsy, it is not preferred due to its invasiveness, recovery time (1-2 weeks), and potential for complications, e.g., bleeding and/or infection.

In this thesis, a computer-aided diagnostic (CAD) system for early detection of ARTR from 4D (3D + b -value) diffusion-weighted (DW) MRI data is developed. The CAD process starts from a 3D B-spline-based data alignment (to handle local deviations due to breathing and heart beat) and kidney tissue segmentation with an evolving geometric (level-set-based) deformable model. The latter is guided by a voxel-wise stochastic speed function, which follows from a joint kidney-background Markov-Gibbs random field model accounting for an adaptive kidney shape prior and for on-going visual kidney-background appearances. A cumulative empirical distribution of apparent diffusion coefficient (ADC) at different b -values of the segmented DW-MRI is considered a discriminatory transplant status feature. Finally, a classifier based on deep learning of a non-negative constrained stacked auto-encoder is employed to distinguish between rejected and non-rejected renal transplants. In the “leave-one-subject-out” experiments on 53 subjects, 98% of the subjects were correctly classified (namely, 36 out of 37 rejected transplants and 16 out of 16 non-rejected ones). Additionally, a four-fold cross-validation experiment was performed, and

an average accuracy of 96% was obtained. These experimental results hold promise of the proposed CAD system as a reliable non-invasive diagnostic tool.

TABLE OF CONTENTS

DEDICATION	iii
ACKNOWLEDGMENTS	iv
ABSTRACT	vi
LIST OF TABLES	x
LIST OF FIGURES	xi
LIST OF ALGORITHMS	xiii
CHAPTER	
I. EXISTING TECHNIQUES FOR THE ASSESSMENT OF RENAL RE- JECTION: A SURVEY	1
A. Introduction	2
B. Kidney Anatomy and Function	3
C. Renal Problems/Symptoms and Treatment	5
D. Post-Transplant Follow-Ups and Complications	9
1. Types of Complications	9
2. Graft Dysfunction	10
E. Detection/Assessment of Renal Rejection	11
1. Traditional Methods	12
a. Urine Tests	12
b. Blood Test/Works	12
c. Biopsy (Gold Standard)	13
2. Image-Based Techniques for Renal Transplant Evaluation	15
3. Ultrasound (US) Imaging	15
4. Magnetic Resonance Imaging (MRI)	18
a. Dynamic Contrast Enhanced (DCE) MRI:	19
b. Blood Oxygen Level Dependant (BOLD) MRI:	23
c. Diffusion-Weighted (DW) MRI:	25
F. Chapter Summary	28
G. Thesis Organization	28
1. Chapter I	28
2. Chapter II	29
3. Chapter III	29
II. COMPUTER-AIDED DIAGNOSTIC SYSTEM FOR EARLY DETECTION OF ACUTE RENAL TRANSPLANT REJECTION USING DIFFUSION- WEIGHTED MRI	30
A. Introduction	30
1. Prior Work on DW-MRI Segmentation	31
2. Prior Work on Renal Function Assessment	34
B. Methods	36
1. 3D Kidney Segmentation	36
a. Appearance-Based Shape Prior:	39

b.	Second-Order MGRF Model of Region Maps:	40
c.	First-Order Kidney/Background Appearance Model:	41
d.	Appearance- and Shape-Guided Deformable Model:	42
2.	Estimating and Depicting Diffusion Parameters	43
3.	Autoencoding and Deep Learning-Based Classifier	44
C.	Experimental Results	49
1.	DW-MRI Data Collection	49
2.	Segmentation Results	49
3.	Diagnostics Results	55
D.	Chapter Summary	59
III.	CONCLUSIONS AND FUTURE WORK	61
A.	Summary of Contributions	61
B.	Future Avenues	62
	REFERENCES	65
	APPENDIX	93
	APPENDIX	93
A.	Evaluating Segmentation Accuracy	93
B.	List of Abbreviations	96
	CURRICULUM VITAE	100

LIST OF TABLES

TABLE.	PAGE
1. Segmentation accuracy of the proposed segmentation method using DSC, MHD(mm), and AKVD(%). All metrics are represented as minimum (Min), maximum (Max), and mean± standard deviation (SD).	51
2. Segmentation accuracy of the proposed segmentation technique against three other level-sets methods using DSC, MHD(mm), and AKVD(%). All metrics are represented as mean± standard deviation (SD).	51
3. Diagnostic accuracy based on the input CDF of the ADC for individual b -values and the fused CDFs of all b -values.	55
4. Diagnostic accuracy, sensitivity, and specificity for the developed CAD system with the SNCAE classifier using different CDF encoding steps (Δ_i). . . .	56
5. Diagnostic accuracy, sensitivity, and specificity for the developed CAD system with the SNCAE classifier using different structures, i.e., different number of hidden layers (l) and hidden nodes at each layer (s_l), using the same input size of 1100 (11 CDFs each of 100 region), $\alpha = 3 * 10^{-5}$, $\beta = 3$, and $\gamma = 0.1$	56
6. Sensitivity to a training set based on a four-fold cross-validation scenario. . .	57
7. Diagnostic accuracy in terms of correctly classified vs. true non-rejection (NR) and rejection (R) cases, sensitivity, specificity, and AUC for the proposed CAD system with the SNCAE classifier and seven classifiers from the Weka collection [1].	58
8. List of abbreviations that have been used in this thesis.	96

LIST OF FIGURES

FIGURE.	PAGE
1. Coronal cross-section of a normal kidney with labeled anatomy.	4
2. A nephron structure with labeled anatomy and pathway of filtration.	5
3. Anatomy of renal system of a patient after kidney transplant.	8
4. Illustration of ultrasound-guided renal biopsy procedure.	14
5. An example of different ultrasounds.	16
6. Illustrative example of a DCE-MRI sequence with pre-, post-, and late-contrast.	19
7. A simple demonstration of grey and R2* colored images for a normal kidney and a kidney with graft dysfunction.	23
8. A demonstration of a DW-MRI sequence at different b -values.	25
9. Proposed CAD system for detecting renal rejection from 4D DW-MRI.	35
10. Coronal cross-sections of raw DW-MRI samples showing (a) similar intensities of kidney and surrounding tissues (e.g., at b_0), (b) inter-patient anatomical differences (e.g., at b_0) compared to the cross-section (a), and (c) image noise, especially, at higher gradient strengths and duration (b -values) (e.g., at b_{1000}).	36
11. 3D zero-level set of a function $\Phi(\mathbf{p} = [x, y, z], t)$	38
12. Raw coronal DW-MRI cross-section before (a) and after (b) its preprocessing.	39
13. 3D co-alignment of training DW-MRI to a single reference: grayscale images before (a) and after (b) their alignment and overlapped 3D binary volumes before (c) and after (d) alignment, the reference image and targets being in yellow and red, respectively.	40
14. Empirical ADC distributions and their CDFs for one subject at different b -values.	44
15. Block-diagram of an NCAE (a) and an SNCAE (b) classifier.	46
16. The proposed model segmentation (red) with respect to the expert's manual ground truth (green): coronal (left column), axial (middle column), and sagittal (right column) cross sections for three different subjects, S_1 , S_2 , and S_3	50
17. The proposed 3D segmentation (red) with respect to the expert's manual ground truth (green) for three subjects with the associated DSC, MHD, and AKVD accuracy scores.	52
18. Four more coronal cross-sections (columns) for the proposed kidney segmentation from DW-MRI acquired at different b -values s/mm^2	52

19.	Comparative cross-sectional segmentation results for our approach, the traditional CV [2] level-set, the level-set guided by intensity alone, and intensity and spatial, respectively, in rows for three different types of cross sections (coronal cross section in the first column, axial cross section in the second column, and sagittal cross section in the third column) for one subject at b_0 s/mm^2 . The model segmentation is shown in red with respect to the manual ground truth (green) from an expert.	53
20.	A sample coronal cross-sectional kidney segmentation for DW-MRI data acquired at b_{300} s/mm^2 (first row), b_{500} s/mm^2 (second row), b_{700} s/mm^2 (third row), and b_{1000} s/mm^2 (fourth row) for (a) the proposed approach; (b) the CV [2] approach; (c) the level-set guided by intensity only; and (d) intensity and spatial.	54
21.	ROC curves and their AUC for SNCAE and Weka classifiers [1].	58
22.	Pixel-wise parametric maps for DW-MRI at different b -values (b_{50} to b_{1000}) s/mm^2 and their average value for two non-rejection (S_1, S_2) and two rejection (S_3, S_4) subjects.	59
23.	2D illustration of segmentation errors calculation between the segmented and ground truth objects for the DSC determination.	93
24.	2D schematic illustration for the HD calculation.	94
25.	3D schematic illustration for the AKVD estimation.	95

LIST OF ALGORITHMS

ALGORITHM.	PAGE
1. Creating / Updating the Shape Prior.	41
2. DW-MRI Segmentation by Geometric Deformable Boundary	43
3. Kidney Transplant Status Classification and ADC Color Mapping	48

CHAPTER I
EXISTING TECHNIQUES FOR THE ASSESSMENT OF RENAL REJECTION: A
SURVEY

The kidney is a very important complicated filtering organ of the body. Many complications and diseases can arise in this organ. One such disease is chronic kidney disease (CKD), which is a gradual loss of function of the nephrons. When the kidney reaches stage 5 chronic kidney disease, end stage renal failure, the preeminent therapy is renal transplantation. Although it is the best form of treatment, the dearth of kidney donors is still challenging. Therefore, all efforts should be employed to prolong the survival rate of the transplanted kidney. However, graft dysfunction (e.g., acute rejection) is one of the serious barriers to long term kidney transplant survival. Currently, graft dysfunction's gold standard of diagnosis is renal biopsy. Although renal biopsy is helpful, it is not preferred due to its invasive nature, high morbidity rates, and expensiveness. Therefore, noninvasive imaging techniques have become the subject of extensive research and interest, giving strong promise to replace, or at least to decrease, biopsy usage in diagnosing graft dysfunction. This chapter will discuss not only the kidney anatomy, chronic kidney disease, treatment, and current diagnosis but also the state-of-the-art imaging techniques in diagnosing graft dysfunction.

A. Introduction

The kidney is a very important organ. It is the main filtration organ in the human body, keeping the nutrients that the body needs in and expelling the waste that can become toxic. Maintaining the health of this organ is critical. There are diseases that can cause the kidney to decrease in function such as diabetes, hypertension, glomerular disease, and polycystic kidney disease [3]. These can cause a gradual loss of function in the kidney leading to waste build up in the body and the patient to develop chronic kidney disease (CKD). CKD affects about 26 million people with 17,000 transplants being performed each year in the U.S. [4, 5]. Though this has greatly improved the outcome of patients diagnosed with stage 5 CKD, complications can still arise. One of the main concerns is graft dysfunction. Routine post-transplantation clinical evaluation of kidney function is of immense importance to prevent the graft loss. The diagnostic technique currently recommended by the National Kidney Foundation (NKF) to measure overall kidney function is Glomerular Filtration Rate (GFR), which is based on measuring the serum creatinine level. However, this test has low sensitivity and is a late marker for renal dysfunction (a significant change in serum creatinine level is detectable only after the loss of 60% of renal function), and it does not assess the function of individual kidneys. The current gold standard for diagnosing different types of kidney dysfunction is needle biopsy [6]. However, this can be difficult, costly, and time-consuming. Renal biopsy can also result in complications such as infections, bleeding, and at times, death. With the evolution of computer-aided diagnostic (CAD) systems, we hope to non-invasively diagnose different types of graft dysfunction, saving time and money. This chapter will give an overview on how CKD is treated and kept viable in post-transplantation when it is affected by graft dysfunction. Thus, the need for new noninvasive techniques which have the capability to provide accurate diagnosis of kidney dysfunction is of great clinical importance.

This chapter presents an overview of current clinical techniques for renal transplant function evaluation as well as an examination of new ways to improve the detection of graft dysfunction using image-based technology [7]. The rest of this chapter is organized

as follows: Section I.B provides a brief overview of the anatomy and function of the kidney. Section I.C takes a closer look at who is more at risk for developing CKD and some symptoms associated with it. In addition, an overview of the treatment options for people that develop stage 5 CKD will be given, concentrating on transplantation as a definitive therapy. Section I.D takes a look at follow-up post transplantation care, which includes possible complications that could arise with a concentration on graft dysfunction. Section I.E will concentrate on tests that are performed to detect graft dysfunctions including the traditional methods such as blood, urine, and renal biopsy. This is followed by the image based techniques such as ultrasound, and magnetic resonance imaging (MRI).

B. Kidney Anatomy and Function

As stated before, kidneys are the main filtration system in the body. Kidneys are able to keep nutrients like salts, sugar, and protein in, while at the same time expelling excess nutrients, water, and waste such as urea and ammonia out of the body. Kidneys keep human bodies in a homeostatic state. They regulate the blood's pH, blood pressure, and osmolality. Osmolality is the amount of particles of solutes that are dissociated in a solvent [8]. Each kidney is shaped like a bean and is about the size of a fist [9] and weighs about 150 g [10]. They are located in the lower back below the rib cage.

As shown in Figure 1, the kidney is composed of an outer "shell", which is the renal cortex; an inner layer, the renal medulla; and a hollow area where the urine is collected, the renal pelvis [10]. Inside the cortex and medulla are the filtration units known as the nephrons (see Figure 2), which are then made up of smaller subunits such as the glomerulus, vasa recta, and loop of Henle [10]. Since the kidneys must filtrate the blood, they must be connected to veins and arteries. The kidneys are connected to the renal artery and vein which are connected to the iliac artery and vein, respectively. That is the general overview of the anatomy of the kidneys, now this chapter will trace the filtration pathway of the blood. The blood enters the kidney by way of the renal artery. Once there, the blood moves to the nephrons of the cortex where the blood then enters the afferent arteriole which allows

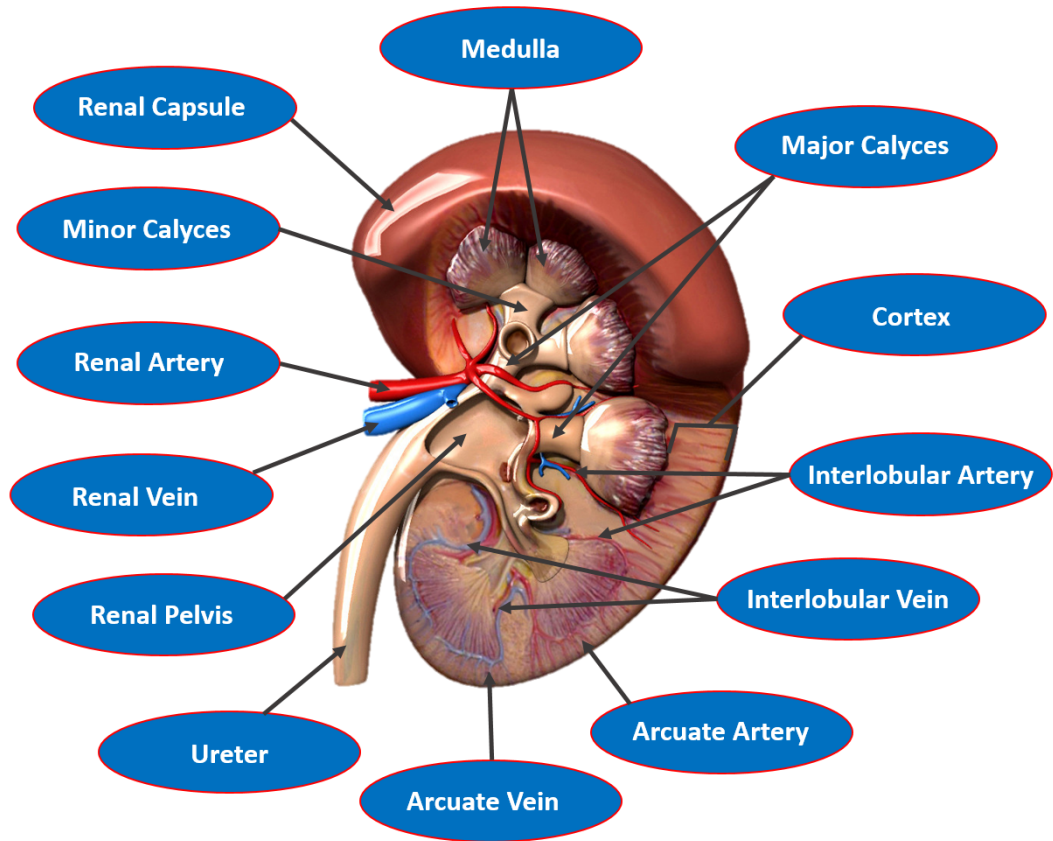


FIGURE 1: Coronal cross-section of a normal kidney with labeled anatomy.

the blood to enter in the glomerulus. The glomerulus is then able to filter out waste through the assistance of blood pressure. This waste is filtered into the Bowman's capsule. From the Bowman's capsule the waste moves to the proximal tubule then to the Loop of Henle and thin segment, which can be found in the medulla. At these places in the nephron, more filtration can be done. From here, waste moves to the distal tubule then the collecting tubule and finally into the renal pelvis. The waste that ends up in the renal pelvises will then move through the ureter to the bladder and then out of the body by way of the urethra. The clean blood exits the glomerulus by way of the efferent arteriole. Once there, more filtration can be done in the Peritubular capillaries where the blood could also move down the Vasa recta in the medulla; nutrients that were filtered out by the loop of Henle and thin segment can be resorbed there. The blood then exits through the venules and then through the arcuate veins, and finally leaves the kidney through the renal vein. The clean blood can then travel

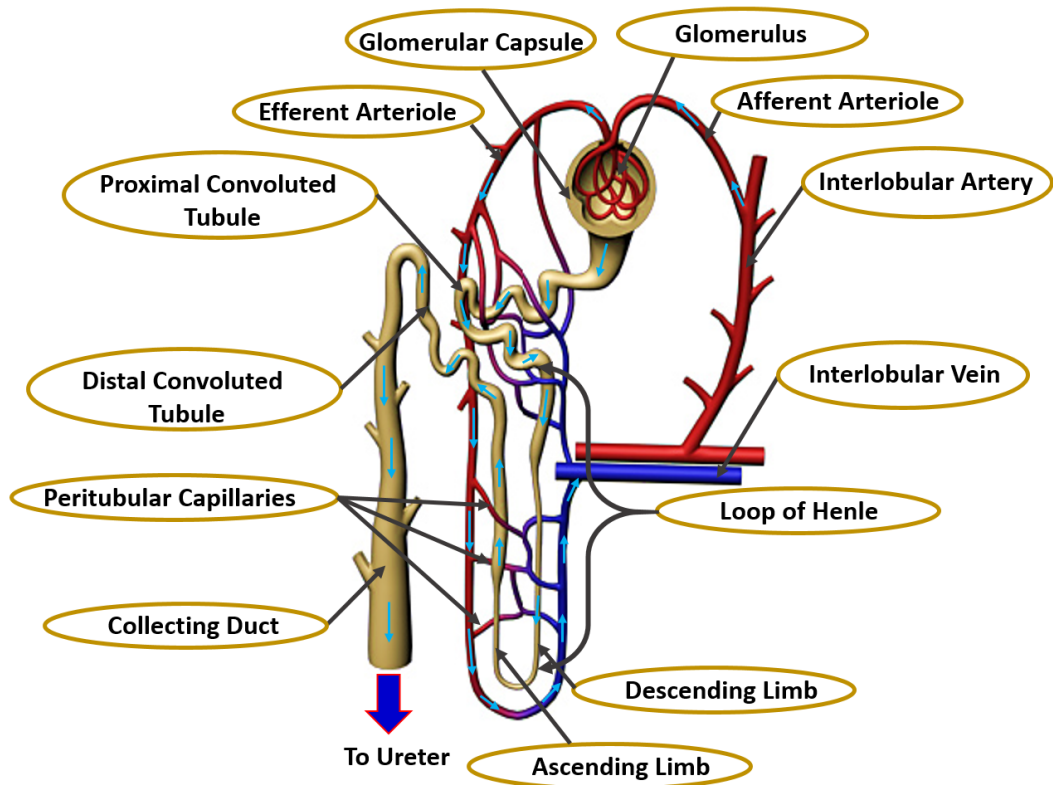


FIGURE 2: A nephron structure with labeled anatomy and pathway of filtration.

back to the heart [10]. As one can see, this organ is very complex and with this complexity many problems can arise. In the next section this chapter will discuss what can go wrong and who is at risk of developing these complications.

C. Renal Problems/Symptoms and Treatment

The renal system is a very complex system, in which various complications and diseases can arise pertaining to it, especially with the kidney. There are multiple conditions and/or diseases that can arise in the kidney such as kidney stones, injury, infections, and cancer. The focus of this chapter will be on CKD, the 9th leading cause of death in America [11]. CKD is a gradual loss of function of the kidney, where the nephrons become compromised [4]. To date, 26 million people in the U.S. are living with CKD [4]. The risk of developing CKD could be increased due to a few different factors such as various physiological conditions, diseases, age, race, lifestyle, and family history. Conditions that

increase the likelihood of developing CKD include diabetes, high blood pressure, heart disease, and high cholesterol [12]. People with the following diseases are at increased risk of CKD; HIV, Hep C, Metabolic syndrome, cancer, and sickle cell trait [13]. Individual 65 years or older are also more at risk. African Americans tend to also have a greater risk compared to the rest of the population [12]. Lifestyles that increase risk include obesity [14] or smoking [12]. The last risk factor is family history; if a patient has a parent or family member with CKD they have a greater chance of developing the disease [12]. People with these risk factors should be aware and contact their doctor if any of the following symptoms become present. In early stage CKD the patient may be asymptomatic but as the disease progresses, kidney function will worsen and symptoms will develop. Symptoms can include change in urination, whether it changes in frequency, feeling, color, or texture. The urine can also start to contain blood [15]. Apart from the change in urination, symptoms can include limb swelling, iron build up that can cause nose bleeds and bad breath [15]. As the disease progresses infection-like symptoms can arise [16]. CKD can have an effect not only on the body but also on mental state and activity level. These symptoms can include fatigue, generalized weakness, decreased libido, change in memory [16], and a decline in mental function [15]. More rare but more serious symptoms may include rash, generalized pain, chest pain, and shortness of breath [15–18]. If a patient should have any of these last symptoms, he/she should seek immediate medical attention. Every patient is different and there is no set relationship between symptoms and the stage of the patient's kidney disease [16]. As stated before, if one should develop any of these symptoms, he/she should talk to their doctor about checking for CKD. If left untreated, symptoms could worsen and kidney failure will advance to stage 5 CKD. The untreated patient with stage 5 CKD could die due to the build up toxins in the body. To prevent this from happening, the patient should be treated with dialysis or transplantation.

Luckily, there have been developments in treatments for patients with stage 5 renal failure. Those treatments include blood dialysis or renal transplant. Blood dialysis is when one's blood is filtered of waste or excess water, either with use of a machine outside the body (hemodialysis) or chemically inside the body (Peritoneal Dialysis) [19]. Though

dialysis is a helpful treatment, a more long term treatment would be kidney transplantation. This is where a donor's kidney is surgically inserted into the CKD patient. That new kidney should improve filtration for the patient. Since transplantation is the definitive therapy for End-Stage Renal Disease (ESRD), the following describes in more detail the kidney transplantation procedure and associated complications and diseases.

As previously stated, renal transplantation is a surgical procedure where a donated kidney is placed inside the patient with CKD. However, it does not mean that a nephrectomy (i.e. removal of the malfunctioned kidney) is performed on the patient with CKD. The patient with CKD usually gets to keep both of the kidneys, unless those kidneys are causing pain or other complications [20]. This means that the patient will have three kidneys after the procedure. The donated kidney also has its own ureter, renal artery, and vein intact. The donated kidney is placed below (distal of) the native kidneys with the donated ureter connecting to the bladder, and the renal artery and vein connecting to the iliac artery and vein of the patient, respectively [21]. Figure 3 demonstrates the entire anatomy of a patient renal system after transplantation.

This procedure seems fairly simple in concept. However, the process to find that donor can be fairly complicated not only medically and logistically but also due to legal hurdles. There are two different types of donors that can be used for CKD; cadaver and living donors. Only one third of the transplantations are from living donors while two thirds of the transplantations are from cadaver donors [22]. Often, the physician and the CKD patient must decide whether to use a living or a cadaver kidney. Often a more desirable choice would be to have a living donor give one of their kidneys. However, this is not without its complications. The donor must meet all criteria such as being HLA (+or-) and/or ABO compatible, physically in good health, and be in no way coerced against their will to donate [22, 23]. This means that the donors can back out at any time. This is why even if there is a willing living donor the physician may persuade the patient to get on the United Network of Organ Sharing (UNOS) [24]. Depending on where the patient is on the list determines if and when they will receive a donor. The donated kidneys from this list are from cadaver donors. In order for the cadaver's kidney to be viable the kidney must

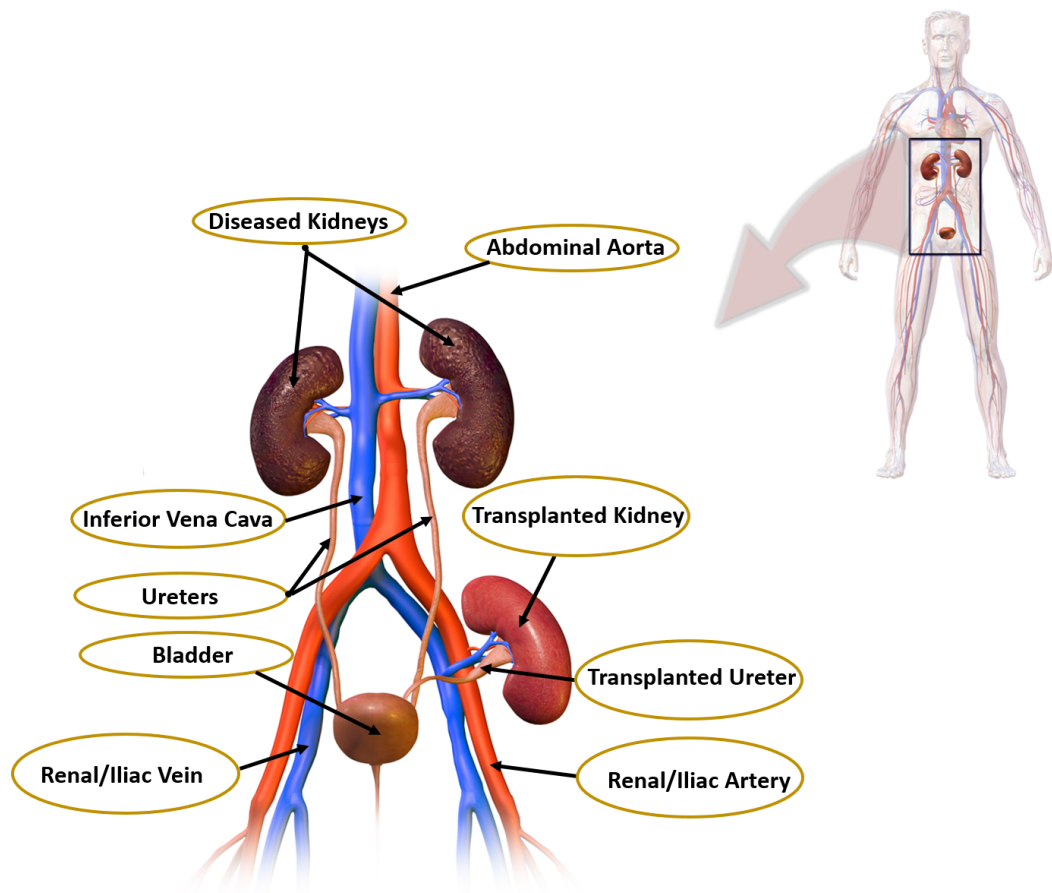


FIGURE 3: Anatomy of renal system of a patient after kidney transplant.

be functioning before death and the manner of death must not damage the organ. Also the time and location of death may play a part since the kidney must not decompose before the kidney can be donated [22]. In the United States, the living donors must be willing to give up their kidney, cadaver donors must also make it clear that they are willing to be a donor after death. With all of these criteria, it is no wonder that although there are about 17,000 kidney transplants performed annually in the United States, there are still about 100,800 people waiting for a kidney. With this in mind, it is very important that the transplanted kidney is kept viable as long as possible so that a nephrectomy and repeat transplantation do not have to be performed [5]. In the following section, an overview on what happens during post-transplantation care should be given, which in turn should improve the viability of the organ post-transplantation. This includes follow up procedures and the complications that arise for transplant patients.

D. Post-Transplant Follow-Ups and Complications

Just as with any medical procedure complications can arise such as infection and bleeding. so one must remain in constant care of one's physician. They must continue follow ups to insure that the new kidney is functioning and that new complications do not arise. To prevent new complications from arising, the patient should follow the instructions of their physician by taking their anti-rejection medications and visiting their physician as directed [25]. The frequency at which a patient has to visit their physician will decrease as time after transplantation increases. Once the patient has reached 210 days post-operatively, they should be seeing their physician monthly or if abnormalities arise [26]. During those clinical visits various tests such as examining the patient's weight, blood pressure, and temperature will be done to assess both the overall health of the patient and the health of the kidney. The urine and the blood tests will be discussed later in this chapter. If these tests appear abnormal, the physician may order a renal biopsy and/or scans [27]; both will be discussed in greater detail later on in the chapter. For now, this chapter will concentrate on the complications that can arise during these tests, specifically those complications that are associated with (renal) transplants. This Section will take a look at those types and concentrate specifically on graft dysfunction. First, this chapter will explain types of complications other than graft dysfunction.

1. Types of Complications

There are six categories of complications including: urological complications, vascular complications, fluid collection, neoplasms, recurrent native renal disease, and graft dysfunction. This section will take a short look at the first five complications then the next section will go a little more in depth for graft dysfunctions. The term urological complications generally refers to uncontrolled or obstructed urine flow [28, 29]. Vascular complications are complications that are associated with the vascular system of the renal system, i.e. renal or iliac artery/vein. Vascular complications can include narrowing, blockage or formations of holes in the vascular system [30]. Fluid collection is closely related

to urological complications and/or vascular complications in that if there is a urological or vascular complication, fluid such as blood or urine will collect in areas where they are not supposed to be collecting. This will create urinomas, hematomas, abscesses, or lymphocelles [29–31]. Neoplasms are abnormal growth such as tumors that grow on the renal system and other areas. This is said to be caused by the prolonged exposure to immune repressor drugs [30, 32, 33]. Lastly, recurrent native renal disease is when the disease that caused the patient to develop CKD in the first place, such as diabetes, is now affecting the donated kidney [34, 35]. It is possible for the patient to develop a combination of these complications. It is important that for any of these complications, diagnosis and treatment are done as soon as possible. Most of these complications are usually easier to detect as compared to graft dysfunction. This is because these complications can be detected using various imaging techniques such as ultrasounds and MRIs [36]. These imaging techniques will be discussed later on in this chapter but the concentration will be more on graft dysfunction. The complication and cause that is more challenging to diagnose is graft dysfunction, which shall be examined next.

2. Graft Dysfunction

Graft dysfunction simply means that the newly transplanted organ is no longer functioning, toxins then build up, and the body rejects the transplanted organ [30]. It was calculated that within the first five years post transplantation, 15% of patients will experience graft dysfunction [37]. There are three classes of graft dysfunction: hyperacute, acute, and chronic. The type of graft dysfunction is differentiated by the mechanism and somewhat by the time of dysfunction onset [38]. Hyperacute rejection is relatively rare nowadays. This class of rejection is caused by antibodies attacking the donated organ due to the donor organ having the wrong HLA (+or-) and/or ABO blood antigen and will present itself within in minutes or hours after transplantation [23]. There is no cure for hyperacute rejection [39]. Chronic kidney rejection's mechanism is not well understood but appears to present itself after five years post-transplant [23]. The main concentration in this chapter

will be on Acute Kidney Rejection (AKR). Just as there are different types of complications in renal transplant, there are different causes of graft dysfunction. This can provide somewhat of a challenge in diagnosis and treatment. This is due to the fact that there is a different treatment for each cause of graft dysfunction. There are four different causes of graft dysfunction; they include: acute tubular necrosis (ATN) antibody-mediated rejection, T-cell mediated rejection, immunosuppressive toxicity (ITox), and viral infection (VI). ATN is when the antibodies of the patient recognize the newly donated kidney as a foreign body causing the tissue to become necrotic and die. It is treated with a drug therapy regimen that may include plasmapheresis, mycophenolate mofetil, and tacrolimus [40–42]. T-cell is when killer T-cells attack the donated organ causing apoptosis in the tissue [38]. The treatment for T-cell mediated rejection includes drugs such as corticosteroids, antithymocyte globulin, and immunosuppression therapy. If the patient has antibody-mediated rejection, they may not respond to the T-cell mediated rejection treatment [43–45]. Immunosuppressive toxicity is when the immunosuppressive drugs that are supposed to be preventing the immune system from rejecting the donated kidney actually cause renal failure since these drugs can be nephrotoxic. Treatment for this would be to cease or change the medication, cease, or to reduce the dose of the nephrotoxic drug such as Cyclosporine and tacrolimus [46–48]. VI is when viruses such as Cytomegalovirus or Herpes simplex virus enters the body and damages the kidney [49]. Treatments for VI may include administering immunosuppressant and/or antiviral medications [40]. The causes of AKR can be presented singularly or in combination, which can add to the difficulty in diagnosing the cause of AKR. How the cause of these graft dysfunctions are diagnosed will be discussed in the next section of this chapter.

E. Detection/Assessment of Renal Rejection

It is important that the patient keeps regular visits with their physician in order to ensure that their newly transplanted organ is in working order. The post-transplantation follow-ups' main concern is to keep the graft viable for as long as possible. If the patient

continues regular follow-ups and notifies the physician of any symptoms that arise, it is possible that they can catch the problem early and save the donated organ. This chapter will give an overview of the existing techniques/methods for diagnosing graft dysfunction. This includes both traditional, non-imaging, clinical methods, and the imaged-based techniques that are in use but are still being developed and/or improved for use. More details about both methods are given below.

1. Traditional Methods

Traditionally, during a routine follow-up a blood and urine analysis will be implemented. If there are any abnormal results in either of these, the physician may order a renal biopsy to get a definitive diagnosis. This diagnosis should also tell the physician what is causing the kidney malfunction. This next section will show how these diagnoses are determined. First, this chapter will discuss urine testing.

a. Urine Tests This method is very simple in use. It can test for multiple substances and is non-invasive. Using the patients urine, the physician is able to measure a number of biomarkers to determine GFR. Most often the biomarker used to calculate GFR is serum creatinine. To calculate GFR, the concentration of creatinine found in the urine sample is placed into an equation which has constants that change based on sex, race, and age. Using the calculated GFR, one is able to determine what stage of function the kidney(s) are in, 0 being at an increased risk and 5 being end stage renal failure [50, 51]. This diagnostic technique is currently recommended by the NKF to measure overall kidney function. However, this test has low sensitivity and is a late marker of renal dysfunction (a significant change in serum creatinine level is detectable only after the loss of 60% of renal function), and it does not assess the function of individual kidneys [6]. The next test that shall be discussed will be a blood test.

b. Blood Test/Works This method is similar to urine in that it measures estimated GFR using serum creatinine. However, since it does pierce the skin when obtaining the blood, this test is slightly more invasive. A complete blood count and differential count

(CBC and diff) [52] measure more substances than urine including detecting the presence of burred blood cells which can be present in patients with CKD. Burr cells are blood cells that appear almost gear like. They appear when there is an excess amount of waste in the body, which is likely to happen in patients with CKD [53, 54]. Though it has slightly more benefits than a urine test, it has the similar setback in that the test has low sensitivity and is a late marker of renal dysfunction and it does not assess the function of individual kidneys [6]. The last traditional method that shall be discussed is a renal biopsy.

c. Biopsy (Gold Standard) Renal biopsy is a traditional method for the graft function assessment that is by far the most invasive, but to date is considered the gold standard. This procedure is performed using a renal biopsy needle that is inserted into the patient's back and kidney while being guided by a camera, ultrasound, or x-ray, as shown in Figure 4 [52]. The tissue that is obtained is read using a microscope [55]. The patient is fully conscious and asked to hold their breath and to not move [52]; if one should breathe or move, they run the risk of piercing other organs. Along with the risk of piercing other organs the patient also runs the risk of excessive bleeding and infections. Excessive bleeding can present itself more so in a patient who is on blood thinners. Infections are likely to occur since the patient is more than likely on an immunosuppressive therapy regimen [37, 56]. These complications can lead to nephrectomy or even death; both occur in 1 in every 1,000 renal biopsies [37].

Along with the invasiveness of the procedure, there are multiple setbacks that are associated with this procedure. Renal biopsies, although a useful tool, have the tendency to give a missed diagnosis or inaccurate estimate of the extent of the problem. This is because it is only sampling a small portion of the kidney and if off target in the slightest can miss an effective portion of the kidney and give a false negative. This would mean that a repeat biopsy may have to be performed causing the patient more pain and precious time lost in order to save the graft. On the subject of time, the time it takes to obtain the results can take up to two weeks [57]. That time which could be used for treatment is wasted and can result in failure of the donated kidney. On top of these setbacks, the financial cost of the procedure can reach over (\$20,000) [58]. So this test cannot only cause physical pain

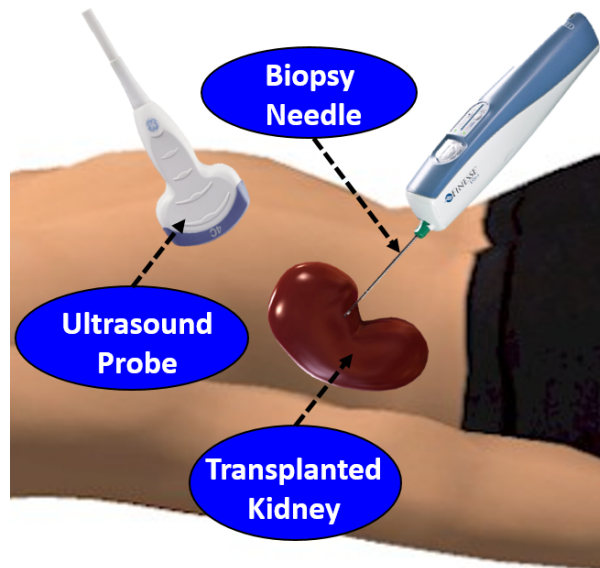


FIGURE 4: Illustration of ultrasound-guided renal biopsy procedure.

but also create more of a financial burden. Though these tests have been routinely used for transplant assessment and have helped in improving graft survival, one can see that there needs to be a better way to diagnose and differentiate the cause of graft dysfunction. Additionally, existing techniques, i.e. GFR and biopsy, for diagnosis of renal rejection are late biomarkers. Moreover, renal biopsy has significant morbidity, is very expensive, takes up to two weeks to get the final report, and can result in over- or under-estimation problems by only sampling small areas of the kidney. Therefore, the development of non-invasive tests to monitor kidney transplant rejection status is of immense importance. This, in turn, will allow doctors to intervene early to prevent rejection and the damage it causes, which will improve long-term outcomes. The following section will overview existing non-invasive imaging techniques and their possible use for assessing renal function and diagnosing graft dysfunction. In this chapter, the imaging techniques that will be discussed are ultrasound and MRI.

2. Image-Based Techniques for Renal Transplant Evaluation

The development of computer-aided diagnosis (CAD) systems for renal transplant assessment using different imaging modalities is an ongoing area of increased research. Non-invasive imaging-based techniques have been clinically used to assess transplanted kidneys with the advantage of providing information on each kidney separately. For example, radionuclide imaging (also called scintigraphy), the traditional method in renal imaging, is an excellent modality for evaluating graft function, both qualitatively and quantitatively, while also screening for common complications [59]. However, this technique fails to show accurate anatomical details due to its limited spatial resolution, so functional abnormalities inside different parts of the kidney (such as cortex and medulla) cannot be discriminated precisely [60]. Furthermore, radionuclide imaging includes radiation exposure [61], thus limiting the range of its applications, especially in monitoring such diseases as ATN or cyclosporin [62]. Computed tomography (CT) is a commonly available technology that uses contrast agents that allows accurate evaluation of various diseases in renal transplantation and with lower costs than magnetic resonance imaging (MRI) [63]. However, information gathered by CT to detect renal acute rejection is unspecific and the contrast agents used still are nephrotoxic. Therefore, currently CT has a limited role in diagnosing acute renal rejection [64]. In contrast to these radionuclides and CTs, ultrasound (US) and MRI are the most popular imaging modalities used for the diagnosis of kidney diseases. In the following sections, an overview of different CAD systems for the diagnosis of acute renal rejection using these two imaging modalities is given.

3. Ultrasound (US) Imaging

Ultrasound (US) imaging is usually used for the early assessment of renal allografts functionality in the postoperative period as well as for the assessment in the long-term follow-up thanks to being a relatively easy to be performed and repeated, inexpensive, and non-nephrotoxic imaging modality. [9]. Pulsatility index (PI) and resistance index (RI) are the most common measurements to assess renal functionality using US. Some recent stud-

ies that assessed renal transplants using different forms of ultrasound (e.g., power doppler (PD), color doppler (CD), contrast enhanced (CE), etc.), please see Figure 5) are discussed.

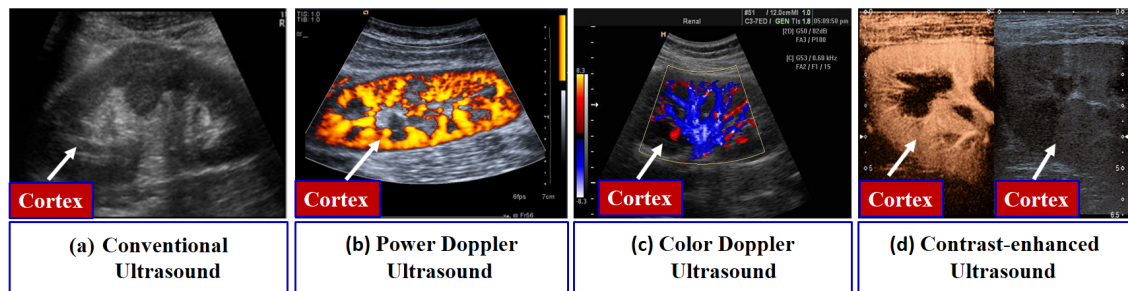


FIGURE 5: An example of different ultrasounds.

In an investigation to characterize the factors that influence PI and RI in patients with immediate (IGF), slow (SGF), or delayed (DGF) kidney graft function, Chudek et al. [65] observed that ischemic injury which occurred mainly prior to organ harvesting played a dominant role in determining intra-renal resistance in the early post-transplant period. A study by Saracino et al. [66] investigated whether the long-term renal functionality could be predicted using RI measurements taken early after kidney transplant. On the other hand, Kramann et al. [67] concentrated in their study on evaluating the potential of RI measurements to predict renal allograft survival. They concluded that, for prediction of long-term allograft survival, RI measurements should be taken 12-18 months post-transplantation. Krejčí et al. [68] utilized a composite gray-scale, CD imaging, and PD imaging to examine the power of US for early detection of a subclinical acute rejection. A significant difference between the four different groups in their study was obtained. In another study by Damasio et al. [69], the ability of doppler US to differentiate between dual and single kidney transplantation (DKT) and (SKT), respectively, was exploited. After the measurement of RI parameters for both DKT and SKT groups, they concluded that those patients with DKT had higher RI and lower kidney volumes than those with (SKT).

A study by Shebel et al. [70] investigated the ability of PD in the differentiation between acute rejection (AR) and ATN. Their study included 67 renal transplant recipients in the early post-transplantation period. After a manual placement of regions of interest

(ROIs), cortical perfusion (CP) and RI were measured for all recipients and CP was tested with respect to serum creatinine (SCr) and RI. Upon their own CP grading scale system, they found a statistical significant correlation between their CP grading and SCr ($P < 0.01$) and between CP grading and RI ($P < 0.05$). They concluded that the PD using CP grading is more sensitive in the detection of early AR compared to RI and cross-sectional measurements.

Fischer et al. [71] proved the superiority of ultrasound contrast media (USCM) to conventional US that uses the RI indicator in the diagnosis of early allograft dysfunction. In addition, Benozzi et al. [72] found that both US and CEUS could identify grafts with early dysfunction, but only some CEUS derived parameters could differentiate between ATN and AR. Schwenger et al. [73] exploited the power of CE sonography (CES) in early prediction of long-term renal transplant functionality compared to CD ultrasonography (CDUS). In their study, 68 renal transplants were investigated using both CES and CDUS one week after transplantation. Renal blood flow (RBF) and RI were measured for all transplant recipients and were correlated with the recipients' clinical data represented by glomerular filtration rate (GFR) in a post-transplantation period from one week to one year. They concluded from their observations that RBF measurement using CES was significantly correlated with kidney functionality in the aforementioned period after transplantation, in contrast with RI measurement using CDUS. Another study was explored by Göcze et al. [74] to differentiate between acute kidney injury (AKI) stages using CEUS based on the quantification of blood perfusion. Instead of generating time-intensity curves (TIC), they used another quantification method called arrival time parametric imaging (ATPI). Their study included 10 patients who underwent CEUS, of which four patients had no evidence of AKI, one with stage AKI, and five with stage 2 or 3 AKI. Color-maps based on inflow time (IT) of the contrast agent were generated using the CEUS-ATPI quantification method and were divided into six major categories based on their values. Then, these ITs were assessed for different poles of kidney cortex (i.e. lower, middle, and upper) and the total IT was the sum of all arrival times of these three poles for each kidney. They observed that patients with stage 2 or 3 AKI have more delayed ITs than those of the other groups. They concluded

that CEUS-ATPI technique may help in detecting different stages of AKI. Recently, Jin et al. [75] assessed renal allografts using CEUS. In their study, 57 renal transplant patients underwent CEUS. Then, they were divided into three groups: 23 patients with AR (group 1), 10 patients with ATN (group 2), and 24 patients with normal allografts (group 3). After a manual placement of ROIs, a new index to detect AR called rising time (RisT) was measured instead of arrival time (AT). In addition, time to peak (TTP) and delta time among ROIs (Δ RisT and Δ TTP) were measured, analyzed, and correlated with clinical data (e.g., GFR). They found that RisT, TTP, and (Δ RisT and Δ TTP) were significantly higher in group 1 as compared to those in group 2 and group 3.

Although several studies utilized US to evaluate and assess renal functionality pre- and post-transplantation by evaluating conventional ultrasound parameters such as the PI and RI, two contradictory studies [76, 77] concluded that RI is not an exact indicator of renal graft dysfunction, and it could only provide a prognostic marker of the graft. Moreover, doppler US may give high PI and RI values (>0.8), which is an indication similar to those of ATN [78, 79]. These contradictions led researchers and investigators to examine a different imaging modality to assess renal functionality (e.g., MRI). In the next section, the state-of-the-art studies utilizing different MR imaging modalities are discussed.

4. Magnetic Resonance Imaging (MRI)

Magnetic resonance imaging (MRI) has become the most powerful and central non-invasive tool for clinical diagnosis of diseases [80]. The main advantage of MRI is that it provides excellent morphological information and offers the best soft tissue contrast among all imaging modalities (e.g., US and CT), which allows advanced analysis of different aspects of renal function. However, structural MRI lacks functional information. On the other hand, other MRI modalities, such as dynamic MRI, BOLD MRI and diffusion MRI are frequently used for renal function evaluation. Next, the state-of-the-art studies utilizing these MRI modalities for renal transplant assessment are overviewed.

a. Dynamic Contrast Enhanced (DCE) MRI: Dynamic MRI of the kidney has gained considerable attention in assessing renal function due to its ability to characterize tissue-specific functional changes, and potential to measure both total and cortical volume, and other functional parameters such as RBF, GFR, and renal plasma flow (RPF). Therefore, in recent years several studies have exploited DCE-MRI to non-invasively analyze kidney function in both native and transplanted kidneys. Figure 6 shows an example of DCE-MRI before, during, and after the administration of contrast to the kidney.

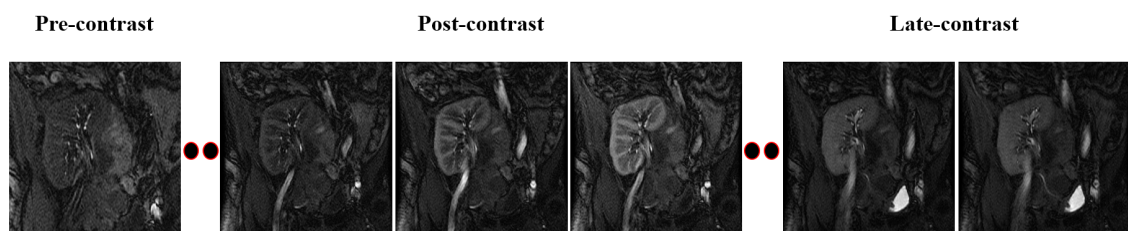


FIGURE 6: Illustrative example of a DCE-MRI sequence with pre-, post-, and late-contrast.

In particular, a study by de Priester et al. [81] utilized dynamic MR enhancement curves to qualitatively evaluate diseased (27 patients) and nondiseased (8 patients) renal transplants. Cortical and the medullary enhancement parameters were obtained from a physiological model that was fitted to the raw data. Cortical arterial blood volume and medullary wash-out rates were found as the main discriminatory parameters between diseased and nondiseased patients. Yuksel [82] introduced a DCE-MRI-based CAD system for the evaluation of transplant function, which employed deformable image segmentation, kidney registration, and cortical perfusion construction. After kidney segmentation, a manual cortical ROI is used to construct the perfusion curve from the co-aligned images and the kidney function is evaluated visually based on the pattern of the constructed curves. Automated CAD system for early diagnosis of acute transplant rejection by Farag et al. [83] and El-Baz et al. [84–86] included parametric deformable model segmentation, nonrigid alignment, and classification of the kidney status using empirical parameters. Their frameworks were tested on 30 data sets and classified kidney status of each patient using four

indexes: the peak signal intensity, the time-to-peak, the wash-in slope (slope between the peak and the first minimum), and the wash-out slope (peak and the signal measured from the last image in the sequence), calculated from the MRI signal for the kidney cortex. A supervised Bayesian classifier was employed and the system classified 13 out of 15 and 15 out of 15 correctly for both training and testing, respectively. Similar approaches were proposed in [87–89]. The study utilized a global alignment step of the MR images exploiting a special Gibbs energy function, and the perfusion curves were estimated from the whole kidney rather than only the cortex. The latter CADs were tested on a larger cohort of 100 patients and achieved a 94% diagnostic accuracy using Bayesian supervised classifier. A semiautomated approach by Rusinek et al. [90] assessed cortical and medullary functional parameters (RPF, GFR, vascular volumes of the cortex and medulla, and rate of water absorption) using compartmental modeling for both simulated and in-vivo data. Their framework employed an initial rigid alignment (translation only) step followed by a graph-cut based segmentation approach. The system was tested on 22 clinical data sets and the study concluded that the accuracy and precision in RPF and GFR are acceptable for clinical use.

Zikic et al. [91] evaluated kidney kinetic parameters after motion correction using template-matching based registration and normalized gradient field (NGF), as the contrast-invariant similarity measure. However, the kidney was segmented manually, and the evaluation of perfusion parameters (plasma volume and tubular flow) was performed visually by trained physicians for 10 data sets of healthy volunteers. Semi-automated evaluation of renal function for both native and transplanted kidneys was explored by De Senneville [92] using rigid-body registration to handle kidney motion inside a user-defined ROI. The renal cortex was segmented manually, and the GFR was estimated with Patlak-Rutland tracer kinetic model. The study demonstrated a significant uncertainty reduction on the computed GFR for native kidneys (10 healthy volunteers), but not the transplanted ones (10 transplant patients). Aslan et al. [93] developed an automated CAD system to classify normal kidney function from kidney rejection using DCE-MRI. Following kidney segmentation, three classification methods (least square support vector machines (LS-SVMs), Ma-

halanobis distance, and the Euclidean distance) were compared to assess transplant status based on medullary perfusion curves. On a cohort of 55 clinical data sets, they achieved a diagnostic accuracy, sensitivity, and specificity of 84%, 75%, and 96%, respectively using the Mahalanobis distance-based classifier. Anderlik et al. [94] proposed a framework for quantitative assessment of kidney function using a two-step motion correction and pharmacokinetic modeling. The GFR was estimated from the time-intensity curves using Sourbron et al. [95] compartment model. Their framework has been tested on 11 data sets. Zöllner et al. [96] employed a non-rigid registration using B-splines and mutual information (MI) as a similarity metric. Functional information was extracted regionally using k-means clustering [97]. This system was tested on only 4 DCE-MRI data sets and the evaluation of kidney regions was assessed qualitatively according to their mean signal intensity time courses. Wentland et al. [98] utilized MRI-based intrarenal perfusion measurement to differentiate between normal-functioning kidney allografts and allografts with ATN or AR on a cohort of 24 biopsy proven patients. The study concluded that the cortical and medullary blood flow is significantly reduced in grafts experiencing AR, as compared with normal grafts. Additionally, AR patients demonstrated medullary blood flow reduction as compared with ATN patients.

Recently, a study by Abou El-Ghar et al. [99] explored the feasibility of DCE-MRI in evaluation of renal allograft dysfunction. Their CAD system employed computer based techniques for motion correction and creation of renographic curves. Functional evaluation on 55 patients using the mean medullary intensity achieved sensitivity, specificity and accuracy of 75%, 96% and 84%, respectively, to separate normal kidneys from impaired ones. Yamamoto et al. [100] utilized dynamic MRI to prospectively assess its ability to identify the cause of acute graft dysfunction. Their study employed 60 patients, 31 of which had normal function and 29 had acute dysfunction due to AR. Their study employed a multicompartamental tracer kinetic model to estimate the GFR and mean transit time (MTT) at different compartments of the kidney. The study documented differences in the fractional MTT values between normal grafts or grafts undergoing AR or ATN; however, substantial overlaps among these groups and with normal kidneys were observed. Semi-automated

estimation of renal parameters was performed by Hodneland et al. [101]. A viscous fluid model combined with an NGF-based cost function was used for elastic kidney registration. However, the kidney was segmented interactively with the nearest neighbor approach, the framework was tested only on 4 data sets of two healthy volunteers, and the reported GFR measurements were slightly underestimated relative to the creatinine reference values. Positano et al. [102] proposed a CAD system for the estimation for renal parameters, which included a two-step rigid registration, and adaptive prediction of kidney position over the course of the respiratory cycle. The perfusion indices (peak signal intensity, MTT, initial up-slope, and time to peak) were evaluated on perfusion curves extracted from the automatically and manually registered data sets and were similar as well. An automated framework for the classification of kidney transplant status was proposed by Khalifa et al. [103, 104]. In their framework, the kidney was segmented using a stochastic geometrical deformable model approach and the local motion of the kidney was corrected for by a Laplace partial differential equation-based nonrigid alignment method [105, 106]. Their initial study [103] included only 26 data sets, and a K-nearest neighbor classifier was used. Their system achieved a 92.31% correct classification using the time-to-peak and wash-out slope empirical parameters that are estimated from the agent kidney kinetic curves. Their framework was extended in [104] by using four augmented empirical parameters (peak intensity value, time-to-peak, up-slope and average plateau) by the genetic algorithm [107]. Unlike [103], the parameters were derived from the cortex rather than from the whole kidney and the system was tested on 50 patients, and the overall diagnostic accuracy increased to 96%. Another study by Khalifa et al. [108] extended the work in [103, 104] by using analytical function-based model to fit agent cortical kinetic curves. For the classification of kidney status, five features (three were derived from the gamma-variate functional model and two are from the perfusion data, namely the time-to-peak and average plateau) were chosen and the study included 50 transplant patients.

Although DCE-MRI has been employed as a widespread imaging technique to develop several CAD systems for renal transplants assessment purpose, the contrast agents may implicate nephrogenic systemic fibrosis; thus, many medical centers are reluctant in

applying the DCE-MRI to patients with renal disease [109]. In order to circumvent this major drawback, DW-MRI and BOLD-MRI have been recently exploited to assess renal transplants as they do not involve any use of contrast agents, like DCE-MRI. A brief discussion of recent renal transplant assessment studies using BOLD-MRI follows as well as a discussion on other studies that utilized DW-MRI to assess renal transplants.

b. Blood Oxygen Level Dependant (BOLD) MRI: In addition to DCE-MRI, another imaging technique, called BOLD-MRI, has been utilized to study renal rejection using the amount of oxygen diffused blood (i.e. oxygen bioavailability) in the kidney to determine whether it is functioning properly. Specifically, the amount of deoxyhemoglobin is measured by the apparent relaxation rate ($R2^*$) parameter [110]. Figure 7 shows grey images and $R2^*$ color-maps for a normal kidney and a kidney with graft dysfunction.

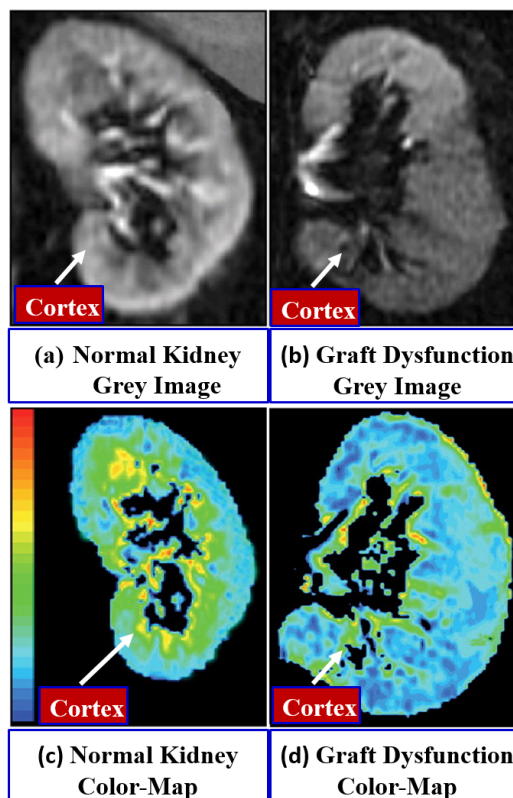


FIGURE 7: A simple demonstration of grey and $R2^*$ colored images for a normal kidney and a kidney with graft dysfunction.

In particular, Djamali et al. [111] investigated the ability of BOLD-MRI to assess

renal allografts. In their study, 23 patients underwent BOLD-MRI scans, of which 5 were normal allografts and 18 had acute allograft dysfunction (5 with ATN and 13 with AR). Medullary and cortical ROIs were placed, and mean cortical (CR2*), medullary (MR2*), and medullary to cortical (MCR2*) were calculated. They found that MR2* and MCR2* values of patients with ATN and AR were significantly decreased more than those with normal allografts. However, no differences in CR2* values between the different groups were observed. In a similar study by Han et al. [112], BOLD-MRI was conducted to differentiate between patients with AR and ATN after transplantation. Their study included 110 patients, 82 with normal allografts (group 1) and 28 with kidney dysfunction, including 21 with AR (group 2) and 7 with ATN (group 3). Group 2 was divided into two subgroups: 13 patients with T-cell-mediated rejection (TMR) and 8 patients with antibody-mediated rejection (AMR). Manual ROIs were placed in the cortical and medullary regions, and CR2*, MR2*, and MCR2* were compared between different groups. They performed a statistical analysis, and they found that values of CR2*, MR2*, and MCR2* of group 2 were reduced compared to those of the other two groups. Contradictory to the Djamali et al. [111] study, they found that values of MR2* of group 3 were higher than those of group 1. However, no significant difference was observed between the TMR and AMR subgroups.

Sadowski et al. [113] employed BOLD-MRI to assess kidney transplants. Manual cortical and medullary ROIs were placed on 17 patients who underwent BOLD-MRI scans, and these patients were divided into three groups: 5 patients with normal allografts (group 1), 4 with ATN (group 2), and 8 with AR (group 3). The MR2* and CR2* were calculated in the same way as was done in their previous study [111], and compared between the different groups. Specifically, MR2* values of group 3 allografts were decreased compared to those of group 1 and group 2, while no significant difference was observed in MR2* values between group 1 and group 2. However, no difference was detected in CR2* values among the three groups. Another interesting study by Liu et al. [110] was investigated to detect renal allograft rejection using BOLD-MRI. A total number of 50 patients with renal allografts were included and divided into three groups as 35 patients with normal allografts

(group 1), 10 patients with AR (group 2), and 5 patients with ATN (group 3). After cortical and medullary ROIs placement, CR2* and MR2* were measured to assess the three groups. Group 2 had the lowest MR2*, while no significant difference was detected in CR2* values among the three groups.

Although BOLD-MRI is a valuable imaging technique that has been investigated by some researchers in detecting renal allografts dysfunction, BOLD-MRI remains challenging, not only because of the low signal-to-noise ratio (SNR) and the weakness of the electromagnetic fields [114], but also the limited applicability of renal BOLD-MRI due to kidney motions and susceptibility induced by bowel gas which may lead to impaired image quality [115].

c. Diffusion-Weighted (DW) MRI: Recently, DW-MRI has become a subject of extensive research as an emerging imaging modality for renal function assessment thanks to DW-MRI's ability to provide both anatomical and functional information, while avoiding radiation exposures (like CT) and contrast agents administration (like DCE-MRI). For DW-MRI, its functional parameter, called apparent diffusion coefficient (ADC), is estimated from different gradient field strengths and duration (b -values), as shown in Figure 8, to describe the unique tissue characteristics of inner spatial water behavior [115]. Therefore, several studies have utilized DW-MRI to assess renal functionality by measuring the ADC values, but the results have varied [110].

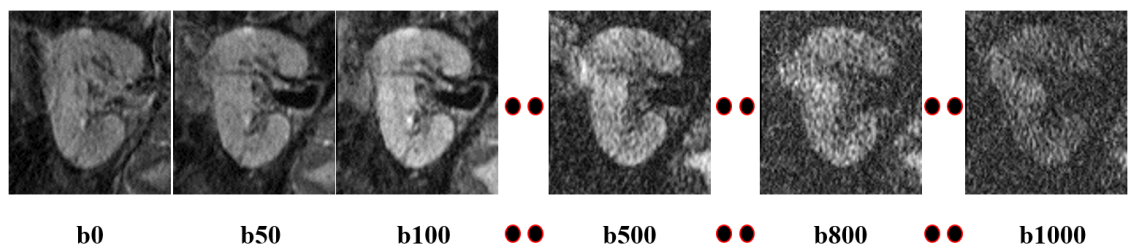


FIGURE 8: A demonstration of a DW-MRI sequence at different b -values.

Eisenberger et al. [116] investigated the manually placed ROIs in the upper, middle, and lower poles of the cortex and medulla on several slices to cover large regions of the allograft. Means and standard deviations of the ADC from all b -values were measured. The

ADC combines the perfusion free ADC and microcirculation parameters, quantified with perfusion fraction, F_p . These parameters were significantly reduced in the cortex and the medulla for the AR and ATN cases, and their values correlated with the creatinine clearance (CrCl). Similarly, a recent study by Hueper et al. [117] included 64 patients with renal allografts, of which 33 were patients with initial graft function (IniGF) and 31 were patients with DGF. These patients underwent DW-MRI scans at two b -values (0 and 600 s/mm^2). After placement of manual ROIs and estimation of renal diffusion parameters, including ADC and F_p , they concluded that renal diffusion parameters were significantly reduced in patients with DGF and their values well correlated with renal function and renal allograft fibrosis in biopsy specimens. The feasibility of diagnosing the acute renal transplant rejection (ARTR) from the DW-MRI was evaluated by Xu et al. [118] on 26 biopsy-proven rejection and 43 non-rejection patients. The non-rejection patients showed higher ADCs than those of the rejection group, and also demonstrated the best sensitivity and specificity at the b -value of 800 s/mm^2 , as was evinced by the ROC curve. Palmucci et al. [119] evaluated functionality of 21 transplanted kidneys by comparing the estimated ADCs and true diffusion (TD) with renal function indices. Patients were divided into three groups by their CrCl values. The cortical ADC and TD were evaluated in a user-defined ROI of the transplanted kidney for the three groups. A moderate positive correlation between the CrCl and both the ADC and TD, as well as no difference between the ADC and TD values for the adjacent groups, has been found. The subsequent extension [120] of these evaluations to 35 patients revealed a slightly smaller positive correlation than the previously reported one [119]. However, acute rejection responses after transplantation could not be detected.

Vermathen et al. [121] assessed renal functionality by determining long-term (3 years) stability and potential changes for renal allograft recipients. After selecting cortical and medullary ROIs, the ADC had been calculated from all b -values. For good allograft, a significant correlation between different ADC components was observed, whereas for reduced allograft, the F_p values were the highest, and the medullary F_p had the greatest changes. Katarzyna et al. [122] investigated possible relations between the selected laboratory results and diffusion parameters in the early period after kidney transplantation by mea-

asuring additional exponential ADCs to overcome the DW-MRI T2-“shine-through” [123]. The measurements were conducted in the kidney’s cortex and medulla over multiple user-defined ROIs at the b -values of 600 and 1000 only. According to relative variability of results and SNR, the best-quality ADC measurement in the renal cortex was at the b -value of 1000 s/mm^2 . Also, there were strong dependencies between the ADC and exponential ADC, measured in the renal cortex at b_{1000} s/mm^2 , and the estimated GFR. Kaul et al. [124] assessed the renal dysfunction with cortical and medullary ADC maps. They reported a significant decrease in the ADC values of medullas compared to those of cortices in normal donor kidneys and normally functioning transplanted kidneys. Both the medulla and cortex ADCs decreased or increased significantly for a rejection or the recovery from the rejection itself, respectively. A recent study by Abou-El-Ghar et al. [125] included 70 renal allograft patients who underwent DW-MRI scans at two b -values (0 and 800 s/mm^2). In this case, 49 patients had stable renal allograft function (group 1) and 21 patients had acute graft impairment (group 2: 10 acute cellular rejection (ACR), 7 ATN, and 4 ITox rejection types). An ROI was placed at the middle of the kidney in a single cross-section and a pixel-wise ADC was calculated. They have shown that the ADC values of group 1 were significantly higher than those of group 2, and no overlap was detected between the ADCs of group 1 and the ATN patients of group 2. However, the minimal overlap was observed between the ADCs of group 1 and the patients with the ACR and IT of group 2. Recently, Liu et al. [110] detected an early renal allograft dysfunction caused by AR and ATN using the DW-MRI and BOLD-MRI with manually selected cortical and medullary ROIs. Their study revealed lower values of both the measured apparent relaxation rates and ADC for the AR group than for the control groups, and no difference in the ADC values for the AR and ATN groups. A similar earlier study was conducted by Thoeny et al. [126].

F. Chapter Summary

Though the treatment of chronic kidney disease has improved greatly with the use of transplants, there are still challenges such as graft dysfunction that provide a challenge in maintaining survival of the new organ. In the future, the use of image-based diagnosis will be improved and implemented in the diagnosis of both pre- and post-transplantation. It is hoped that by having these improved imaged based CAD systems that diagnosis of graft dysfunction, along with the cause of graft dysfunction, will be less invasive, more accurate, time saving, and inexpensive compared to renal biopsies and other traditional methods of diagnosis. By having all of these advantages it is expected that graft survival will improve in cases of graft dysfunction.

G. Thesis Organization

This thesis is presented in three chapters. The scope of each chapter is summarized as follows:

1. Chapter I

This chapter overviews the existing traditional clinical methods and the current image-based techniques which are used to evaluate and assess renal transplants functionality and to detect early signs of graft dysfunction. Additionally, a brief overview is given in this chapter including: kidney anatomy and functionality, the risk of developing chronic kidney disease (CKD) and some symptoms associated with it, an overview of the treatment options for people that develop stage 5 CKD, transplantation procedure as a definitive therapy for these people with stage 5 CKD, and post transplantation follow-ups which includes possible complications that could arise with a concentration on graft dysfunction. This is followed by the traditional tests that are performed to detect graft dysfunctions such as blood, urine, and renal biopsy. Finally, the state-of-the-art image based techniques which are used in renal transplants' evaluation and assessment are discussed. These im-

age techniques include: ultrasounds (US) (e.g., conventional, power doppler (PD), color doppler (CD), contrast enhanced (CE), etc.) , and magnetic resonance imaging (MRI)(e.g., dynamic contrast enhanced (DCE), blood oxygen level-dependent (BOLD), and diffusion-weighted (DW)).

2. Chapter II

This chapter presents a new computer-aided diagnostic (CAD) system for the early detection of acute renal transplant rejection (ARTR) using diffusion-weighted (DW) MRI. The developed CAD system demonstrates multiple novelties including: *(i)* segmenting kidneys from the DW-MRI data in a fully automated mode using geometric deformable models; *(ii)* describing kidney functionality with the cumulative distribution function (CDF) of the ADCs; and *(iii)* discriminating between rejection and non-rejection renal transplants with a deep neural network learned by stacking layers of several auto-encoders with non-negativity constraint (NCAE).

3. Chapter III

This chapter concludes the thesis, highlights the main contributions and obtained results, and discusses the trend for possible future avenues to be handled.

CHAPTER II

COMPUTER-AIDED DIAGNOSTIC SYSTEM FOR EARLY DETECTION OF ACUTE RENAL TRANSPLANT REJECTION USING DIFFUSION-WEIGHTED MRI

A. Introduction

Due to the fact there are up to 17,000 renal transplants per annum in the U.S. and a limited number of donors [127], the salvage of a transplanted kidney is of serious clinical concern. The immunological response of a patient's body to a transplanted kidney, called the acute renal transplant rejection (ARTR), is considered to be the leading cause of renal dysfunction [127] after the transplantation. An early detection of renal dysfunction increases the survival rate of the transplanted kidney [110, 125], as confirmed by clinicians. Therefore, calling for essential medical biomarkers to assess renal transplants, especially at an early stage, (i.e. before major changes in creatinine clearance (CrCl) and serum plasma creatinine (SPCR) are detected), is very necessary to distinguish the ARTR from other diagnoses, including the acute tubular necrosis (ATN) and immune drug toxicity.

Traditional blood tests and urine sampling to evaluate renal transplant dysfunction cannot assess function of individual kidneys. The glomerular filtration rate (GFR) is based on measuring the serum creatinine level and has been approved by the National Kidney Foundation (NKF) to evaluate the overall kidney function. The GFR is a relatively imprecise and late marker for renal dysfunction (a significant change in creatinine levels is only detectable after losing 60% of renal function) [6]. Biopsy, which remains the gold standard for renal transplant assessment, is an invasive procedure with a high cost and morbidity rate, and relatively small needle biopsy samples may over- or under-estimate an inflammation extent in the entire graft [127]. More favorable non-invasive imaging tests provide separate information on each kidney. However, the most frequent scintigraphy, preferred for

its good functional information, has too low spatial resolution [128] and exposes patients to a small dose of radioactivity because of reliance on gamma-cameras [129]. Computed tomography provides superior functional and anatomical information, but uses nephrotoxic contrast agents and exposes patients to radiation as well [128]. These shortcomings have been circumvented recently by evaluating kidney functions with magnetic resonance imaging (MRI). For example, the dynamic contrast-enhanced (DCE) MRI has been exploited for renal function assessment due to providing both anatomical and functional kidney information [91, 92, 96, 109]. However, because the contrast agents may cause the development of nephrogenic systemic fibrosis, many medical centers are reluctant in applying the DCE-MRI to patients with renal disease [101].

In order to circumvent this major drawback, diffusion-weighted (DW) MRI has been exploited as an emerging imaging modality for renal function assessment. The DW-MRI measures unique tissue characteristics of inner spatial water behavior, namely, its apparent diffusion coefficients (ADC). In this chapter, a CAD system for the early detection of ARTR using DW-MRI is developed, thanks to DW-MRI's ability to provide both anatomical and functional information, exposes patients to no radiation, and needs no contrast agents, like the DCE-MRI. The proposed CAD system demonstrates multiple novelties including: (i) segmenting kidneys from the DW-MRI data in a fully automated mode (Section II.B.1); (ii) describing kidney functionality with the cumulative distribution function (CDF) of the ADCs (Section II.B.2); and (iii) discriminating between kidney rejection and non-rejection with a deep neural network learned by stacking layers of several auto-encoders with non-negativity constraint (NCAE) (Section II.B.3). Section II.A.1 below briefly outlines state-of-the-art techniques in DW-MRI segmentation, followed by Section II.A.2 which reviews the prior work on assessing the renal transplant function using the ADCs.

1. Prior Work on DW-MRI Segmentation

The process of segmenting kidneys from the DW-MRI has not been addressed yet. In literature, only known applications to other anatomical structures, such as the brain, the

prostate, and the liver, can be reviewed.

Brain segmentation. To segment the brain tissue in a fully automated mode, Yap et al. [130] used voxel-wise compartmental coexistence modeling of various diffusion features. After possible signal contributions from different brain tissues are assigned to each voxel using diffusion exemplars, each voxel is classified in accordance with the least fitting residual. Mujumdar et al. [131] segmented stroke lesions by using the Chan-Vese [2] deformable boundary guided with the Mumford-Shah functional. An automated window-based noise suppression at high b -values was conducted to enhance local contrast of the candidate lesions. Automated region growing by Saad et al. [132, 133] integrated homogeneity criteria and simple statistical regional features, such as the mean signal intensity and the number of pixels. However, both this approach and its semi-automated variant could not fully characterize the tumor lesion. Saad et al. [134] explored an automatic brain lesion segmentation, which starts from the DW-MRI normalization, background removal, and enhancement. Then both regional and boundary information, combined with statistical texture descriptors extracted from a collected gray level co-occurrence matrix, were used to guide the segmentation of brain lesions (e.g., hyperintense or hypointense). To segment near-tubular fiber bundles from the DW-MRI, Niethammer et al. [135] performed global statistical diffusion orientation modeling that utilized optimal paths or simple streamlining to obtain geometric information. Convex approximation of the probabilistic Chan-Vese energy [2] was employed using region-based directional statistics.

Prostate segmentation. McClure et al. [136] used geometric (level-set-based) deformable boundaries and nonnegative matrix factorization (NMF) for an automated prostate segmentation from the DW-MRI. The NMF integrated the DW-MRI intensity, a prostate shape prior, and pairwise spatial interactions between the prostate voxels. The like segmentation and maximum *a posteriori* decisions were used by Firjani et al. [137] for early detection of prostate cancer. An unsupervised level-set-based prostate segmentation by Liu et al. [138] applies a shape penalty term described by an elliptical deformable boundary to initialize and constrain the level-set function. The latter is then refined by connectivity and morphological analysis. Subsequently, their framework was extended to account for the 3D ADC

images derived from the original DW-MRI [139]. After an initial coarse segmentation, a shape prior weighting parameter is selected automatically, and refining morphological operations are performed to obtain the final segmentation map. Ozer et al. [140] tuned thresholds of support vector machines (SVM) and relevance vector machines (RVM) to classify “multispectral” MRI data, e.g., dynamic MRI, quantitative T2 MRI, and DW-MRI, for automated prostate segmentation in accordance with an user-defined performance criterion, such as optimal accuracy, maximal sensitivity, etc. Then, the best performance was obtained by using a first-order polynomial kernel in the SVMs and RVMs. A fuzzy Markov random field (MRF) modeling of the like multispectral MRI prostate data allowed Liu et al. [141] to simultaneously perform an unsupervised prostate segmentation and MRF parameter estimation.

Liver segmentation. Veeraraghavan et al. [142] applied simultaneous segmentation and iterative registration to the liver DW-MRI data. At each iteration, the rigid global affine registration is followed by the the fine non-rigid *B*-spline-based registration. A sequence of transformations is used to most accurately align the individual *b*-value images to the reference image, the modified Housdorff distance (MHD) being a similarity metric. Then, a GrowCut optimization segments the whole volume of interest after one or more 2D slices were manually segmented in the reference image. Stephen et al. [143] developed a semi-automated lesion segmentation and ADC estimation. For every given set of patient images, a large rectangular ROI is created only once manually by the analyst in one of the images, ensuring that the lesion is within the ROI in all of the images for all the *b*-values and some pixel within the lesion region is marked as a seed. For each image, an empirical probability distribution pixel intensities inside the ROI is approximated with a finite Gaussian mixture (FGM), a Markov-Gibbs random field (MGRF) model is built to quantify spatial pixel-to-pixel dependencies (interactions), and these two statistical descriptors are combined to segment the lesion within the ROI for each image. To improve the segmentation, geometric convexity constraints of a lesion are taken into account. A semi-automated joint liver segmentation and alignment framework by Veeraraghavan and Do [144] begins from a sequential least-squares alignment of the images. Then various structures in a randomly

selected reference image are manually segmented, starting from user-drawn lines on these structures. The closest image, selected with mean-shift tracking and aligned to the reference image using non-rigid B-spline-based deformations, is selected as the new reference image, and the process is repeated for all remaining images in the sequence. Jha et al. [145] developed an automated statistical clustering approach for segmenting liver lesions. The DW-MRI intensity distribution is approximated by an FGM, such that its number of Gaussian components (classes) is determined by measuring the approximation error, and an MRF model is used to quantify spatial pixel interactions, as well.

2. Prior Work on Renal Function Assessment

Prior related work on renal function assessment using DW-MRI has been covered in details in Chapter I (Section I.E.4.c).

In total, several clinical studies have been conducted for the assessment of renal function. However, they have some limitations. All the approaches employ manual delineation of the kidney using 2D ROIs, which is subjective and depends on user knowledge of anatomy. In addition, these methods did not compensate for the kidney motion since they did not account for the entire kidney. Furthermore, several of these studies performed only statistical analysis to investigate the significant difference between pairs at certain b -values and did not integrate all the analysis steps into a whole framework to build a fully automated CAD system. Finally, the studies mentioned above did not investigate the fusion of ADCs at multiple low and high b -values.

As an initial idea to overcome these limitations, a recent study to distinguish between rejection and non-rejection renal transplants was made by [146]. Their study included 36 renal transplants of which 6 were non-rejection and 30 were rejection. After DW-MRI data motion correction using a 2D B-splines approach, they segmented the largest coronal cross-section of the kidney using a fully automated level sets segmentation approach. Then, they calculated the ADCs at different b -values from the segmented coronal cross-section for each subject. By using a leave-one-subject-out scenario along with

a KStar classifier, they got a 87% total classification accuracy. In addition, they depicted color-maps from the calculated ADCs for the visualization purpose at different b -values. However, this study did not compensate for kidney motion as it did not account for the entire kidney volume. In addition, it did not investigate the fusion of multiple ADCs at multiple low and high b -values for the entire kidney volume.

These initial promising diagnostic results obtained by [146] was the trigger to extend this work to overcome all of the aforementioned shortcomings. Therefore, a 4D (3D + b -value) fully automated CAD system has been developed [147, 148], shown in Figure 9, which is able to: (i) delineate the whole kidney and handle its motion; (ii) fuse the ADC values calculated from the segmented DW-MRI data sets acquired at multiple low and high b -values; (iii) describing kidney functionality with the CDFs of the ADCs; and (iv) discriminating between kidney rejection and non-rejection with a deep neural network learned by stacking layers of several auto-encoders with non-negativity constraint (NCAE). Experimental results hold promise for the developed CAD system as a reliable non-invasive diagnostic tool.

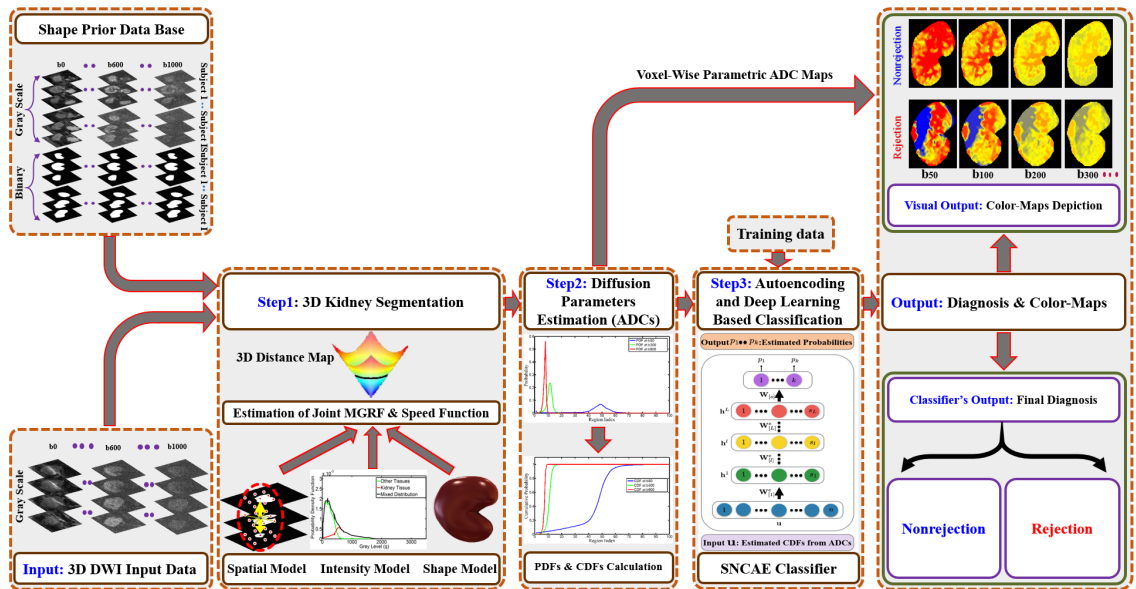


FIGURE 9: Proposed CAD system for detecting renal rejection from 4D DW-MRI.

B. Methods

Given an input 4D (3D + b -value) DW-MRI, the proposed CAD system, shown in Figure 9, performs the following steps: (i) segments kidneys from surrounding abdominal structures (Section II.B.1); (ii) estimates voxel-wise functional parameters (ADCs) to form a 3D parametric map for detecting status of the transplanted kidney (Section II.B.2); and (iii) classifies acute rejection or non-rejection transplant status in order to evaluate the system as a diagnostic test (Section II.B.3).

1. 3D Kidney Segmentation

Since the segmentation is a key step in developing any CAD system, the presented CAD starts with segmenting the kidney from the surrounding tissues using DW-MRI. However, accurate kidney segmentation is a challenging task for many reasons, including: kidney motion due to breathing and heart beating; kidney shape changes due to inter-patient anatomical differences; low contrast between the kidney and other abdominal structures, especially, at the higher gradient strengths and duration, or b -values (Figure 10); low SNR and artifacts that complicate image alignment [149, 150]; and geometric distortions due to long acquisition time [130].

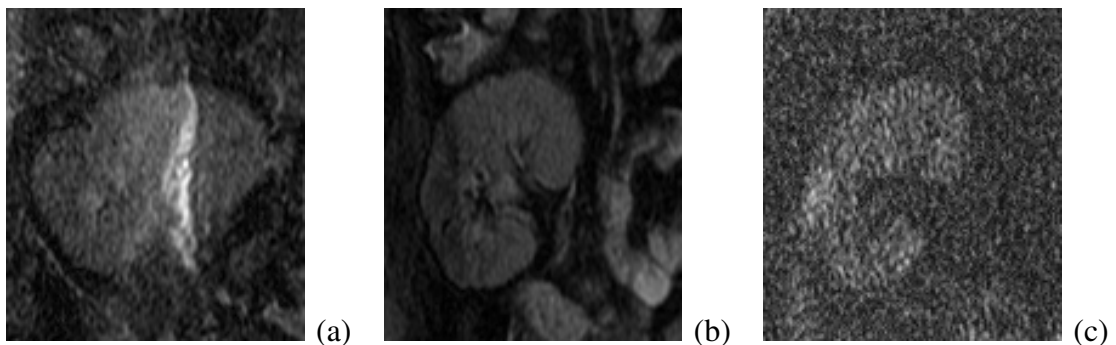


FIGURE 10: Coronal cross-sections of raw DW-MRI samples showing (a) similar intensities of kidney and surrounding tissues (e.g., at b_0), (b) inter-patient anatomical differences (e.g., at b_0) compared to the cross-section (a), and (c) image noise, especially, at higher gradient strengths and duration (b -values) (e.g., at b_{1000}).

To overcome these challenges, the proposed segmentation technique [146, 151–153] relies on multiple image features to accurately delineate the kidney and thus facilitates further analysis of transplant status. Basic notations and details of the proposed segmentation approach are outlined below.

For describing these processing steps, let $\mathbf{p} = (x, y, z)$ denote a voxel at position with discrete Cartesian coordinates (x, y, z) and let $\mathbf{R} = \{(x, y, z) : 0 \leq x \leq X - 1; 0 \leq y \leq Y - 1; 0 \leq z \leq Z - 1\}$ be a finite 3D arithmetic lattice of unit voxels, which has the size of XYZ and supports both grayscale images and their parametric or region (segmentation) maps. A grayscale image, $\mathbf{g} = \{g_{\mathbf{p}} : \mathbf{p} \in \mathbf{R}; g_{\mathbf{p}} \in \mathbf{Q}\}$, takes voxel values from a finite set, $\mathbf{Q} = \{0, 1, \dots, Q - 1\}$, of Q integer gray levels, i.e. $g : \mathbf{R} \rightarrow \mathbf{Q}$. A region map, $\mathbf{m} = \{m_{\mathbf{p}} : \mathbf{p} \in \mathbf{R}; m_{\mathbf{p}} \in \mathbf{L}\}$, takes voxel values from a binary set of region labels, $\mathbf{L} = \{0, 1\}$, where 0 and 1 indicate background and object (kidney), respectively, i.e. $m : \mathbf{R} \rightarrow \mathbf{L}$.

A 3D geometric, or level-set-based deformable boundary, is employed in the proposed CAD system for the DW-MRI kidney segmentation. Such a tool is common and successful in a wide range of applications, including various medical imaging tasks, e.g., segmenting brain, prostate, liver, kidney, etc. [104]. Compared to alternative parametric deformable boundaries, the geometric ones are more popular due to their simplicity, flexibility, and ability to handle complex geometries and topological changes independently of surface parameterizations. Points of an object-background boundary at each time instant t are specified implicitly as a zero-level set, $B_t = \{\mathbf{p} : \mathbf{p} \in \mathbf{R}; \Phi(\mathbf{p}, t) = 0\}$, of arguments of a specific higher-dimensional function $\Phi(\mathbf{p}, t)$, being supported by the lattice \mathbf{R} and often called a signed distance map:

$$\Phi(\mathbf{p}, t) = \begin{cases} d(\mathbf{p}, B_t) & \text{if } \mathbf{p} \text{ is inside the boundary } B_t; \\ 0 & \text{if } \mathbf{p} \text{ is at the boundary } B_t, \text{ and} \\ -d(\mathbf{p}, B_t) & \text{if } \mathbf{p} \text{ is outside the boundary } B_t \end{cases}$$

Here, $d(\mathbf{p}, B_t) = \min_{\mathbf{b} \in B_t} d(\mathbf{p}, \mathbf{b})$ denotes the distance from the point \mathbf{p} to the boundary B_t , and $d(\mathbf{p}, \mathbf{b})$ is the Euclidean distance between the lattice points \mathbf{p} and \mathbf{b} , as illustrated in Figure 11.

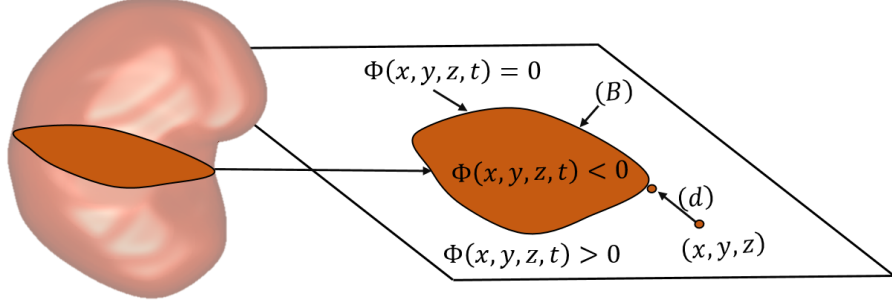


FIGURE 11: 3D zero-level set of a function $\Phi(\mathbf{p} = [x, y, z], t)$.

The function $\Phi(\mathbf{p}, t)$ evolves in discrete time $t = n\tau$ with a fixed step, $\tau > 0$, as [154]:

$$\Phi(\mathbf{p}, (n + 1)\tau) = \Phi(\mathbf{p}, n\tau) - \tau F_n(\mathbf{p}) |\nabla \Phi(\mathbf{p}, n\tau)| \quad (1)$$

where $n = 0, 1, 2, \dots$, is the time index; $\nabla \Phi(\mathbf{p}, n\tau)$ is the spatial gradient of $\Phi(\mathbf{p}, n\tau)$:

$$\nabla \Phi(\mathbf{p}, n\tau) = \left[\frac{\partial \Phi(\mathbf{p}, n\tau)}{\partial x}, \frac{\partial \Phi(\mathbf{p}, n\tau)}{\partial y}, \frac{\partial \Phi(\mathbf{p}, n\tau)}{\partial z} \right];$$

$|\mathbf{a}|$ denotes the magnitude of the vector \mathbf{a} , and $F_n(\mathbf{p})$ is a speed function guiding the evolution of an initial boundary B_0 , which was defined at the starting instant $t = 0$ (i.e. $n = 0$).

Most of the conventional speed functions quantify visual appearance differences between the object and its background in terms of mean values and variances of image intensities, intensity edges or gradient vector flow, and similar regional signal characteristics. Thus, their guidance may fail if images to be segmented are noisy and/or object-background contrast is low. To accurately segment the kidneys from the noisy and low-contrast DW-MRI, the developed guiding function accounts for not only regional kidney-background appearance, but also for a kidney shape prior and spatial relationships of the goal region map. To provide the voxel-wise guidance for the evolving boundary, all the employed appearance and shape descriptors are combined into a joint MGRF model of a DW-MR image, \mathbf{g} , and its binary kidney-background region map, \mathbf{m} . The model is specified by a joint probability distribution $P(\mathbf{g}, \mathbf{m}) = P(\mathbf{g}|\mathbf{m})P(\mathbf{m})$, where $P(\mathbf{g}|\mathbf{m})$ and $P(\mathbf{m})$ denote a conditional probability distribution of images given a map and an unconditional distribution of region maps, respectively. The latter distribution is factored into two terms: $P(\mathbf{m}) = P_{\text{sp}}(\mathbf{m})P_{\text{V}}(\mathbf{m})$, where $P_{\text{sp}}(\mathbf{m})$ denotes an appearance-based adaptive shape prior

and $P_V(\mathbf{m})$ is a second-order Gibbs probability distribution with potentials \mathbf{V} of multiple nearest-neighbor pairwise dependencies, which specifies a simple spatially homogeneous MGRF model of region maps. These components of the joint image-map model are outlined in the following Sections.

a. Appearance-Based Shape Prior: In addition to the distinct visual appearances, the well-known geometric shapes of medical structures can enhance the segmentation accuracy. To rely on this fact, an adaptive model of the expected kidney shape is used to both handle kidney motions, e.g., due to breathing and/or heart beating, and account for the kidney's variability due to inter-patient anatomical differences. In addition, the kidney DW-MR images are very noisy, especially at high b -values, and have low contrast between the kidney tissue and other abdominal structures. The noise and inconsistencies due to low-frequency non-uniformity, or heterogeneity of intensities, are suppressed in part by preprocessing, namely, histogram equalization with nonparametric bias correction by Tustison [155] shown in Figure 12.

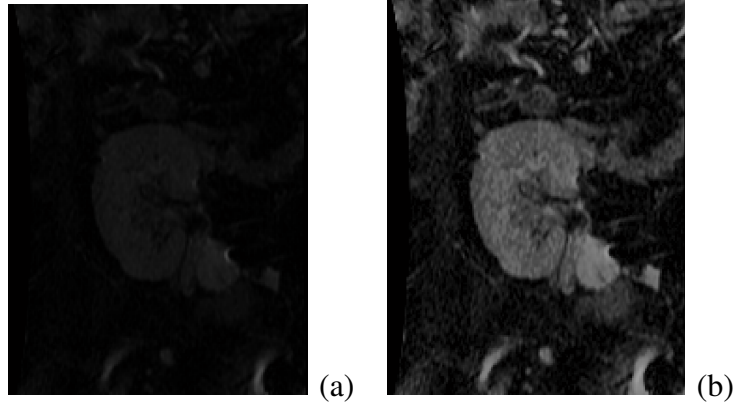


FIGURE 12: Raw coronal DW-MRI cross-section before (a) and after (b) its preprocessing.

To build the shape prior, a shape database is created from a training set of manually delineated kidney images from different subjects by co-aligning these images using a 3D B-spline-based non-rigid transformation [156]. The alignment minimizes the sum of squared voxel-wise intensity differences between the two kidney images, and kidney/background labels of the co-aligned region maps are used to learn the shape prior. Figure 13 illustrates the co-alignment of the training DW-MRI with respect to a single reference image.

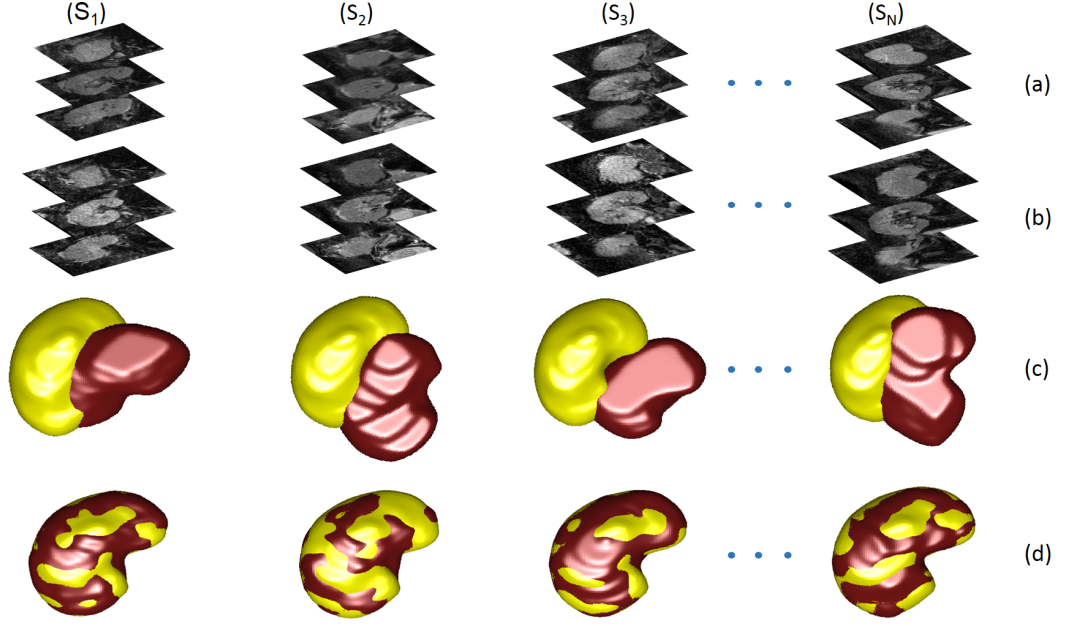


FIGURE 13: 3D co-alignment of training DW-MRI to a single reference: grayscale images before (a) and after (b) their alignment and overlapped 3D binary volumes before (c) and after (d) alignment, the reference image and targets being in yellow and red, respectively.

In the performed experiments, the shape database contained 53 data sets (b_0 -scans) manually segmented by an MRI expert and then co-aligned. Adapting the shape prior to each input DW-MR image to be segmented is guided by visual appearance of the latter image. The probabilistic shape prior is built as a spatially variant independent random field of region labels $P_{\text{sp}}(\mathbf{m}) = \prod_{\mathbf{p} \in \mathbf{R}} \text{Pr}_{\mathbf{p}}(m_{\mathbf{p}})$, where $\text{Pr}_{\mathbf{p}}(l)$ is the marginal empirical probability of the label $l \in \mathbf{L}$ in the voxel \mathbf{p} ; $\sum_{l \in \mathbf{L}} \text{Pr}_{\mathbf{p}}(l) = 1$. Algorithm summarizes estimating and updating the appearance-guided shape prior for each test DW-MR image to be segmented (the test images are first removed from the training set).

b. Second-Order MGRF Model of Region Maps: In order to increase the segmentation accuracy, 3D pairwise dependencies between the region labels are additionally incorporated in the proposed model by using a popular Potts MGRF [157]. Here, it is a spatially homogeneous binary field with the nearest 26-voxel neighborhoods and analytically estimated bi-valued Gibbs potentials depending only on whether or not the nearest pairs of labels are equal. Let f_{eq} denote the empirical marginal probability of equal labels

Algorithm 1 Creating / Updating the Shape Prior.

- 1 Preprocess the training DW-MR images by bias correction and histogram equalization.
 - 2 Construct the shape database by applying the co-alignment by Glocker et al. [156] to the preprocessed DW-MR Images.
 - 3 Preprocess the DW-MR image for a test subject and co-align with the shape database.
 - 4 For each voxel, $\mathbf{p} \in \mathbf{R}$, in the test DW-MR image, \mathbf{g}_{test} , calculate its prior shape probabilities, $\text{Pr}_{\mathbf{p}}(l); l \in \mathbf{L}$, as follows:
 - A Use the co-aligning deformation field to relate the voxel \mathbf{p} of the test image to the shape database lattice.
 - B Construct a 3D window with initial size of $N_1 \times N_2 \times N_3$, centred at the related voxel in the shape database lattice.
 - C Find within the window all the voxels with the corresponding intensity, $g_{\text{test};\mathbf{p}}$, in all the training images.
 - D If necessary, increase the window size and repeat Steps 4B to 4D until a non-empty set of such corresponding training intensities is found.
 - E Estimate label probabilities based on relative occurrences of each label in all the training voxels found.
-

in the neighboring voxel pairs $(\mathbf{p}, \mathbf{p} + \boldsymbol{\delta}) \in \mathbf{R}^2; \boldsymbol{\delta} \in \mathbf{N}_{26} = \{(\pm 1, 0, 0), (0, \pm 1, 0), (0, 0, \pm 1), (\pm 1, \pm 1, 0), (\pm 1, 0, \pm 1), (0, \pm 1, \pm 1), (\pm 1, \pm 1, \pm 1)\}$. Given a region map \mathbf{m} (e.g., after an initial rough segmentation), the maximum likelihood estimates of the potentials

$$V(m_{\mathbf{p}}, m_{\mathbf{p}+\boldsymbol{\delta}}) = \begin{cases} V_{\text{eq}} & \text{if } m_{\mathbf{p}} = m_{\mathbf{p}+\boldsymbol{\delta}} \\ V_{\text{ne}} & \text{if } m_{\mathbf{p}} \neq m_{\mathbf{p}+\boldsymbol{\delta}} \end{cases} ; \mathbf{p} \in \mathbf{R}; \boldsymbol{\delta} \in \mathbf{N}_{26}; V_{\text{eq}} + V_{\text{ne}} = 0$$

are analytically approximated [158] as follows: $V_{\text{eq}} = -V_{\text{ne}} \approx 2f_{\text{eq}}(\mathbf{m}) - 1$. This approximation is used for computing the voxel-wise probabilities $\text{Pr}_{\mathbf{v};\mathbf{p}}(l)$ of each label; $l \in \mathbf{L}$.

c. First-Order Kidney/Background Appearance Model: To accurately model the DW-MRI appearance, the empirical marginal probability distribution of intensities is approximated with a linear combination of discrete Gaussians (LCDG) [159]. The LCDG with two positive dominant components (one each for the kidney and background) and

multiple sign-alternate subordinate components allow for separating the mixed marginal of the DW-MRI voxel-wise intensities into the two distinct LCDGs, each associated with the kidney or background label. This LCDG model adapts the segmentation to changing appearance, such as non-linear intensity variations caused by patient weight and the data acquisition system, and it separates individual submodels of the kidney and background intensities more accurately than a conventional mixture of only positive Gaussians. This adaptation yields a better initial region map after the voxel-wise classification of only the image intensities with no account for the kidney shape.

d. Appearance- and Shape-Guided Deformable Model: Adaptation to both the kidney-background visual appearance, shape prior, and statistical spatial dependencies between kidney labels is one of the main advantages of the proposed segmentation framework. Estimated directly from the input image and a given shape database, these properties guide the evolving deformable boundary by defining, for each voxel \mathbf{p} with intensity $g_{\mathbf{p}} = q$, the speed function [104] of Equation (1), $F_n(\mathbf{p}) = \kappa\vartheta_{\mathbf{p}}$, where κ is the mean contour curvature and $\vartheta_{\mathbf{p}}$ specifies the magnitude and direction of moving that voxel:

$$\vartheta_{\mathbf{p}} = \begin{cases} -\Pr_{\mathbf{p}}(1) & \text{if } \Pr_{\mathbf{p}}(1) > \Pr_{\mathbf{p}}(0) = 1 - \Pr_{\mathbf{p}}(1); \text{ i.e. } \Pr_{\mathbf{p}}(1) > 0.5; \\ \Pr_{\mathbf{p}}(0) & \text{otherwise} \end{cases} \quad (2)$$

Here, $\Pr_{\mathbf{p}}(0)$ and $\Pr_{\mathbf{p}}(1)$ are the voxel-wise background and kidney probabilities, respectively:

$$\Pr_{\mathbf{p}}(1) = \frac{\Omega_{\text{kd};\mathbf{p}}}{\Omega_{\text{kd};\mathbf{p}} + \Omega_{\text{bg};\mathbf{p}}}; \quad \Pr_{\mathbf{p}}(0) = \frac{\Omega_{\text{bg};\mathbf{p}}}{\Omega_{\text{kd};\mathbf{p}} + \Omega_{\text{bg};\mathbf{p}}} = 1 - \Pr_{\mathbf{p}}(1)$$

where the variables $\Omega_{\text{kd};\mathbf{p}}$ and $\Omega_{\text{bg};\mathbf{p}}$ for the kidney and background, respectively, depend on the voxel-wise probabilities $\Pr(q|l)$; $l \in \mathbf{L}$, for the LCDG submodels of the kidney ($l = 1$) or background ($l = 0$) appearance and on the kidney label probability in the MGRF spatial region map model, $\Pr_{\mathbf{v};\mathbf{p}}(1)$, and in the adaptive shape prior, $\Pr_{\text{sp};\mathbf{p}}(1)$, respectively:

$$\Omega_{\text{kd};\mathbf{p}} = \Pr(q|1) \Pr_{\mathbf{v};\mathbf{p}}(1) \Pr_{\text{sp};\mathbf{p}}(1); \quad \Omega_{\text{bg};\mathbf{p}} = \Pr(q|0)(1 - \Pr_{\mathbf{v};\mathbf{p}}(1))(1 - \Pr_{\text{sp};\mathbf{p}}(1))$$

Algorithm summarizes the basic steps of the 3D level-set-based kidney segmentation.

Algorithm 2 DW-MRI Segmentation by Geometric Deformable Boundary

- 1 Update the shape prior probability using Step 4 of Algorithm .
 - 2 Approximate the marginal of DW-MRI intensities with the LCDG [159] with two dominant components.
 - 3 Form an initial region map, \mathbf{m}_{ini} , using the estimated shape prior and LCDG submodes of kidney and background appearances.
 - 4 Estimate the Gibbs potentials for the spatial MGRF map model from \mathbf{m}_{ini} .
 - 5 Find the above speed function [104], $F_n(\mathbf{p})$, using results of Steps 2 to 4.
 - 6 Segment the input image, \mathbf{g} , by evolving the level-set function, $\Phi(\mathbf{p}, n\tau)$, of Equation (1) with the speed function found in Step 5.
-

2. Estimating and Depicting Diffusion Parameters

After segmenting the kidneys, their discriminatory functional features are estimated from the images and used to distinguish between rejection and non-rejection of kidney transplants. In this chapter, the ADC defined by Le Bihan [160] is used as a transplant status feature. This voxel-wise ADC is defined as:

$$\text{ADC} = \frac{1}{b_0 - b} \ln \left(\frac{g_{b:\mathbf{p}}}{g_{0:\mathbf{p}}} \right) = \frac{\ln g_{b:\mathbf{p}} - \ln g_{0:\mathbf{p}}}{b_0 - b} \quad (3)$$

where the segmented DW-MR images \mathbf{g}_0 and \mathbf{g}_b were acquired with the b_0 and a given different b -value, respectively. To reduce the noise effects on ADC estimation, the ADC at each voxel \mathbf{p} (3D location of the DW-MRI data) is calculated using a $3 \times 3 \times 3$ cube around \mathbf{p} , and $g_{0:\mathbf{p}}$ and $g_{b:\mathbf{p}}$ are represented by the average signal intensity of that cube.

It is worth noting that conventional classification methods that deal directly with the voxel-wise ADCs of the entire kidney volume as discriminative kidney features encounter two difficulties: (i) varying input data size requires either data truncation for larger kidney volumes or zero padding for smaller ones and (ii) large data volumes lead to considerable time expenditures for training and classification. In order to overcome the above challenges, the entire 3D ADC maps, collected for each subject at the 11 different b -values, is characterized by the CDFs of the ADCs, as shown in Figure 14. These descriptors are independent of the initial data size and can be quantified in accordance with the actual ac-

accuracy (signal-to-noise ratio) of the ADCs. Preliminary experiments have shown that the 1%-accuracy of measuring the ADC to within a range between the maximum and minimum ADCs for all the b -values and subjects is sufficient, as regarding the final classification accuracy. Comparing to the empirical probability distribution functions (PDFs) of the ADCs, the CDFs allow better differentiation between the PDFs across the whole range of the ADC values. The training CDFs are used for deep learning of a stacked NCAE (SNCAE) classifier detailed in Section II.B.3. Fixing the input data size to 11 for such CDFs helps to overcome the above challenges for arbitrary sizes of the original ADCs and notably accelerates the classification. Also, the estimated 3D ADCs can be displayed as voxel-wise parametric maps to be visually assessed by the radiologists.

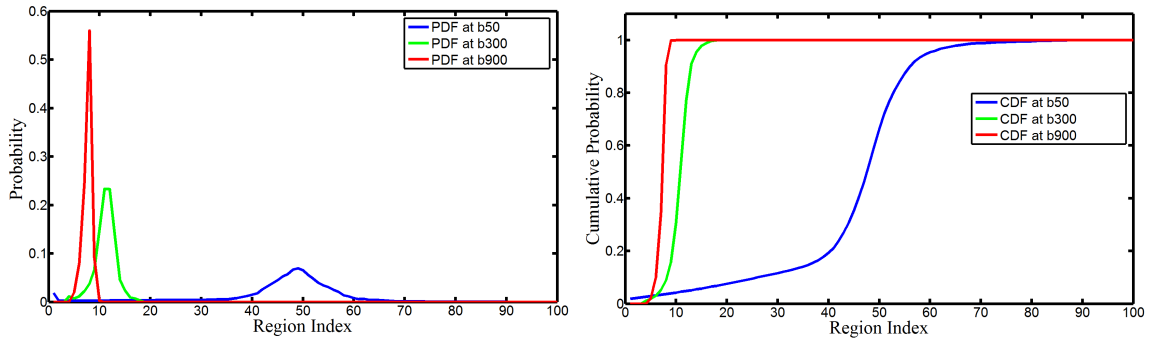


FIGURE 14: Empirical ADC distributions and their CDFs for one subject at different b -values.

3. Autoencoding and Deep Learning-Based Classifier

A rich variety of learnable classifiers with shallow structure [161–164] have been used in the CAD systems for organ transplantation prediction using clinical and demographic data of patients, including (but not limited to) artificial neural networks (ANN), support vector machines (SVMs), regression trees, random forests (RFs), decision trees (DTs), k-nearest neighbor (kNN), etc. However, the aforementioned popular learnable classifiers and predictors have some limitations [165, 166]: (i) some of them (e.g., RFs and DTs) cannot deal with very large scale amounts of data, which are typical for DW-MRI; (ii) some of them (e.g., SVMs) depend mainly on the selection of the kernel function and

its parameters; *(iii)* many classifiers (e.g., SVMs, RFs) are of high algorithmic complexity and require extensive memory.

Recent advances in deep learning of the ANNs [167] allow for overcoming these drawbacks of the classical shallow models: *(i)* by automated dimensionality reduction of large scale data [168]; *(ii)* and automatic extraction of more discriminatory features between classes through hierarchical feature extraction. In this case, the high level (global) features are derived from the low level (local) features for model training [168–171]; *(iii)* and flexibility compared to the classical shallow models, i.e. a classifier (e.g., a softmax-based or SVM-based) can be built on the extracted features from the deep learning ANN [168, 172].

Due to the aforementioned advantages, the proposed fully automated CAD system utilizes deep learning and auto-encoders with non-negativity constraint (NCAE) as a core ANN architecture for pre-training and classification to distinguish between the non-rejection and acute rejection of kidney transplants. In particular, the presented CAD system employs a deep neural network with a stack of auto-encoders (AE) before the output layer that computes a softmax regression, generalizing the common logistic regression to more than two classes. Each AE compresses its input data to capture the most prominent variations and is built separately by greedy unsupervised pre-training [173]. The softmax output layer facilitates the subsequent supervised back-propagation-based fine tuning of the entire classifier by minimizing the total loss (negative log-likelihood) for a given training labeled data. Using the AEs with a non-negativity constraint (NCAE) [174] yields both more reasonable data codes (features) during its unsupervised pre-training and better classification performance after the supervised refinement.

Let $\mathbf{W} = \{\mathbf{W}_j^e, \mathbf{W}_i^d : j = 1, \dots, s; i = 1, \dots, n\}$ denote a set of column vectors of weights for encoding (e) and decoding (d) layers of a single AE in Figure 15. Let \mathbf{T} denote vector transposition. The AE converts an n -dimensional column vector $\mathbf{u} = [u_1, \dots, u_n]^\top$ of input signals into an s -dimensional column vector $\mathbf{h} = [h_1, \dots, h_s]^\top$ of hidden codes (features, or activations), such that $s \ll n$, by a uniform nonlinear transformation of s

weighted linear combinations of signals:

$$h_j = \sigma\left(\left(\mathbf{W}_j^e\right)^\top \mathbf{u}\right) \equiv \sigma\left(\sum_{i=1}^n w_{j:i}^e u_i\right)$$

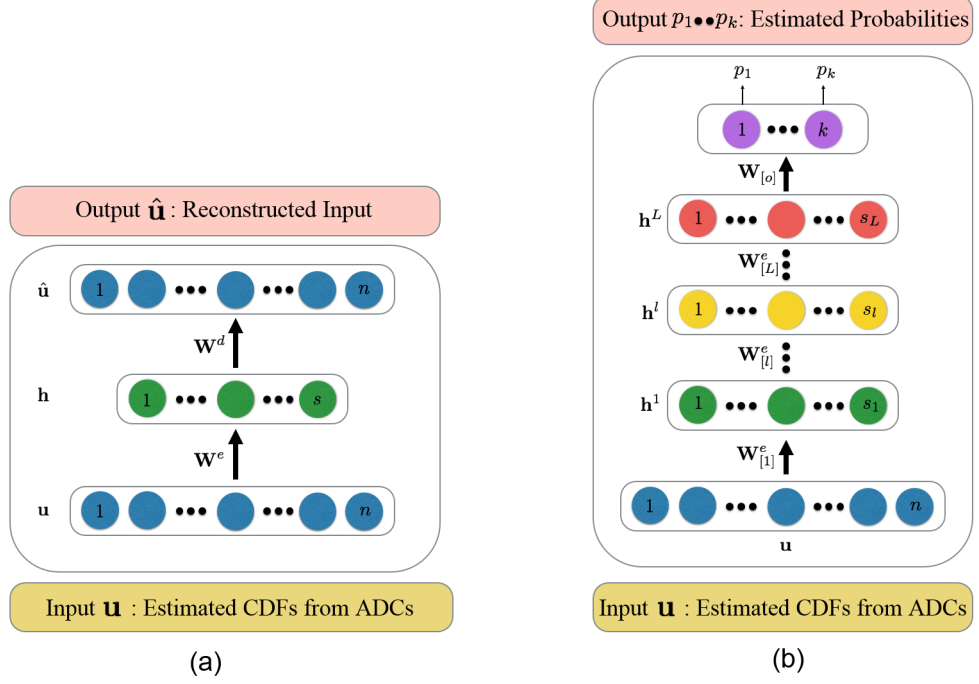


FIGURE 15: Block-diagram of an NCAE (a) and an SNCAE (b) classifier.

where $\sigma(\dots)$ is a certain sigmoid, i.e. a differentiable monotone scalar function with values in the range $[0, 1]$. Unsupervised pre-training of the AE minimizes total deviations between each given training input vector \mathbf{u}_k ; $k = 1, \dots, K$, and the same-dimensional vector, $\hat{\mathbf{u}}_{\mathbf{w}:k}$ reconstructed from its code, or activation vector, \mathbf{h}_k (Figure 15(a)). The total reconstruction error of applying such AE to compress and decompress the K training input vectors integrates the ℓ_2 -norms of the deviations:

$$J_{\text{AE}}(\mathbf{W}) = \frac{1}{2K} \sum_{k=1}^K \|\hat{\mathbf{u}}_{\mathbf{w}:k} - \mathbf{u}_k\|^2 \quad (4)$$

To reduce the number of negative weights and enforce sparsity of the NCAE, the reconstruction error of Equation (4) is appended, respectively, with quadratic negative weight penalties, $f(w_i) = (\min\{0, w_i\})^2$; $i = 1, \dots, n$, and Kullback-Leibler (KL) divergence, $J_{\text{KL}}(\mathbf{h}_{\mathbf{w}^e}; \gamma)$, of activations, $\mathbf{h}_{\mathbf{w}^e}$, obtained with the encoding weights \mathbf{W}^e for the training

data, from a fixed small positive average value, γ , near 0:

$$J_{\text{NCAE}}(\mathbf{W}) = J_{\text{AE}}(\mathbf{W}) + \alpha \sum_{j=1}^s \sum_{i=1}^n f(w_{j:i}) + \beta J_{\text{KL}}(\mathbf{h}_{\mathbf{W}^e}; \gamma) \quad (5)$$

Here, the factors $\alpha \geq 0$ and $\beta \geq 0$ specify relative contributions of the non-negativity and sparsity constraints to the overall loss, $J_{\text{NCAE}}(\mathbf{W})$, and

$$J_{\text{KL}}(\mathbf{h}_{\mathbf{W}^e}, \gamma) = \sum_{j=1}^s h_{\mathbf{W}^e:j} \log\left(\frac{h_{\mathbf{W}^e:j}}{\gamma}\right) + (1 - h_{\mathbf{W}^e:j}) \log\left(\frac{1 - h_{\mathbf{W}^e:j}}{1 - \gamma}\right) \quad (6)$$

The classifier is built by stacking the NCAE layers with an output softmax layer, as shown in Figure 15(b). Each NCAE is pre-trained separately in the unsupervised mode by using the activation vector of a lower layer as the input to the upper layer. Here, the initial input data consisted of the 11 CDFs, each of size 100, i.e. $n = 1100$. In other words, for quantizing the ADCs, the range between the minimum and maximum ADCs for all the input data sets (i.e. all the sets for 11 b -values and 53 subjects) was divided into 100 steps to keep the chosen 1%-accuracy of initial ADC measurements. The PDFs and then CDFs of the ADCs were built for these quantized values. The bottom NCAE compresses the input vector to s_1 first-level activators, compressed by the next NCAE to s_2 second-level activators, which are reduced in turn by the output softmax layer to s° values. The number of the NCAE layers and successive data compression ratios for each layer were chosen empirically, on the basis of comparative experiments.

Separate pre-training of the first and second layers by minimizing the loss of Equation (5) reduces the total reconstruction error, as well as increases sparsity of the extracted activations and numbers of the non-negative weights. The activations of the second NCAE layer, $\mathbf{h}^{[2]} = \sigma(\mathbf{W}_{[2]}^e \mathbf{T} \mathbf{h}^{[1]})$, are inputs of the softmax classification layer, as sketched in Figure 15(b) to compute a plausibility of a decision in favor of each particular output class, $c = 1, 2$:

$$p(c; \mathbf{W}_{\circ:c}) = \frac{\exp(\mathbf{W}_{\circ:c}^T \mathbf{h}^{[2]})}{\exp(\mathbf{W}_{\circ:1}^T \mathbf{h}^{[2]}) + \exp(\mathbf{W}_{\circ:2}^T \mathbf{h}^{[2]})}; \quad c = 1, 2; \quad \sum_{c=1}^2 p(c; \mathbf{W}_{\circ:c}; \mathbf{h}^{[2]}) = 1.$$

Its separate pre-training minimizes the total negative log-likelihood $J_\circ(\mathbf{W}_\circ)$ of the known training classes, appended with the negative weight penalties:

$$J_\circ(\mathbf{W}^\circ) = -\frac{1}{K} \sum_{k=1}^K \log p(c_k; \mathbf{W}_{\circ:c}) + \alpha \sum_{c=1}^2 \sum_{j=1}^{s_2} w_{\circ:c;j} \quad (7)$$

Finally, the entire stacked NCAE classifier (SNCAE) is fine-tuned on the labeled training data by the conventional error back-propagation through the network and penalizing only the negative weights of the softmax layer. In the performed experiments, the network was trained and tested based on a leave-one-out scenario, so that the 53 (by the number of subjects) test accuracies were averaged to estimate the overall accuracy of the classifier. These experiments were conducted for different structures and parameters of the classifier. At this point, the two-layer SNCAE classifier with the following parameters: $s_1 = 50$, $s_2 = 5$, $s^\circ = 2$, $\alpha = 3 * 10^{-5}$, $\beta = 3$, and $\gamma = 0.1$, is considered to give the best accuracy and was accepted as the final choice. Algorithm 3 summarizes classification of kidney transplant status and generation of color ADC maps.

Algorithm 3 Kidney Transplant Status Classification and ADC Color Mapping

- 1 Calculate, using Equation (3), the ADCs at different b -values for the entire transplanted kidney of each subject.
 - 2 Classification:
 - A Construct the CDFs of the calculated ADCs over the entire kidney volume at different b -values.
 - B Use a SNCAE-based deep ANN classifier trained by unsupervised pre-training and supervised fine tuning together with a leave-one-subject-out approach to discriminate rejection from non-rejection status and get the final diagnosis.
 - 3 Generation of color ADC maps: Generate voxel-wise color-coded maps of the ADCs calculated in Step 1 to demonstrate visually perceived differences between the rejection and non-rejection states of kidney transplants at different b -values.
-

C. Experimental Results

1. DW-MRI Data Collection

The proposed CAD system has been tested on DW-MRI data that has been collected from 53 subjects (44 men and 9 women with ages between 12 and 54 years old, having a mean age of 26 ± 10 years). Both the rejection (37 subjects) and non-rejection (16 subjects) groups, as a part of routine medical care after transplantation, were assessed with serum creatinine laboratory values. The patient who subsequently underwent an ultrasound-guided needle biopsy was examined, based on their clinical indication, as the gold standard. The DW-MR images were acquired before any biopsy procedure using a 1.5 T scanner (SIGNA Horizon, General Electric Medical Systems, Milwaukee, WI). Coronal DW-MR images have been obtained by using a body coil and a gradient multi-shot spin-echo echo-planar sequence (TR/TE, 8000/61.2; bandwidth, 142 kHz; matrix, $1.25 \times 1.25 \text{ mm}^2$; section thickness, 4 mm; intersection gap, 0 mm; FOV, 32 cm; signals acquired, 7; water signals acquired at different b -values of ($b_0, b_{50}, b_{100}, b_{200}, b_{300}, b_{400}, b_{500}, b_{600}, b_{700}, b_{800}, b_{900}$, and b_{1000}) s/mm²). Approximately 50 sections have been obtained in 60 - 120 s to cover the whole kidney.

2. Segmentation Results

Since the segmentation is an important step in developing any CAD system to assess renal function, the performance of the proposed segmentation was tested first on the collected DW-MRI data. Figure 16 shows some segmentation results for different kidney cross-sections (coronal, axial, and sagittal) for three subjects at b_0 . The segmentation accuracy was evaluated by two volumetric metrics, namely, the Dice similarity coefficient (DSC) [175, 176] and absolute kidney volume difference (AKVD) and one distance-based metric – the 95-percentile modified Hausdorff distance (MHD) [177], which characterize the spatial overlap and distribution of the surface to surface distances between the

segmented and ground truth kidneys, respectively. The ground truth kidney maps were manually outlined by an MRI expert. For completeness, these metrics are detailed in Appendix .A.

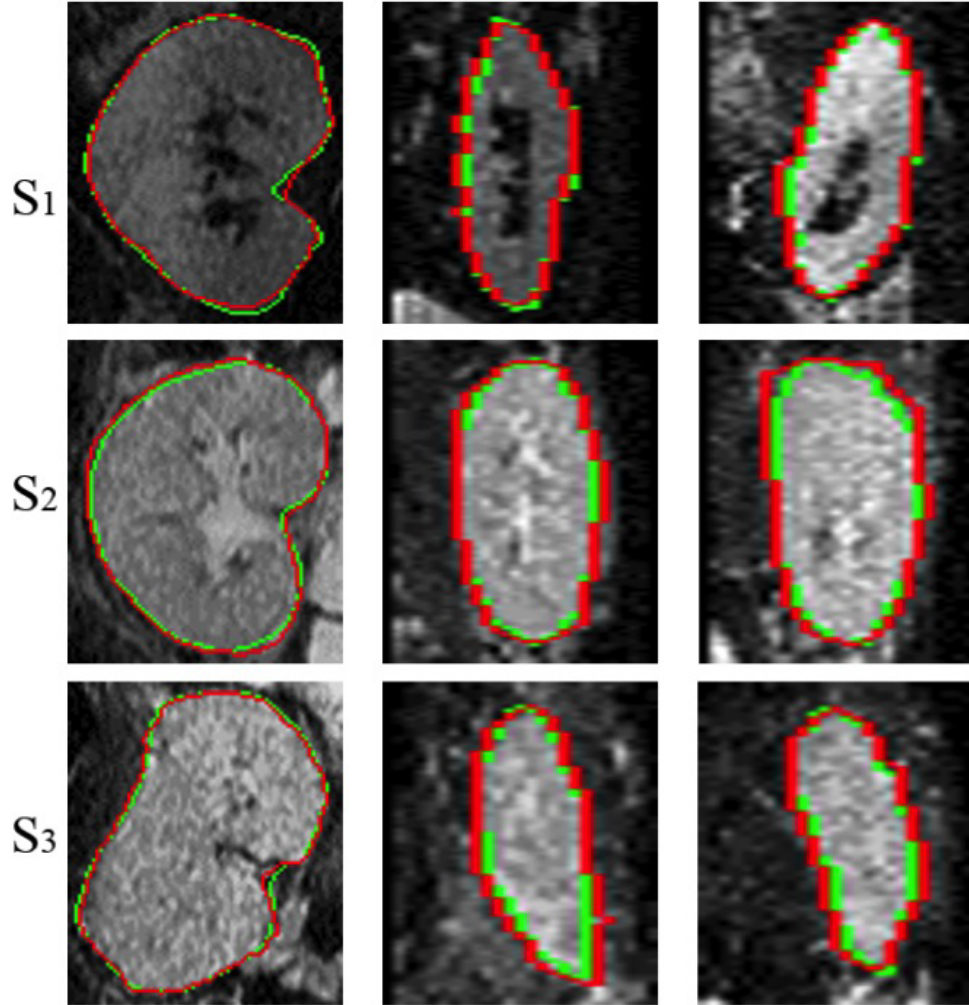


FIGURE 16: The proposed model segmentation (red) with respect to the expert’s manual ground truth (green): coronal (left column), axial (middle column), and sagittal (right column) cross sections for three different subjects, S_1 , S_2 , and S_3 .

As shown in Table 1, high accuracy of the developed segmentation method is confirmed by means of the DSC, MHD, and AKVD statistics for all the test data sets. Moreover, the accuracy of the proposed segmentation technique was compared against three other methods: the level-sets approach by Chan and Vese [2] (CV), the level-sets guided by image intensity only, and the level-sets guided by combined intensity and spatial features

TABLE 1: Segmentation accuracy of the proposed segmentation method using DSC, MHD(mm), and AKVD(%). All metrics are represented as minimum (Min), maximum (Max), and mean± standard deviation (SD).

	Evaluation Metrics		
	DSC	MHD (mm)	AVKD (%)
Min	0.85	4.00	8.00
Max	0.96	20.00	25.00
mean±SD	0.92 ± 0.02	6.20 ± 2.00	15.00 ± 3.00

TABLE 2: Segmentation accuracy of the proposed segmentation technique against three other level-sets methods using DSC, MHD(mm), and AKVD(%). All metrics are represented as mean± standard deviation (SD).

	Evaluation Metrics					
	DSC		MHD		AVKD	
	Mean±SD	<i>P</i> -value	Mean±SD	<i>P</i> -value	Mean±SD	<i>P</i> -value
Proposed	0.92±0.02%	—	6.20±2.00	—	15.00±3.00%	—
CV [2]	0.69±0.11%	< 0.0001	75.97±11.96	< 0.0001	46.05±13.18%	< 0.0001
I Only	0.54±0.07%	< 0.0001	29.14±5.34	< 0.0001	62.33±7.12%	< 0.0001
I+S	0.63±0.05%	< 0.0001	22.79±7.36	< 0.0001	53.82±5.35%	< 0.0001

using the same aforementioned segmentation evaluation metrics. Table 2 shows that the advantage of the developed segmentation approach is statistically significant with respect to the other methods, evidenced by the *P*-values less than 0.05, which confirms the high accuracy of the proposed segmentation techniques.

Figure 17 shows 3D results of the proposed segmentation method for three subjects along with their evaluation metrics. In particular, the developed segmentation technique proved its ability to precisely segment the kidney at higher b_i values.

Figure 18 shows more coronal cross-sectional segmentation results for three different subjects at b_0 and higher b_i values (b_{500} and b_{1000}) which in turn emphasize the high

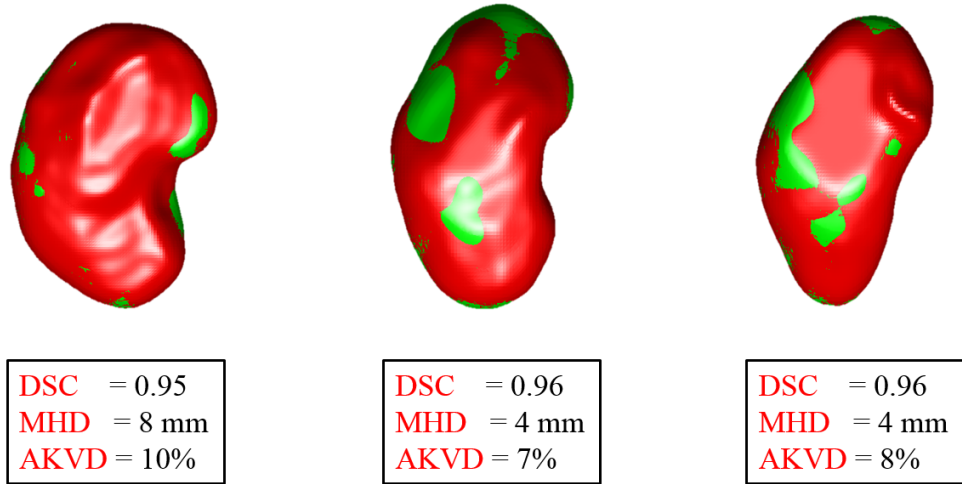


FIGURE 17: The proposed 3D segmentation (red) with respect to the expert’s manual ground truth (green) for three subjects with the associated DSC, MHD, and AKVD accuracy scores.

accuracy and robustness to noise of the proposed kidney segmentation technique.

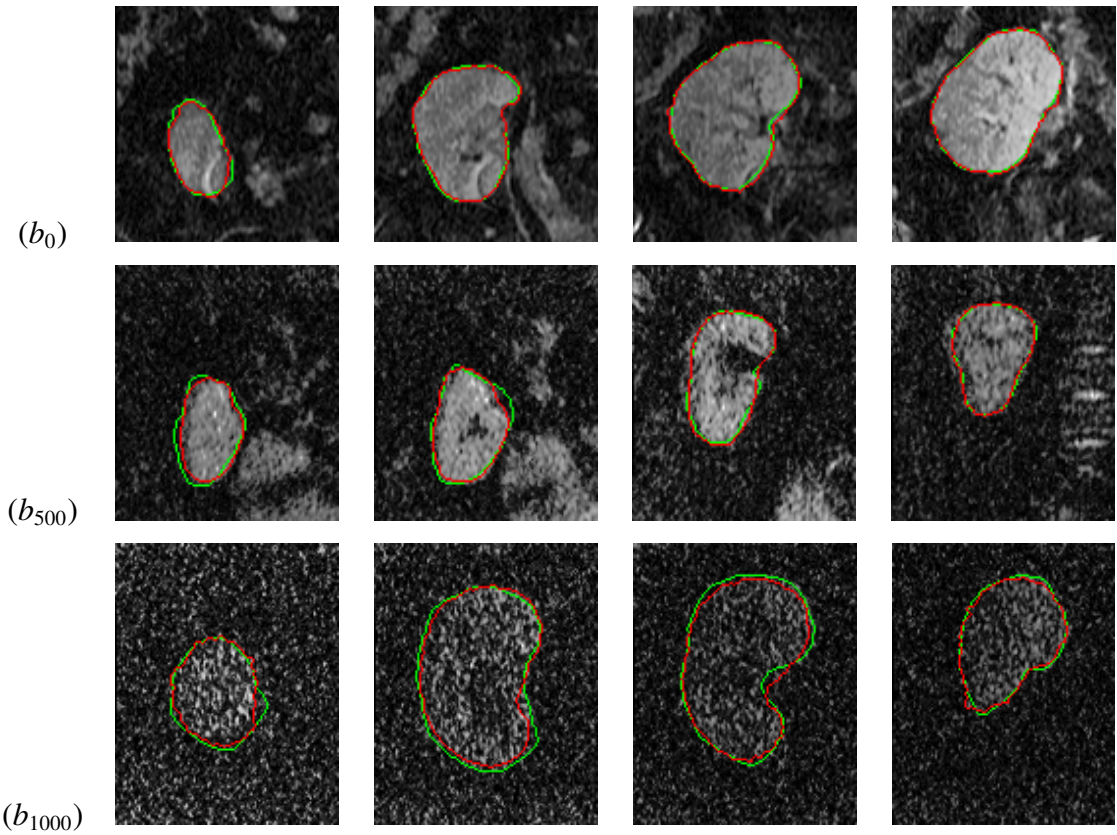


FIGURE 18: Four more coronal cross-sections (columns) for the proposed kidney segmentation from DW-MRI acquired at different b -values s/mm^2 .

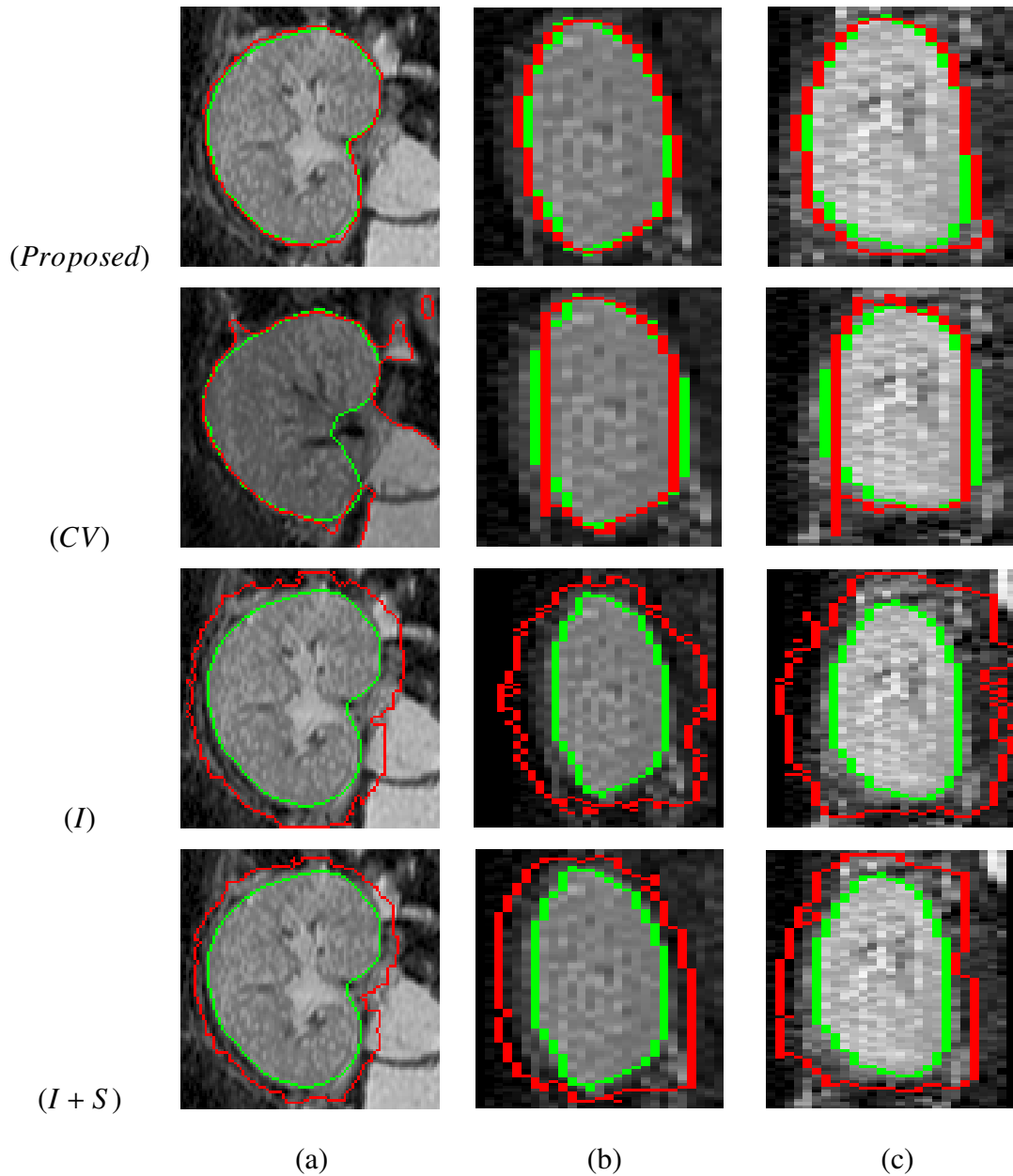


FIGURE 19: Comparative cross-sectional segmentation results for our approach, the traditional CV [2] level-set, the level-set guided by intensity alone, and intensity and spatial, respectively, in rows for three different types of cross sections (coronal cross section in the first column, axial cross section in the second column, and sagittal cross section in the third column) for one subject at b_0 s/mm². The model segmentation is shown in red with respect to the manual ground truth (green) from an expert.

The comparative accuracy of the proposed approach versus the CV method on representative data at different types of kidney cross sections (i.e., axial, sagittal, and coronal)

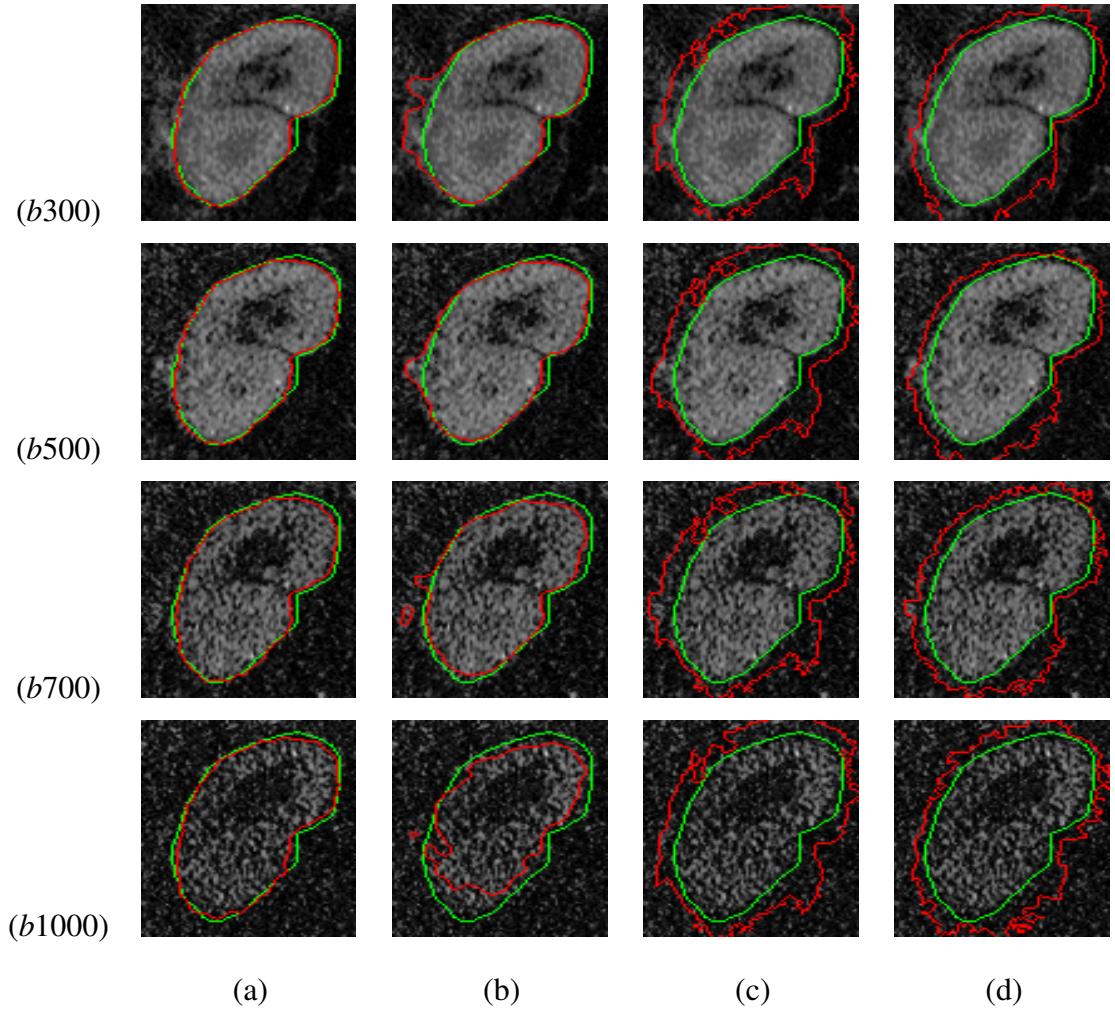


FIGURE 20: A sample coronal cross-sectional kidney segmentation for DW-MRI data acquired at b_{300} s/mm² (first row), b_{500} s/mm² (second row), b_{700} s/mm² (third row), and b_{1000} s/mm² (fourth row) for (a) the proposed approach; (b) the CV [2] approach; (c) the level-set guided by intensity only; and (d) intensity and spatial.

for one selected subject acquired at b_0 is shown in Figure 19.

In order to assess the renal function using DW-MRI-based CAD systems, which in turn has gained increased attention in recent years [178], the estimation of diffusion parameters (e.g., ADC) requires the accurate segmentation of the kidney on DW-MRI data acquired at both higher and lower b-values. However, the accurate segmentation of kidney volumes at higher b-values is a challenge compared with those at lower b-values because of the decreased contrast between the object and the background. In spite of the aforementioned challenge, the proposed segmentation technique extracts accurately the kidney from

diffusion data at higher b -values compared to the other three aforementioned methods as shown in Figure 20. In contrast to the existing DW-MRI approaches, the integration of the 3D appearance, shape, and spatial features increases the robustness of the proposed approach to overcome large image noise at higher b -values. Figure 20 demonstrates a sample coronal cross section segmentation for four subjects at b -values of 300, 500, 700 and 1000 s/mm^2 for the developed approach and the three other approaches used before. As shown in this figure, the proposed approach produces precise segmentation of the kidney at higher b -values compared with the other methods with respect to the ground truth segmentation.

3. Diagnostics Results

Following kidney segmentation, the developed CAD system classifies the transplant status with the SNCAE-based classifier and CDFs as discriminatory features. A leave-one-subject-out classification scenario applied to distinguish between the rejection and non-rejection cases from the CDFs of the ADCs for different b -values has correctly classified 98% of the cases, namely, 36 out of the 37 rejected and 16 out of the 16 non-rejected kidney transplants.

It is worth mentioning that fusing all the CDFs of the ADCs calculated at the 11 different b -values, totally improves the final diagnostic accuracy, as shown in Table 3, and helps to overcome the challenge of possible artifacts due to chemical shifts, which could occur at one or two b -values, if the artifacts exist.

TABLE 3: Diagnostic accuracy based on the input CDF of the ADC for individual b -values and the fused CDFs of all b -values.

Classification Accuracy											
b_{50}	b_{100}	b_{200}	b_{300}	b_{400}	b_{500}	b_{600}	b_{700}	b_{800}	b_{900}	b_{1000}	Fused b -values
75%	85%	75%	81%	70%	77%	62%	60%	64%	62%	74%	98%

In order to evaluate the effect of the CDFs encoding step (Δ) on the overall accuracy, the CDFs of the 3D ADCs were constructed using two different Δ_i ($\Delta = 0.02$ and 0.04).

Then, the SNCAE classifier was applied on the constructed CDFs and the results are shown in Table 4. As demonstrated in Table 4, the overall accuracy, sensitivity, and specificity, have been greatly reduced. This can be explained in part by the fact that increasing the value of Δ results in losing important data information, thus making the data not well-presented, which in turn affects the classifier performance.

TABLE 4: Diagnostic accuracy, sensitivity, and specificity for the developed CAD system with the SNCAE classifier using different CDF encoding steps (Δ_i).

Δ_i :	Quality of classification		
	Accuracy	Sensitivity	Specificity
$\Delta_1 = 0.01$	98%	97%	100%
$\Delta_2 = 0.02$	85%	86%	81%
$\Delta_3 = 0.04$	83%	84%	81%

Furthermore, the effect of changing the SNCAE structure on the overall accuracy has been investigated by using different SNCAE layouts (different number of hidden layers (l) and hidden nodes at each layer (s_l)). From the results in Table 5, the network structure with two hidden layers $s_1 = 50$ and $s_2 = 5$, demonstrated the highest accuracy.

TABLE 5: Diagnostic accuracy, sensitivity, and specificity for the developed CAD system with the SNCAE classifier using different structures, i.e., different number of hidden layers (l) and hidden nodes at each layer (s_l), using the same input size of 1100 (11 CDFs each of 100 region), $\alpha = 3 * 10^{-5}$, $\beta = 3$, and $\gamma = 0.1$.

SNCAE Structure:	Quality of classification		
	Accuracy	Sensitivity	Specificity
$s_1 = 5$	85%	84%	88%
$s_1 = 25$	60%	68%	44%
$s_1 = 50$	68%	70%	63%
$s_1 = 50$ and $s_2 = 5$	98%	97%	100%
$s_1 = 50$, $s_2 = 25$, and $s_3 = 5$	77%	92%	44%

In addition to the leave-one-subject-out approach, a four-fold cross-validation test has been performed where 75% of the data was used for training and the other 25% for testing, to further validate and justify the performance of the SNCAE classifier. As documented in Table 6, the diagnostic accuracy of the combined SNCAE classification system is almost independent of the choice of the training and testing data sets. The four-fold cross-validation experiment demonstrated an average accuracy of 96%.

TABLE 6: Sensitivity to a training set based on a four-fold cross-validation scenario.

	Cross-validating SNCAE classifier			
Testing group (25%)	1	2	3	4
Correct/All	12/13	12/13	13/13	14/14
Accuracy	92%	92%	100%	100%
Average Accuracy	96%			

To evaluate capabilities of the SNCAE classifier, it has been compared with seven well-known learnable classifiers from the Weka collection [1]: K*, IBK, Naive Bayes tree (NBT), Multi-class classifier (MCC), Decorate, Random tree (RT), and Random forest (RF). Table 7 presents their and the presented diagnostic accuracy in terms of the numbers of correctly classified rejection and non-rejection cases with respect to the overall numbers of subjects, sensitivity, and specificity. The SNCAE classifier demonstrated the best total diagnostic accuracy of 98% with 100 % specificity, or 16 correctly classified non-rejected transplants out of the 16 subjects, and 97% sensitivity, or 36 correctly classified rejected transplants out of the 37 subjects.

In addition, the receiver operating characteristics (ROC) (see Appendix .A) for the developed CAD system with SNCAE and the chosen seven Weka classifiers in Figure 21 have been constructed to test the performance. As shown in Figure 21, the area under the curve (AUC) is the highest for the SNCAE classifier and approaches the top-most unit value (see Table 7). These initial diagnostic results confirm that the proposed CAD system holds promise as a reliable non-invasive diagnostic tool.

Together with the automated classification, the proposed CAD system also provides

TABLE 7: Diagnostic accuracy in terms of correctly classified vs. true non-rejection (NR) and rejection (R) cases, sensitivity, specificity, and AUC for the proposed CAD system with the SNCAE classifier and seven classifiers from the Weka collection [1].

	Classification Accuracy					
	NR	R	Accuracy	Sensitivity	Specificity	AUC
K*	12/16	30/37	79%	81%	75%	0.82
IBK	15/16	36/37	96%	97%	94%	0.96
NBT	11/16	30/37	77%	81%	69%	0.79
MCC	15/16	34/37	92%	92%	94%	0.94
Decorate	8/16	34/37	79%	92%	50%	0.80
RT	10/16	29/37	74%	78%	63%	0.74
RF	9/16	35/37	83%	95%	56%	0.82
SNCAE	16/16	36/37	98%	97%	100%	0.97

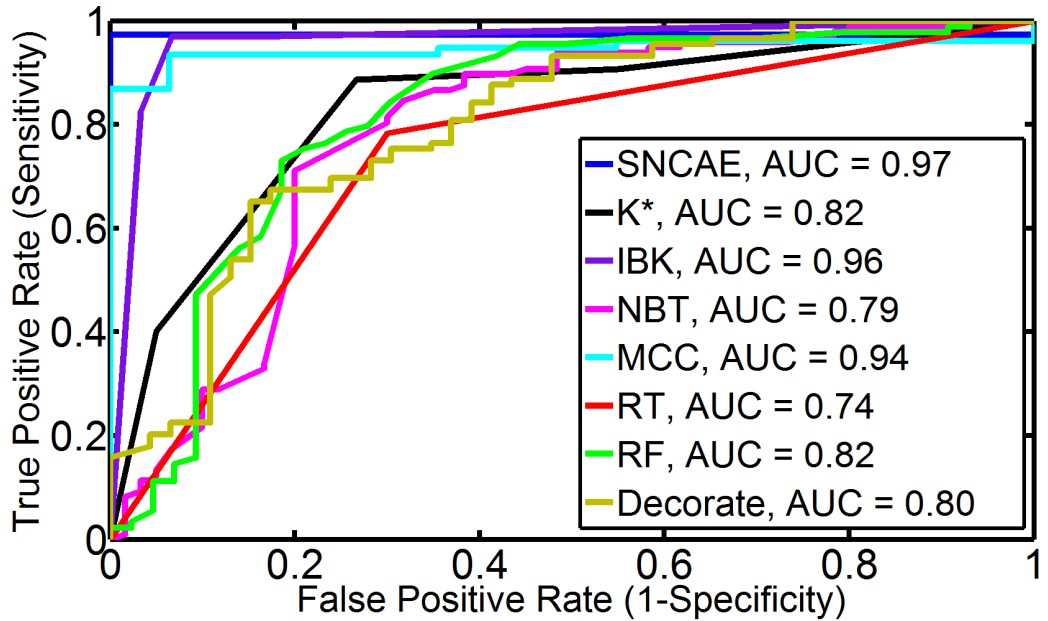


FIGURE 21: ROC curves and their AUC for SNCAE and Weka classifiers [1].

voxel-wise parametric ADC maps, which can help in local visual assessment of the transplanted kidney. The color-coded ADC map, which depicts the estimated voxel-wise ADCs of Equation (3), is more informative than the ADC CDFs collected over the entire kidney

and thus hides local peculiarities of spatial behavior of the ADCs. Examples of the ADC maps for two non-rejection and two acute rejection cases for the DW-MRI at the different b -values in Figure 22 demonstrate some expected relations between the local ADCs, which could be helpful for assessing the transplant and detecting its non-rejection or rejection status.

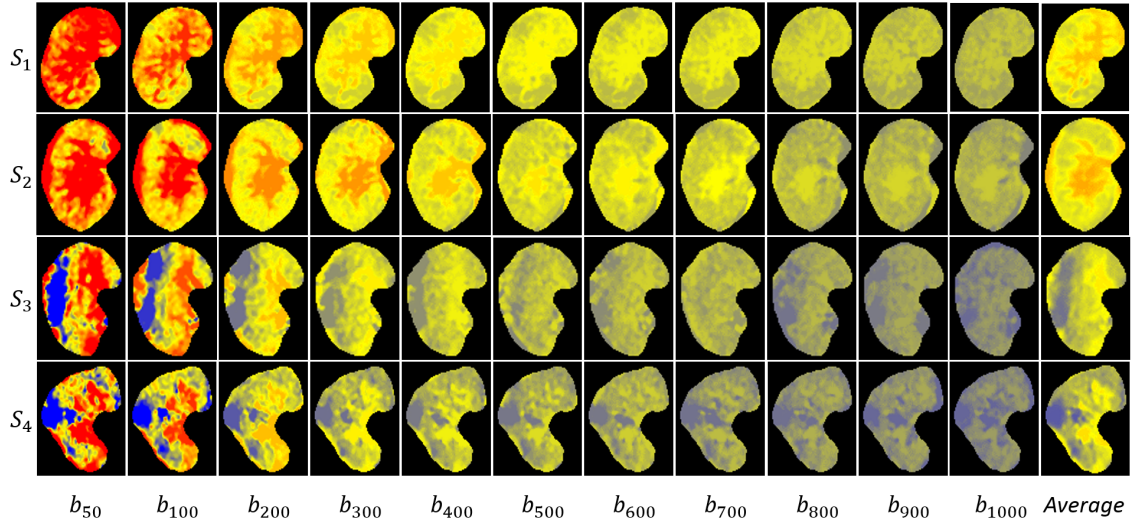


FIGURE 22: Pixel-wise parametric maps for DW-MRI at different b -values (b_{50} to b_{1000}) s/mm^2 and their average value for two non-rejection (S_1, S_2) and two rejection (S_3, S_4) subjects.

D. Chapter Summary

The developed CAD system for early detection of renal transplant rejection from 4D DW-MRI data combines existing and new techniques for non-rigid image alignment, kidney segmentation with a deformable boundary, estimation of spatial diffusion parameters (ADCs), and an SNCAE classification of the transplanted kidney status using CDFs of the ADCs as integral status descriptions. In a test on a biopsy-proven cohort of 53 participants, the developed system showed an overall accuracy of 98% in detecting rejected and non-rejected kidney transplants. These experimental results make the proposed non-invasive framework a reliable early renal diagnostic tool. In the future, the test sets of both non-

rejection and rejection kidney transplants will be increased in order to further validate the accuracy and robustness of the proposed framework in both segmentation of the DW-MRI and diagnosis. Also, new kidney transplant data sets, which are acquired at lower b -values, will be used to explore the ability of the proposed framework to determine the type of kidney transplant rejection, such as anti-body mediated rejection, T-cell or cellular rejection, or other causes of acute kidney dysfunction such as drug toxicity and viral infection.

CHAPTER III CONCLUSIONS AND FUTURE WORK

This thesis has presented a novel computer-aided diagnostic (CAD) system coupled with diffusion-weighted magnetic resonance imaging (DW-MRI) for the early detection of acute renal rejection after transplantation. Fortunately, the presented work in this thesis confirms the power of DW-MRI as an emerging imaging modality, with great thanks to its ability to provide both anatomical and functional information about both original and transplanted kidneys without exposing patients to any radiation, and with no need for contrast agents administration like the DCE-MRI. Therefore, a fully automated CAD system for early detection of acute renal transplant rejection was coupled with DW-MRI utilizing the aforementioned merits of DW-MRI. The developed CAD system for early detection of renal transplant rejection from 4D DW-MRI data combines existing and new techniques for non-rigid image alignment, kidney segmentation with a deformable boundary, estimation of functional diffusion parameters, called apparent diffusion coefficients (ADCs), and a stacked nonnegativity constrained autoencoder (SNCAE) classification of the transplanted kidney status using cumulative distribution functions (CDFs) of the ADCs as integral status descriptions.

A. Summary of Contributions

The main findings and contributions of this thesis can be summarized as follows:

- A new fully-automated computer-aided diagnostic (CAD) system using 4D (3D + b -value) diffusion-weighted magnetic resonance imaging (DW-MRI) for early determination of the transplanted kidney status as nonrejection or rejection.
- Fusion of the apparent diffusion coefficients (ADCs) at multiple low and high gra-

dient field strengths and duration (b -values) estimated from the segmented kidneys (subjects) using the proposed segmentation approach. The segmentation is done after a non-rigid image alignment for all subjects to a single reference subject.

- Exploring new discriminatory features to distinguish between nonrejected and rejected kidney transplants. These features are based on constructing cumulative distribution functions (CDFs) from the estimated ADCs at different b -values from b_0 to b_{1000} s/mm^2 for all segmented kidneys. It is worth mentioning that, the use of those CDFs instead of the voxel-wise ADCs of the entire kidney volume helps in making the data well-presented and mainly solves three important challenges of different kidney volumes: (i) loss of important information by data truncation for large kidney volumes; (ii) addition of nonexisting information by zero padding for small kidney volumes; and (iii) considerable time expenditures for training and classification for large kidney volumes.
- The use of stacked autoencoders with nonnegativity constraint (SNCAE) classifier for the purpose of discriminating nonrejected from rejected transplanted kidneys. After fusing all the constructed CDFs at different b -values for each subject, the SNCAE is trained and tested with these fused CDFs for all subjects by using a leave-one-subject-out approach and a four-fold cross-validation scenario as well.

B. Future Avenues

Several future trends that can be deeply investigated include but are not limited to the following avenues:

- Exploiting a new segmentation technique using a nonnegative matrix factorization (NMF)-guided active contour model to enhance and improve the segmentation accuracy. Some initial promising segmentation results have been obtained [179]
- After differentiating rejection from nonrejection kidney transplants, the next step is to obtain new DW-MRI data volumes at lower b -values and to investigate in-depth

the ability of the proposed CAD system to differentiate between different types of rejection (e.g., T-cell mediated rejection, anti-body mediated rejection, immunosuppressive toxicity, and viral infection) as it is a very important step for therapeutic purposes and for the determination of the appropriate treatment. Preliminary results for differentiating between different types of rejection are preferably found in [180]

- A new trend to be investigated is considering the fusion of multiple discriminating features extracted from images (e.g., CDFs of ADCs) with clinical data such as creatinine clearance (CrCl) and serum plasma creatinine (SPCR) to enhance and support the classification process with the clinical data as well, which in turn can provide a meaningful coupling of information provided by imaging and clinical information. Please see [181] for some initial results.
- Constructing a new two-cascaded stages CAD system utilizing the fusion of image-based with clinical-based biomarkers with the ability to differentiate nonrejection kidney transplants from transplanted kidneys with abnormalities (graft dysfunction) in the first stage. Then, classifying these abnormal kidneys as kidneys with early rejection and kidneys with other diseases (e.g., tubular inflammation, acute tubular injury, graft amyloidosis, etc.). Preliminary results of the suggested idea can be found in [181].
- Conducting a new study to investigate the ability of the proposed segmentation approach to extract the prostate from the surrounding tissues using DCE-MRI and DW-MRI [182–195].
- Extending the developed segmentation approach to segment the heart left/right ventricle wall by using contrast enhanced cardiac magnetic resonance images [196–218].
- Exploring the ability of the proposed CAD system to detect other organ diseases like lung cancer using contrast enhanced computed tomography (CECT) images [219–267].

- Investigating the capability of the developed CAD system to detect brain disorders and abnormalities (e.g., dyslexia, autism, etc.) [159, 268–311].

REFERENCES

- [1] M. Hall, E. Frank, G. Holmes, B. Pfahringer, P. Reutemann, and I. Witten. The WEKA data mining software: An update. *ACM SIGKDD Explorations Newsletter*, 11(1):10–18, 2009.
- [2] T. Chan and L. Vese. Active contours without edges. *IEEE Transactions on Image Processing*, 10(2):266–277, 2001.
- [3] A. Kukla, M. Adulla, J. Pascual, M. Samaniego, L. Nanovic, B. N. Becker, and A. Djamali. Ckd stage-to-stage progression in native and transplant kidney disease. *Nephrology Dialysis Transplantation*, 23(2):693–700, 2008.
- [4] N. K. Foundation. About chronic kidney disease [online]. Available, <http://www.kidney.org/kidneydisease/aboutckd>.
- [5] N. K. Foundation. Organ-donation-and-transplantation-stats [online]. Available, <http://www.kidney.org/news/newsroom/factsheets/organ-donation-and-transplantation-stats>.
- [6] G. Myers, G. Miller, J. Coresh, J. Fleming, N. Greenberg, T. Greene, T. Hostetter, A. Levey, M. Panteghini, M. Welch, et al. Recommendations for improving serum creatinine measurement: A report from the laboratory working group of the national kidney disease education program. *Clinical Chemistry*, 52(1):5–18, 2006.
- [7] E. Hollis, M. Shehata, F. Khalifa, M. Abou El-Ghar, T. Eldiasty, G. Gimel'farb, and A. El-Baz. Towards non-invasive diagnostic techniques for early detection of acute renal rejection: A review. *The Egyptian Journal of Radiology and Nuclear Medicine*, page To be submitted, 2016.
- [8] E. Widmaier, H. Raff, and K. Strang. *Vanders human physiology: The mechanisms of human body function*. 2006.
- [9] M. Mostapha, F. Khalifa, A. Alansary, A. Soliman, J. Suri, and A. El-Baz. Computer-aided diagnosis systems for acute renal transplant rejection: Challenges and methodologies. In *Abdomen and Thoracic Imaging*, pages 1–35. Springer, 2014.
- [10] G. Tortora and N. Anagnostakos. Maintenance of the human body. *Principles of Anatomy and Physiology*. New York, NY: Harper and Row, pages 441–695, 1981.
- [11] N. C. for Health Statistics (US et al. Health, United States, 2015: With special feature on racial and ethnic health disparities. 2016.
- [12] J. Stanifer, E. Turner, J. Egger, N. Thielman, F. Karia, V. Maro, K. Kilonzo, U. Patel, and K. Yeates. Knowledge, attitudes, and practices associated with chronic kidney disease in northern tanzania: A community-based study. *PloS one*, 11(6):e0156336, 2016.

- [13] S. Mendoza. Nephrotoxic drugs. *Pediatric Nephrology*, 2(4):466–476, 1988.
- [14] G. Obrador and B. Pereira. Screening for chronic kidney disease. *UpToDate: Waltham, MA*, 2015.
- [15] M. E. Institute. Life options: 10 symptoms of kidney disease [online]. Available, <http://lifeoptions.org/kidneyinfo/ckdinfo.php?page=3>.
- [16] M. Papadakis, S. McPhee, and M. Rabow. *Current medical diagnosis & treatment 2014*. McGraw Hill Medical, New York, USA, 2014.
- [17] S. Textor and L. Mailloux. Clinical manifestations and diagnosis of chronic kidney disease resulting from atherosclerotic renal artery stenosis. *UpToDate: [Online]. Available.*, 2016.
- [18] S. Davison. Management of chronic pain in chronic kidney disease. *UpToDate: [Online]. Available.*, 2015.
- [19] N. I. of Diabetes, Digestive, and K. Diseases. Dialysis [online]. Available, <http://www.niddk.nih.gov/health-information/health-communication-programs/nkdep/learn/living/kidney-failure/dialysis/pages/dialysis.aspx>.
- [20] M. Desai and I. Gill. Laparoscopic surgery in renal transplant recipients. *Urologic Clinics of North America*, 28(4):759–767, 2001.
- [21] R. Minter and G. Doherty. *Current Procedures Surgery*. McGraw-Hill Education, 2010.
- [22] G. Doherty. *Current diagnosis & treatment*. McGraw-Hill Education, 2015.
- [23] F. Gruessner. *Schwartz's Principles of Surgery. Edited by F. Brunicaudi*. McGraw Hill Medical, New York, USA, 2014.
- [24] U. T. Living. The national waiting list [online]. Available, <http://www.transplantliving.org/before-the-transplant/getting-on-the-list/the-national-waiting-list/>.
- [25] N. K. Foundation. NKF: Care after kidney transplant [online]. Available, <https://www.kidney.org/atoz/content/immunosuppression>.
- [26] H. R. Foundation. Clinic and follow-up visits after kidney transplantation [online]. Available, <http://www.seattlechildrens.org/clinics-programs/transplant/kidney/clinic-followup-visits-after-kidney-transplantation/>.
- [27] B. L. Kasiske, M. G. Zeier, J. R. Chapman, J. C. Craig, H. Ekberg, C. A. Garvey, M. D. Green, V. Jha, M. A. Josephson, B. A. Kiberd, et al. Kdigo clinical practice guideline for the care of kidney transplant recipients: a summary. *Kidney international*, 77(4):299–311, 2010.
- [28] E. Streeter, D. Little, D. Cranston, and P. Morris. The urological complications of renal transplantation: a series of 1535 patients. *BJU international*, 90(7):627–634, 2002.

- [29] S. Akbar, Z. Jafri, M. Amendola, B. Madrazo, R. Salem, and K. Bis. Complications of renal transplantation 1. *Radiographics*, 25(5):1335–1356, 2005.
- [30] S. B. Park, J. K. Kim, and K.-S. Cho. Complications of renal transplantation ultrasonographic evaluation. *Journal of Ultrasound in Medicine*, 26(5):615–633, 2007.
- [31] H. Richard III. Perirenal transplant fluid collections. In *Seminars in interventional radiology*, volume 21, page 235. Thieme Medical Publishers, 2004.
- [32] J. Lutz and U. Heemann. Tumours after kidney transplantation. *Current Opinion in Urology*, 13(2):105–109, 2003.
- [33] G. Wong and J. Chapman. Cancers after renal transplantation. *Transplantation Reviews*, 22(2):141–149, 2008.
- [34] E. Ramos and C. Tisher. Recurrent diseases in the kidney transplant. *American Journal of Kidney Diseases*, 24(1):142–154, 1994.
- [35] K. D. I. G. O. K. T. W. Group et al. KDIGO clinical practice guideline for the care of kidney transplant recipients. *American Journal of Transplantation: Official Journal of the American Society of Transplantation and the American Society of Transplant Surgeons*, 9:S33–S37, 2009.
- [36] V. F. Muglia, S. R. Teixeira, E. A. Roma o, M. F. Cassini, M. F. de Andrade, M. Kato, M. E. P. Nardin, and S. T. Jr. *Imaging in Kidney Transplantation in Current Issues and Future Direction in Kidney Transplantation*, T. Rath, Editor. InTech, 2013.
- [37] F. R. collins A. et al. United States renal data system 2011 annual data report: Atlas of chronic kidneydisease & end-stage renal disease in the United States. *American Journal of Kidney Diseases*, 59(1Suppl1):A7, 2012.
- [38] A. Abbas, A. Lichtman, and S. Pillai. *Cellular and molecular immunology*. Elsevier Health Sciences, 2014.
- [39] S. Flechner. Renal transplantation. In J. McAninch and F. Lue, editors, *Smith and Tanagho's General Urology*. McGraw Hill Professional, New York, USA, 2012.
- [40] D. Brennan and E. Ramos. Management of bk virus-induced (polyomavirus-induced) nephropathy in kidney transplantation. *UpToDate: [Online] Available*. Waltham, MA, 2015.
- [41] R. Montgomery, A. Zachary, L. Racusen, M. Leffell, K. King, J. Burdick, W. Maley, and L. Ratner. Plasmapheresis and intravenous immune globulin provides effective rescue therapy for refractory humoral rejection and allows kidneys to be successfully transplanted into cross-match-positive recipients. *Transplantation*, 70(6):887–895, 2000.
- [42] M. Pascual, S. Saidman, N. Tolkoff-Rubin, W. Williams, S. Mauiyyedi, J. M. Duan, M. L. Farrell, R. Colvin, B. Cosimi, and F. Delmonico. Plasma exchange and tacrolimus-mycophenolate rescue for acute humoral rejection in kidney transplantation1. *Transplantation*, 66(11):1460–1464, 1998.

- [43] B. D. Chon, James. Acute renal allograft rejection: Treatment. *UpToDate: [Online] Available. Waltham, MA, 2014.*
- [44] M. Jordan, R. Shapiro, V. Vivas, Carlosand Scantlebury, P. Rhandhawa, G. Carri-
eri, J. McCauley, A. Demetris, A. Tzakis, J. Fung, et al. Fk506 rescue for resistant
rejection of renal allografts under primary cyclosporine immunosuppression. *Trans-
plantation*, 57(6):860–865, 1994.
- [45] M. Jordan, R. Naraghi, R. Shapiro, D. Smith, C. Vivas, V. Scantlebury, A. Gritsch,
J. McCauley, P. Randhawa, A. Demetris, et al. Tacrolimus rescue therapy for renal
allograft rejection–five-year experience. *Transplantation*, 63(2):223–228, 1997.
- [46] E. Burdmann, T. Andoh, L. Yu, and W. Bennett. Cyclosporine nephrotoxicity. In
Seminars in Nephrology, volume 23, pages 465–476. Elsevier, 2003.
- [47] W. Bennett. Cyclosporine and tacrolimus nephrotoxicity. *UpToDate: [Online] Available. Waltham, MA, 2015.*
- [48] A. de Mattos, A. Olyaei, and W. Bennett. Nephrotoxicity of immunosuppressive
drugs: long-term consequences and challenges for the future. *American Journal of
Kidney Diseases*, 35(2):333–346, 2000.
- [49] B. Weikert and E. Blumberg. Viral infection after renal transplantation: surveil-
lance and management. *Clinical Journal of the American Society of Nephrology*,
3(Supplement 2):S76–S86, 2008.
- [50] M. Ursula Brewster and M. M. Perazella. *Chronic Kidney Disease and Dialysis in
Principles and Practice of Hospital Medicine. Edited by S.C. McKean and Others.*
McGraw Hill Professional, New York, USA, 2012.
- [51] N. I. of Diabetes, Digestive, and K. Diseases. Esti-
mating glomerular filtration rate (gfr) [online]. Available,
[http://www.niddk.nih.gov/health-information/health-communication-
programs/nkdep/lab-evaluation/gfr/estimating/pages/estimating.aspx](http://www.niddk.nih.gov/health-information/health-communication-programs/nkdep/lab-evaluation/gfr/estimating/pages/estimating.aspx).
- [52] D. Pagana and T. Pagana. *Mosby's diagnostic and laboratory test reference.* Elsevier
Health Sciences, 2012.
- [53] P. Medicine. Blood smear [online]. Available, [https://www.pennmedicine.org/for-
patients-and-visitors/patient-information/conditions-treated-a-to-z?gclid=003665](https://www.pennmedicine.org/for-patients-and-visitors/patient-information/conditions-treated-a-to-z?gclid=003665).
- [54] D. Longo, J. Adamson, A. Fauci, D. Kasper, S. Hauser, J. Jameson, and J. Loscalzo.
*Anemia and Polycythemia In: Harrison's principles of Internal medicine. Edited by
15th, vol. A2.* New York: McGraw-Hill, 2001.
- [55] A. Fogo and N. E. *Atlas of Urinary Sediments and Renal Biopsies in Harrison's
Principles of Internal Medicine. Edited by D. Kasper and Others.* McGraw Hill
Professional, New York, USA, 2015.
- [56] V. Jha. Post-transplant infections: An ounce of prevention. *Indian Journal of
Nephrology*, 20(4):171–178, 2010.

- [57] M. C. Staff. Test and procedures: Kidney biopsy: Results [online]. Available, <http://www.mayoclinic.org/tests-procedures/kidney-biopsy/basics/results/prc-20018979>.
- [58] D. Chesney, B. Brouhard, and R. Cunningham. Safety and cost effectiveness of pediatric percutaneous renal biopsy. *Pediatric Nephrology*, 10(4):439–445, 1996.
- [59] E. Brown, M. Chen, N. Wolfman, D. Ott, and N. Watson. Complications of renal transplantation: Evaluation with US and radionuclide imaging. *Radiographics*, 20(3):607–622, 2000.
- [60] E. Giele. *Computer methods for semi-automatic MR renogram determination*. Technische Universiteit Eindhoven, 2002.
- [61] A. Taylor and J. Nally. Clinical applications of renal scintigraphy. *American Journal of Roentgenology*, 164(1):31–41, 1995.
- [62] J. Heaf and J. Iversen. Uses and limitations of renal scintigraphy in renal transplantation monitoring. *European Journal of Nuclear Medicine*, 27(7):871–879, 2000.
- [63] C. Sebastià, S. Quiroga, R. Boyé, C. Cantarell, M. Fernandez-Planas, and A. Alvarez. Helical CT in renal transplantation: Normal findings and early and late complications. *Radiographics*, 21(5):1103–1117, 2001.
- [64] A. Grabner, D. Kentrup, U. Schnöckel, M. Schäfers, and S. Reuter. Non-invasive diagnosis of acute renal allograft rejection- Special focus on gamma scintigraphy and positron emission tomography. In *Current Issues and Future Direction in Kidney Transplantation*, chapter 4. 2013.
- [65] J. Chudek, A. Kolonko, R. Krol, J. Ziaja, L. Cierpka, and A. Wicek. The intrarenal vascular resistance parameters measured by duplex Doppler ultrasound shortly after kidney transplantation in patients with immediate, slow, and delayed graft function. In *Transplantation Proceedings*, volume 38, pages 42–45, 2006.
- [66] A. Saracino, G. Santarsia, A. Latorraca, and V. Gaudio. Early assessment of renal resistance index after kidney transplant can help predict long-term renal function. *Nephrology Dialysis Transplantation*, 21(10):2916–2920, 2006.
- [67] R. Kramann, D. Frank, V. M. Brandenburg, N. Heussen, J. Takahama, T. Krüger, J. Riehl, and J. Floege. Prognostic impact of renal arterial resistance index upon renal allograft survival: The time point matters. *Nephrology Dialysis Transplantation*, 27(10):3958–3963, 2012.
- [68] K. Krejčí, J. Zdražil, T. Tichý, S. Al-Jabry, V. Horčíčka, P. Štrebl, and P. Bachleda. Sonographic findings in borderline changes and subclinical acute renal allograft rejection. *European Journal of Radiology*, 71(2):288–295, 2009.
- [69] M. Damasio, G. Cittadini, D. Rolla, F. Massarino, N. Stagnaro, M. Gherzi, E. Paoletti, and L. Derchi. Ultrasound findings in dual kidney transplantation. *La Radiologia Medica*, 118(1):14–22, 2013.

- [70] H. Shebel, A. Akl, A. Dawood, T. El-Diasty, A. Shokeir, M. Ghoneim, et al. Power doppler sonography in early renal transplantation: Does it differentiate acute graft rejection from acute tubular necrosis? *Saudi Journal of Kidney Diseases and Transplantation*, 25(4):733, 2014.
- [71] T. Fischer, S. Filimonow, J. Dieckhöfer, T. Slowinski, M. Mühler, A. Lembcke, K. Budde, H.-H. Neumayer, V. Ebeling, M. Giessing, A. Thomas, and S. Morgera. Improved diagnosis of early kidney allograft dysfunction by ultrasound with echo enhancerA new method for the diagnosis of renal perfusion. *Nephrology Dialysis Transplantation*, 21(10):2921–2929, 2006.
- [72] L. Benozzi, G. Cappelli, M. Granito, D. Davoli, D. Favali, M. Montecchi, A. Grossi, P. Torricelli, and A. Albertazzi. Contrast-enhanced sonography in early kidney graft dysfunction. In *Transplantation Proceedings*, volume 41, pages 1214–1215, 2009.
- [73] V. Schwenger, V. Hankel, J. Seckinger, S. Macher-Göppinger, C. Morath, M. Zeisbrich, M. Zeier, and L. Kihm. Contrast-enhanced ultrasonography in the early period after kidney transplantation predicts long-term allograft function. In *Transplantation proceedings*, volume 46, pages 3352–3357. Elsevier, 2014.
- [74] I. Göcze, P. Renner, B. M. Graf, H. J. Schlitt, T. Bein, and K. Pfister. Simplified approach for the assessment of kidney perfusion and acute kidney injury at the bedside using contrast-enhanced ultrasound. *Intensive Care Medicine*, 41(2):362–363, 2015.
- [75] Y. Jin, C. Yang, S. Wu, S. Zhou, Z. Ji, T. Zhu, and W. He. A novel simple noninvasive index to predict renal transplant acute rejection by contrast-enhanced ultrasonography. *Transplantation*, 99(3):636–641, 2015.
- [76] A. Kirkpantur, R. Yilmaz, D. E. Baydar, T. Aki, B. Cil, M. Arici, B. Altun, Y. Erdem, I. Erkan, M. Bakkaloglu, et al. Utility of the Doppler ultrasound parameter, resistive index, in renal transplant histopathology. In *Transplantation Proceedings*, volume 40, pages 104–106, 2008.
- [77] S. Seiler, S. M. Colbus, G. Lucisano, K. S. Rogacev, M. K. Gerhart, M. Ziegler, D. Fliser, and G. H. Heine. Ultrasound renal resistive index is not an organ-specific predictor of allograft outcome. *Nephrology Dialysis Transplantation*, 27(8):3315–3320, 2012.
- [78] R. Kramann, D. Frank, V. M. Brandenburg, N. Heussen, J. Takahama, T. Krüger, J. Riehl, and J. Floege. Prognostic impact of renal arterial resistance index upon renal allograft survival: The time point matters. *Nephrology Dialysis Transplantation*, 27(10):3958–3963, 2012.
- [79] D. O. Cosgrove and K. E. Chan. Renal transplants: What ultrasound can and cannot do. *Ultrasound Quarterly*, 24(2):77–87, 2008.
- [80] P. Mansfield. Snapshot magnetic resonance imaging (nobel lecture). *Angewandte Chemie International Edition*, 43(41):5456–5464, 2004.

- [81] J. de Priester, J. den Boer, M. H. Christiaans, A. G. Kessels, E. L. Giele, A. Hasman, H. van Hooff, and J. van Engelshoven. Automated quantitative evaluation of diseased and nondiseased renal transplants with MR renography. *Journal of Magnetic Resonance Imaging*, 17(1):95–103, 2003.
- [82] S. Yuksel, A. El-Baz, A. Farag, M. Abou El-Ghar, T. Eldiasty, and M. Ghoneim. Automatic detection of renal rejection after kidney transplantation. In *International Congress Series*, volume 1281, pages 773–778. Elsevier, 2005.
- [83] A. Farag, A. El-Baz, Yuksel, M. A. El-Ghar, and T. Eldiasty. A framework for the detection of acute rejection with Dynamic Contrast Enhanced Magnetic Resonance Imaging. In *Proceedings of IEEE Int. Symp. Biomed. Imaging: From Nano to Macro*, pages 418–421, Arlington, Virginia, USA, April 6-9, 2006.
- [84] A. El-Baz, A. Farag, R. Fahmi, S. Yuksel, M. A. El-Ghar, and T. Eldiasty. Image analysis of renal DCE MRI for the detection of acute renal rejection. In *Proceedings of IEEE International Conference on Pattern Recognition*, pages 822–825, Hong Kong, August 20-24, 2006.
- [85] A. El-Baz, A. Farag, R. Fahmi, S. Yuksel, W. Miller, M. A. El-Ghar, T. El-Diasty, and M. Ghoneim. A new CAD system for the evaluation of kidney diseases using DCE-MRI. In *Proceedings of Int. Conf. Med. Image Comput. Comput.-Assist. Interv.*, pages 446–453, Copenhagen, Denmark, October 1-6, 2006.
- [86] A. El-Baz, A. Farag, S. Yuksel, M. A. El-Ghar, T. Eldiasty, and M. Ghoneim. Application of deformable models for the detection of acute renal rejection. In A. A. Farag and J. S. Suri, editors, *Deformable Models*, volume 1, chapter 10, pages 293–333. 2007.
- [87] A. El-Baz, G. Gimel'farb, and M. A. El-Ghar. New motion correction models for automatic identification of renal transplant rejection. In *Proceedings of Int. Conf. Med. Image Comput. Comput.-Assist. Interv.*, pages 235–243, Brisbane, Australia, October 29–November 2, 2007.
- [88] A. El-Baz, G. Gimel'farb, and M. A. El-Ghar. A novel image analysis approach for accurate identification of acute renal rejection. In *Proceedings of IEEE Int. Conf. Image Process.*, pages 1812–1815, San Diego, California, USA, October 12–15, 2008.
- [89] A. El-Baz, G. Gimel'farb, and M. A. El-Ghar. Image analysis approach for identification of renal transplant rejection. In *Proceedings of IEEE International Conference on Pattern Recognition*, pages 1–4, Tampa, Florida, USA, December 8-11, 2008.
- [90] H. Rusinek, Y. Boykov, M. Kaur, S. Wong, L. Bokacheva, J. B. Sajaous, A. J. Huang, S. Heller, and V. S. Lee. Performance of an automated segmentation algorithm for 3D MR renography. *Magn. Reson. Med.*, 57(6):1159–1167, 2007.
- [91] D. Zikic, S. Sourbron, X. Feng, H. J. Michaely, A. Khamene, and N. Navab. Automatic alignment of renal DCE-MRI image series for improvement of quantitative

- tracer kinetic studies. In *Proceedings of SPIE, Medical Imaging: Image Processing*, volume 6914, pages 1–8. International Society for Optics and Photonics, 2008.
- [92] B. D. de Senneville, I. A. Mendichovszky, S. Roujol, I. Gordon, C. Moonen, and N. Grenier. Improvement of MRI-functional measurement with automatic movement correction in native and transplanted kidneys. *Journal of Magnetic Resonance Imaging*, 28(4):970–978, 2008.
- [93] M. Aslan, H. A. El Munim, A. Farag, and M. Abou El-Ghar. Assessment of kidney function using dynamic contrast enhanced mri techniques. *Biomedical Image Analysis and Machine Learning Technologies: Applications and Techniques: Applications and Techniques*, page 214, 2009.
- [94] A. Anderlik, A. Munthe-Kaas, O. Oye, E. Eikefjord, J. Rorvik, D. Ulvang, F. Zollner, and A. Lundervold. Quantitative assessment of kidney function using dynamic contrast enhanced MRI-Steps towards an integrated software prototype. In *Proceedings of the 6th International Symposium on Image and Signal Processing and Analysis (ISPA'09)*, pages 575–581, Salzburg, Austria, September 16–18, 2009.
- [95] S. Sourbron, H. Michaely, M. Reiser, and S. Schoenberg. MRI- measurement of perfusion and glomerular filtration in the human kidney with a separable compartment model. *IEEE Engineering in Medicine and Biology Magazine*, 43(1):40–48, 2008.
- [96] F. Zöllner, R. Sance, P. Rogelj, M. J. Ledesma-Carbayo, J. Rørvik, A. Santos, and A. Lundervold. Assessment of 3D DCE-MRI of the kidneys using non-rigid image registration and segmentation of voxel time courses. *Computerized Medical Imaging and Graphics*, 33(3):171–181, 2009.
- [97] J. MacQueen. Some methods for classification and analysis of multivariate observations. In *Proceedings of 5th Berkeley Symposium on Mathematical Statistics and Probability*, pages 281–297, University of California Press, 1967.
- [98] A. Wentland, E. Sadowski, A. Djamali, T. Grist, B. Becker, and S. Fain. Quantitative MR measures of intrarenal perfusion in the assessment of transplanted kidneys: initial experience. *Academic radiology*, 16(9):1077–1085, 2009.
- [99] M. Abou El-Ghar, A. Farag, T. El-Diasty, A. Shokeir, H. Refaie, Y. Osman, T. Mohsen, and M. Ghoneim. Computer aided detection of acute renal allograft dysfunction using dynamic contrast enhanced MRI. *The Egyptian Journal of Radiology and Nuclear Medicine*, 42(3):443–449, 2011.
- [100] A. Yamamoto, J. Zhang, H. Rusinek, H. Chandarana, P.-H. Vivier, J. Babb, T. Diflo, D. John, J. Benstein, L. Barisoni, et al. Quantitative evaluation of acute renal transplant dysfunction with low-dose three-dimensional MR renography. *Radiology*, 260(3):781–789, 2011.
- [101] E. Hodneland, A. Kjørstad, E. Andersen, J. Monssen, A. Lundervold, J. Rorvik, and A. Munthe-Kaas. In vivo estimation of glomerular filtration in the kidney using DCE-MRI. In *Proceedings of the 7th International Symposium on Image and Signal Processing Analysis (ISPA'11)*, pages 755–761, Dubrovnik, Croatia, September 4–6, 2011.

- [102] V. Positano, I. Bernardeschi, V. Zampa, M. Marinelli, L. Landini, and M. F. Santarelli. Automatic 2D registration of renal perfusion image sequences by mutual information and adaptive prediction. *Magnetic Resonance Materials in Physics, Biology and Medicine*, 26(3):1–11, 2013.
- [103] F. Khalifa, A. El-Baz, G. Gimel'farb, and M. A. El-Ghar. Non-invasive image-based approach for early detection of acute renal rejection. In *Proceedings of Int. Conf. Med. Image Comput. Comput.-Assist. Interv.*, pages 10–18, Beijing, China, September 20–24, 2010.
- [104] F. Khalifa, G. Beache, M. Abou El-Ghar, T. El-Diasty, G. Gimel'farb, M. Kong, and A. El-Baz. Dynamic contrast-enhanced MRI-based early detection of acute renal transplant rejection. *IEEE Transaction on Medical Imaging*, 32(10):1910–1927, 2013.
- [105] F. Khalifa, G. Beache, G. Gimel'farb, G. Giridharan, and A. El-Baz. Accurate automatic analysis of cardiac cine images. *Transaction on Biomedical Engineering*, 59(2):445–455, 2012.
- [106] F. Khalifa, G. Beache, M. Nitzken, G. Gimel'farb, G. Giridharan, and A. El-Baz. Automatic analysis of left ventricle wall thickness using short-axis cine CMR images. In *Proceedings of IEEE Int. Symp. Biomed. Imaging: From Nano to Macro*, pages 1306–1309, Chicago, Illinois, USA, 30 March–2 April, 2011.
- [107] E. Elbeltagi, T. Hegazy, and D. Grierson. Comparison among five evolutionary-based optimization algorithms. *Advanced Engineering Informatics*, 19(1):43–53, 2005.
- [108] F. Khalifa, M. Abou El-Ghar, B. Abdollahi, H. Frieboes, T. El-Diasty, and A. El-Baz. A comprehensive non-invasive framework for automated evaluation of acute renal transplant rejection using DCE-MRI. *NMR in Biomedicine*, 26(11):1460–1470, 2013.
- [109] E. Hodneland, Å. Kjørstad, E. Andersen, J. A. Monssen, A. Lundervold, J. Rorvik, and A. Munthe-Kaas. In vivo estimation of glomerular filtration in the kidney using DCE-MRI. In *Proceedings of 7th International Symposium on Image and Signal Processing and Analysis (ISPA'11)*, pages 755–761. IEEE, 2011.
- [110] G. Liu, F. Han, W. Xiao, Q. Wang, Y. Xu, and J. Chen. Detection of renal allograft rejection using blood oxygen level-dependent and diffusion weighted magnetic resonance imaging: A retrospective study. *BMC Nephrology*, 15(1):158, 2014.
- [111] A. Djamali, E. Sadowski, M. Samaniego-Picota, S. Fain, R. Muehrer, S. Alford, T. Grist, and B. Becker. Noninvasive assessment of early kidney allograft dysfunction by blood oxygen level-dependent magnetic resonance imaging. *Transplantation*, 82(5):621–628, 2006.
- [112] F. Han, W. Xiao, Y. Xu, J. Wu, Q. Wang, H. Wang, M. Zhang, and J. Chen. The significance of BOLD MRI in differentiation between renal transplant rejection and acute tubular necrosis. *Nephrology Dialysis Transplantation*, 23(8):2666–2672, 2008.

- [113] E. Sadowski, A. Djamali, A. Wentland, R. Muehrer, B. Becker, T. Grist, and S. Fain. Blood oxygen level-dependent and perfusion magnetic resonance imaging: Detecting differences in oxygen bioavailability and blood flow in transplanted kidneys. *Magnetic Resonance Imaging*, 28(1):56–64, 2010.
- [114] D. Yablonskiy and M. Haacke. Theory of nmr signal behavior in magnetically inhomogeneous tissues: the static dephasing regime. *Magnetic Resonance in Medicine*, 32(6):749–763, 1994.
- [115] H. Michaely, K. Herrmann, K. Nael, N. Oesingmann, M. Reiser, and S. Schoenberg. Functional renal imaging: Nonvascular renal disease. *Abdominal Imaging*, 32(1):1–16, 2007.
- [116] U. Eisenberger, H. Thoeny, T. Binsler, M. Gugger, F. Frey, C. Boesch, and P. Vermathen. Evaluation of renal allograft function early after transplantation with diffusion-weighted MR imaging. *European Radiology*, 20(6):1374–1383, 2010.
- [117] K. Hueper, A. A. Khalifa, J. H. Bräsen, V. Chieu, V. Dai, M. Gutberlet, S. Winterle, F. Lehner, N. Richter, M. Peperhove, et al. Diffusion-weighted imaging and diffusion tensor imaging detect delayed graft function and correlate with allograft fibrosis in patients early after kidney transplantation. *Journal of Magnetic Resonance Imaging*, 2016.
- [118] J. Xu, W. Xiao, L. Zhang, and M. Zhang. [value of diffusion-weighted MR imaging in diagnosis of acute rejection after renal transplantation]. *Journal of Zhejiang University. Medical Sciences*, 39(2):163–167, 2010.
- [119] S. Palmucci, L. Mauro, P. Veroux, G. Failla, P. Milone, G. Ettore, N. Sinagra, G. Giuffrida, D. Zerbo, and M. Veroux. Magnetic resonance with diffusion-weighted imaging in the evaluation of transplanted kidneys: Preliminary findings. In *Transplantation Proceedings*, volume 43, pages 960–966. Elsevier, 2011.
- [120] S. Palmucci, L. Mauro, G. Failla, P. Foti, P. Milone, N. Sinagra, D. Zerbo, P. Veroux, G. Ettore, and M. Veroux. Magnetic resonance with diffusion-weighted imaging in the evaluation of transplanted kidneys: Updating results in 35 patients. In *Transplantation Proceedings*, volume 44, pages 1884–1888. Elsevier, 2012.
- [121] P. Vermathen, T. Binsler, C. Boesch, U. Eisenberger, and H. C. Thoeny. Three-year follow-up of human transplanted kidneys by diffusion-weighted MRI and blood oxygenation level-dependent imaging. *Journal of Magnetic Resonance Imaging*, 35(5):1133–1138, 2012.
- [122] K. Wypych-Klunder, A. Adamowicz, A. Lemanowicz, W. Szczęsny, Z. Włodarczyk, and Z. Serafin. Diffusion-weighted MR imaging of transplanted kidneys: Preliminary report. *Polish Journal of Radiology*, 79:94–98, 2014.
- [123] J. M. Provenzale, S. Engelter, J. R. Petrella, J. S. Smith, and J. MacFall. Use of MR exponential diffusion-weighted images to eradicate T2 ‘shine-through’ effect. *American Journal of Roentgenology*, 172(2):537–539, 1999.

- [124] A. Kaul, R. Sharma, R. Gupta, H. Lal, A. Yadav, D. Bhadhuria, N. Prasad, A. Gupta, et al. Assessment of allograft function using diffusion-weighted magnetic resonance imaging in kidney transplant patients. *Saudi Journal of Kidney Diseases and Transplantation*, 25(6):1143, 2014.
- [125] M. Abou El-Ghar, T. El-Diasty, A. El-Assmy, H. Refaie, A. Refaie, and M. Ghoneim. Role of diffusion-weighted MRI in diagnosis of acute renal allograft dysfunction: A prospective preliminary study. *The British Journal of Radiology*, 85(1014):e206e211, 2014.
- [126] H. Thoeny, D. Zumstein, S. Simon-Zoula, U. Eisenberger, F. De Keyzer, L. Hofmann, P. Vock, C. Boesch, F. J. Frey, and P. Vermathen. Functional evaluation of transplanted kidneys with diffusion-weighted and BOLD MR imaging: Initial experience 1. *Radiology*, 241(3):812–821, 2006.
- [127] F. Khalifa, A. Soliman, G. Gimel'farb, R. Ouseph, A. Dwyer, T. El-Diasty, and A. El-Baz. Models and methods for analyzing DCE-MRI: A review. *Medical Physics*, 41(12):1–32, 2014.
- [128] R. Katzberg, M. Buonocore, M. Ivanovic, C. Pellot-Barakat, J. Ryan, K. Whang, J. Brock, and D. Jones. Functional, dynamic, and anatomic MR urography: Feasibility and preliminary findings. *Academic Radiology*, 8(11):1083–1099, 2001.
- [129] V. Lee, H. Rusinek, M. Noz, P. Lee, M. Raghavan, and E. Kramer. Dynamic three-dimensional MR renography for the measurement of single kidney function: Initial experience 1. *Radiology*, 227(1):289–294, 2003.
- [130] P.-T. Yap, Y. Zhang, and D. Shen. Brain tissue segmentation based on diffusion MRI using l0 sparse-group representation classification. In *Medical Image Computing and Computer-Assisted Intervention, (MICCAI'15)*, pages 132–139. Springer, 2015.
- [131] S. Mujumdar, R. Varma, and L. Kishore. A novel framework for segmentation of stroke lesions in diffusion weighted MRI using multiple b-value data. In *Proceedings of 21st International Conference on Pattern Recognition (ICPR'12)*, pages 3762–3765. IEEE, 2012.
- [132] M. Saad, S. Abu-Bakar, S. Muda, M. Mokji, and A. Abdullah. Fully automated region growing segmentation of brain lesion in diffusion-weighted MRI. *IAENG International Journal of Computer Science*, 39(2):155–164, 2012.
- [133] M. Saad, S. Abu-Bakar, S. Muda, and M. Mokji. Automated segmentation of brain lesion based on diffusion-weighted MRI using a split and merge approach. In *Proceedings of 2010 IEEE EMBS Conference on Biomedical Engineering and Sciences (IECBES)*, pages 475–480. IEEE, 2010.
- [134] N. M. Saad, S. Abu-Bakar, S. Muda, M. Mokji, and L. Salahuddin. Brain lesion segmentation of diffusion-weighted MRI using gray level co-occurrence matrix. In *Proceedings of 2011 IEEE International Conference on Imaging Systems and Techniques (IST)*, pages 284–289. IEEE, 2011.

- [135] M. Niethammer, C. Zach, J. Melonakos, and A. Tannenbaum. Near-tubular fiber bundle segmentation for diffusion weighted imaging: Segmentation through frame reorientation. *NeuroImage*, 45(1):S123–S132, 2009.
- [136] P. McClure, F. Khalifa, A. Soliman, M. Abou El-Ghar, G. Gimelfarb, A. Elmagraby, and A. El-Baz. A novel NMF guided level-set for DWI prostate segmentation. *Journal of Computer Science and System Biology*, 7(6):209–216, 2014.
- [137] A. Firjani, A. Elnakib, F. Khalifa, G. Gimelfarb, M. Abou El-Ghar, A. Elmaghraby, and A. El-Baz. A diffusion-weighted imaging based diagnostic system for early detection of prostate cancer. *Journal of Biomedical Science and Engineering*, 6(03):346, 2013.
- [138] X. Liu, D. Langer, M. Haider, T. Van der Kwast, A. Evans, M. Wernick, and I. Yetik. Unsupervised segmentation of the prostate using MR images based on level set with a shape prior. In *Proceedings of Annual International Conference of the IEEE, Engineering in Medicine and Biology Society, (EMBC'09)*, pages 3613–16. IEEE, 2009.
- [139] X. Liu, M. Haider, and I. Yetik. Unsupervised 3D prostate segmentation based on diffusion-weighted imaging MRI using active contour models with a shape prior. *Journal of Electrical and Computer Engineering*, 2011:11, 2011.
- [140] S. Ozer, D. L. Langer, X. Liu, M. Haider, T. van der Kwast, A. Evans, Y. Yang, M. Wernick, and I. Yetik. Supervised and unsupervised methods for prostate cancer segmentation with multispectral MRI. *Medical Physics*, 37(4):1873–1883, 2010.
- [141] X. Liu, D. Langer, M. Haider, Y. Yang, M. Wernick, and I. S. Yetik. Prostate cancer segmentation with simultaneous estimation of Markov random field parameters and class. *IEEE Transaction on Medical Imaging*, 28(6):906–915, 2009.
- [142] H. Veeraraghavan, R. K. Do, D. Reidy, and J. Deasy. Simultaneous segmentation and iterative registration method for computing ADC with reduced artifacts from DW-MRI. *Medical Physics*, 42(5):2249–2260, 2015.
- [143] R. Stephen, A. Jha, D. Roe, T. Trouard, J.-P. Galons, M. Kupinski, G. Frey, H. Cui, S. Squire, M. Pagel, et al. Diffusion MRI with semi-automated segmentation can serve as a restricted predictive biomarker of the therapeutic response of liver metastasis. *Magnetic Resonance Imaging*, 33(10), 2015.
- [144] H. Veeraraghavan and K. Do. Joint segmentation and sequential registration based approach for computing artifact-free ADC maps from multiple DWI-MRI sequences in liver. *Medical Physics*, 40(6):521–521, 2013.
- [145] A. Jha, J. Rodríguez, R. Stephen, and A. Stopeck. A clustering algorithm for liver lesion segmentation of diffusion-weighted MR images. In *Proceedings of IEEE Southwest Symposium on Image Analysis and Interpretation, (SSIAI'10)*, pages 93–96. IEEE, 2010.
- [146] M. Shehata, F. Khalifa, A. Soliman, A. Takieldean, M. Abou El-Ghar, A. Shaffie, A. C. Dwyer, R. Ouseph, A. El-Baz, and K. Robert. 3D diffusion MRI-based CAD

- system for early diagnosis of acute renal rejection. In *Proceedings of IEEE 13th International Symposium on Biomedical Imaging, (ISBI'16)*, pages 1177–1180. IEEE, 2016.
- [147] M. Shehata, F. Khalifa, A. Soliman, E. Hosseini-Asl, M. Abou El-Ghar, A. C. Dwyer, G. Gimel'farb, R. Keynton, and A. El-Baz. Computer-aided diagnostic system for early detection of acute renal transplant rejection using diffusion-weighted MRI. *Medical Image Analysis*, page Submitted, 2016.
- [148] M. Shehata, F. Khalifa, A. Soliman, M. Abou El-Ghar, A. Dwyer, R. Ouseph, and A. El-Baz. Early assessment of acute renal rejection. In *12th Annual Scientific Meeting of American Society for Diagnostics and Interventional Nephrology (AS-DIN)*, Phoenix, Arizona, USA, Feb 19–21, 2016.
- [149] V. Vishnevskiy, C. Stoeck, G. Székely, C. Tanner, and S. Kozerke. Simultaneous denoising and registration for accurate cardiac diffusion tensor reconstruction from MRI. In *Proceedings of International Conference on Medical Image Computing and Computer-Assisted Intervention, (MICCAI'15) (Lecture Notes in Computer Science)*, volume 9349, pages 215–222. Springer, 2015.
- [150] H. G. Jensen, F. Lauze, M. Nielsen, and S. Darkner. Locally orderless registration for diffusion weighted images. In *Proceedings of International Conference on Medical Image Computing and Computer-Assisted Intervention, (MICCAI'15) (Lecture Notes in Computer Science)*, volume 9350, pages 305–312. Springer, 2015.
- [151] M. Shehata, F. Khalifa, A. Soliman, R. Alrefai, M. Abou El-Ghar, A. C. Dwyer, R. Ouseph, and A. El-Baz. A novel framework for automatic segmentation of kidney from DW-MRI. In *Proceedings of IEEE 12th International Symposium on Biomedical Imaging, (ISBI'15)*, pages 951–954. IEEE, 2015.
- [152] M. Shehata, F. Khalifa, A. Soliman, R. Alrefai, M. Abou El-Ghar, A. C. Dwyer, R. Ouseph, and A. El-Baz. A level set-based framework for 3D kidney segmentation from diffusion MR images. In *Proceedings of IEEE 22nd International Conference on Image Processing, (ICIP'15)*, pages 4441–4445. IEEE, 2015.
- [153] M. Shehata, F. Khalifa, A. Soliman, A. Taki Eldeen, M. Abou El-Ghar, T. Eldiasty, A. El-Baz, and R. Keynton. An appearance-guided deformable model for 4D kidney segmentation using diffusion MRI. In X. J. A. El-Baz and T. F. J. Suri, Eds, editors, *Biomedical Image Segmentation: Advances and Trends*, page (In Press). CRC, 2016.
- [154] S. Osher and R. Fedkiw. *Level Set Methods and Dynamic Implicit Surfaces*. Springer Verlag, New York, USA, 2006.
- [155] N. Tustison, B. Avants, P. Cook, Y. Zheng, A. Egan, P. Yushkevich, and J. Gee. N4ITK: Improved N3 bias correction. *IEEE Transactions on Medical Imaging*, 29(6):1310–1320, 2010.
- [156] B. Glocker, N. Komodakis, N. Paragios, and N. Navab. Non-rigid registration using discrete MRFs: Application to thoracic CT images. In *Proceedings of MICCAI Workshop on Evaluation of Methods for Pulmonary Image Registration, (MICCAI'10)*, pages 147–154, 2010.

- [157] F. Wu. The Potts model. *Reviews of Modern Physics*, 54(1):235–268, 1982.
- [158] A. Farag, A. El-Baz, and G. Gimelfarb. Precise segmentation of multi-modal images. *IEEE Transactions on Image Processing*, 15(4):952–968, 2006.
- [159] A. El-Baz, A. Elnakib, F. Khalifa, M. A. El-Ghar, P. McClure, A. Soliman, and G. Gimel’farb. Precise segmentation of 3-D magnetic resonance angiography. *IEEE Transactions on Biomedical Engineering*, 59(7):2019–2029, 2012.
- [160] D. Le Bihan and E. Breton. Imagerie de diffusion in-vivo par résonance magnétique nucléaire. *Comptes-Rendus de l’Académie des Sciences*, 93(5):27–34, 1985.
- [161] V. Vapnik. *The Nature of Statistical Learning Theory*. Springer Science & Business Media, 2013.
- [162] L. Breiman, J. Friedman, C. J. Stone, and R. A. Olshen. *Classification and Regression Trees*. CRC press, 1984.
- [163] L. Breiman. Random forests. *Machine Learning*, 45(1):5–32, 2001.
- [164] P. Cunningham and S. J. Delany. k-nearest neighbour classifiers. *Multiple Classifier Systems*, pages 1–17, 2007.
- [165] R. Rifkin, G. Yeo, and T. Poggio. Advances in learning theory: Methods, models and applications, eds. suykens, horvath, basu, micchelli, and vandewalle, ser. *NATO Science Series III: Computer and Systems Sciences*. Amsterdam: IOS Press, 190, 2003.
- [166] G. Cawley and N. Talbot. On over-fitting in model selection and subsequent selection bias in performance evaluation. *The Journal of Machine Learning Research*, 11:2079–2107, 2010.
- [167] S. Plis, D. Hjelm, R. Salakhutdinov, E. Allen, H. Bockholt, J. Long, H. Johnson, J. Paulsen, J. Turner, and V. Calhoun. Deep learning for neuroimaging: A validation study. *Frontiers in Neuroscience*, 8, 2014.
- [168] G. Hinton and R. Salakhutdinov. Reducing the dimensionality of data with neural networks. *Science*, 313(5786):504–507, 2006.
- [169] H. Song and S.-Y. Lee. Hierarchical representation using NMF. In *Neural Information Processing*, pages 466–473. Springer, 2013.
- [170] D. Erhan, Y. Bengio, A. Courville, P.-A. Manzagol, P. Vincent, and S. Bengio. Why does unsupervised pre-training help deep learning? *The Journal of Machine Learning Research*, 11:625–660, 2010.
- [171] Y. Bengio, A. Courville, and P. Vincent. Representation learning: A review and new perspectives. *IEEE Transactions on Pattern Analysis and Machine Intelligence*, 35(8):1798–1828, 2013.
- [172] Y. Bengio. Learning deep architectures for AI. *Foundations and Trends in Machine Learning*, 2(1):1–127, 2009.

- [173] Y. Bengio, P. Lamblin, D. Popovici, H. Larochelle, et al. Greedy layer-wise training of deep networks. *Advances in Neural Information Processing Systems*, 19:153, 2007.
- [174] E. Hosseini-Asl, J. Zurada, and O. Nasraoui. Deep learning of part-based representation of data using sparse autoencoders with nonnegativity constraints. *IEEE Transactions on Neural Networks and Learning Systems*, pages 1–13, 2015. e-publication ahead of print.
- [175] L. Dice. Measures of the amount of ecologic association between species. *Ecology*, 26(3):297–302, 1945.
- [176] K. Zou, S. Warfield, A. Bharatha, C. Tempany, M. Kaus, S. Haker, W. Wells, F. Jolesz, and R. Kikinis. Statistical validation of image segmentation quality based on a spatial overlap index 1: Scientific reports. *Academic Radiology*, 11(2):178–189, 2004.
- [177] G. Gerig, M. Jomier, and M. Chakos. Valmet: A new validation tool for assessing and improving 3D object segmentation. In *Proceedings of International Conference on Medical Image Computing and Computer Assisted Intervention, (MICCAI'01)*, pages 516–523, 2001.
- [178] J. Zhao, Z. Wang, M. Liu, J. Zhu, X. Zhang, T. Zhang, S. Li, and Y. Li. Assessment of renal fibrosis in chronic kidney disease using diffusion-weighted MRI. *Clinical Radiology*, 69(11):1117–1122, 2014.
- [179] F. Khalifa, A. Soliman, A. Takieldeem, M. Shehata, M. Mostapha, A. Shaffie, R. Ouseph, A. Elmaghraby, and A. El-Baz. Kidney segmentation from CT images using a 3D NMF-guided active contour model. In *Proceedings of IEEE 13th International Symposium on Biomedical Imaging, (ISBI'16)*, pages 432–435. IEEE, 2016.
- [180] M. Shehata, F. Khalifa, E. Hollis, A. Soliman, E. Hosseini-Asl, M. Abou El-Ghar, M. El-Baz, A. Dwyer, A. El-Baz, and R. Keynton. A new non-invasive approach for early classification of renal rejection types using diffusion-weighted MRI. In *Proceedings of IEEE 23rd International Conference on Image Processing, (ICIP'16)*, page (In Press). IEEE, 2016.
- [181] M. Shehata, F. Khalifa, A. Soliman, A. E.-G. Mohamed, D. Amy, G. Gimel'farb, R. Keynton, and A. El-Baz. A promising non-invasive CAD system for kidney function assesment. In *Proceedings of 19th Medical Image Computing and Computer Assisted Intervention, (MICCAI'16)*, page (In Press), Athens, Greece, October 17–21, 2016.
- [182] I. Reda, A. Shalaby, M. Abou El-Ghar, F. Khalifa, M. Elmogy, A. Aboufotouh, E. Hosseini-Asl, A. El-Baz, and R. Keynton. A new NMF-autoencoder based CAD system for early diagnosis of prostate cancer. In *Proceedings of IEEE 13th International Symposium on Biomedical Imaging (ISBI'16)*, pages 1237–1240. IEEE, 2016.

- [183] M. Abou El-Ghar, A. El-Baz, F. Khalifa, A. Elnakib, A. Firjani, and T. El-Diasty. Non-invasive image-based approach for early diagnosis of prostate cancer. In *Proceedings of 18th Symposium of the European Society of Urogenital Radiology, (ESUR'11)*, Dubrovnik, Croatia, October 13–16, 2011.
- [184] A. Firjani, A. Elmaghraby, and A. El-Baz. MRI-based diagnostic system for early detection of prostate cancer. In *Biomedical Sciences and Engineering Conference (BSEC), 2013*, pages 1–4, 2013.
- [185] A. Firjani, A. Elnakib, F. Khalifa, A. El-Baz, G. Gimel'farb, M. Abou El-Ghar, and A. Elmaghraby. A novel 3D segmentation approach for segmenting the prostate from dynamic contrast enhanced MRI using current appearance and learned shape prior. In *Proceedings of IEEE International Symposium on Signal Processing and Information Technology, (ISSPIT'10)*, pages 137–143, Luxor, Egypt, December 15–18, 2010.
- [186] A. Firjani, A. Elnakib, F. Khalifa, G. Gimel'farb, M. A. El-Ghar, A. Elmaghraby, and A. El-Baz. A new 3D automatic segmentation framework for accurate extraction of prostate from diffusion imaging. In *Proceedings of Biomedical Science and Engineering Conference–Image Informatics and Analytics in Biomedicine, (BSEC'11)*, pages 1306–1309, 2011.
- [187] A. Firjani, A. Elnakib, F. Khalifa, G. Gimel'farb, M. A. El-Ghar, J. Suri, A. Elmaghraby, and A. El-Baz. A new 3D automatic segmentation framework for accurate extraction of prostate from DCE-MRI. In *Proceedings of IEEE International Symposium on Biomedical Imaging: From Nano to Macro, (ISBI'11)*, pages 1476–1479, Chicago, Illinois, March 30–April 2, 2011.
- [188] A. Firjani, A. Elnakib, F. Khalifa, G. Gimelfarb, M. Abou El-Ghar, A. Elmaghraby, and A. El-Baz. A diffusion-weighted imaging based diagnostic system for early detection of prostate cancer. *Journal of Biomedical Science and Engineering*, 6(3A):346–356, 2013.
- [189] A. Firjani, F. Khalifa, A. Elnakib, G. Gimel'farb, M. A. El-Ghar, A. Elmaghraby, and A. El-Baz. Non-invasive image-based approach for early detection of prostate cancer. In *Proceedings of Fourth International Conference on Developments in eSystems Engineering, (DeSE'11)*, pages 172–177, Dubai, UAE, December 6–8, 2011.
- [190] A. Firjani, F. Khalifa, A. Elnakib, G. Gimel'farb, M. A. El-Ghar, A. Elmaghraby, and A. El-Baz. 3D automatic approach for precise segmentation of the prostate from diffusion-weighted magnetic resonance imaging. In *Proceedings of IEEE International Conference on Image Processing, (ICIP'11)*, pages 2285–2288, Brussels, Belgium, September 11–14, 2011.
- [191] A. Firjani, F. Khalifa, A. Elnakib, G. Gimel'farb, M. Abou El-Ghar, A. Elmaghraby, and A. El-Baz. A novel image-based approach for early detection of prostate cancer using DCE-MRI. In K. Suzuki, editor, *Computational Intelligence in Biomedical Imaging*, pages 55–82. Springer New York, 2014.

- [192] A. Firjani, F. Khalifa, A. Elnakib, G. Gimel'farb, A. Elmagharby, and A. El-Baz. A novel image-based approach for early detection of prostate cancer. In *Proceedings of IEEE International Conference on Image Processing, (ICIP'12)*, pages 2849–2852, Lake Buena Vista, Florida, September 30–October 3, 2012.
- [193] A. Firjany, A. Elnakib, A. El-Baz, G. Gimel'farb, M. Abou El-Ghar, and A. Elmagharby. Novel stochastic framework for accurate segmentation of prostate in dynamic contrast enhanced MRI. In A. Madabhushi, J. Dowling, P. Yan, A. Fenster, P. Abolmaesumi, and N. Hata, editors, *Prostate Cancer Imaging. Computer-Aided Diagnosis, Prognosis, and Intervention*, volume 6367 of *Lecture Notes in Computer Science*, pages 121–130. Springer Berlin Heidelberg, 2010.
- [194] A. Firjany, A. Elnakib, A. El-Baz, G. Gimelfarb, M. Abou El-Ghar, and A. Elmagharby. Novel stochastic framework for accurate segmentation of prostate in dynamic contrast-enhanced MRI. In *Proceedings of the International Workshop on Prostate Cancer Imaging: Computer-Aided Diagnosis, Prognosis, and Intervention*, pages 121–130, Beijing, China, September 24, 2010.
- [195] P. McClure, F. Khalifa, A. Soliman, M. Abou El-Ghar, G. Gimelfarb, A. Elmagharby, and A. El-Baz. A novel nmf guided level-set for dwi prostate segmentation. *Journal of Computer Science and Systems Biology*, 7:209–216, 2014.
- [196] A. Elnakib, G. M. Beache, G. Gimelfarb, and A. El-Baz. Intramyocardial strain estimation from cardiac cine mri. *International journal of computer assisted radiology and surgery*, 10(8):1299–1312, 2015.
- [197] G. Beache, F. Khalifa, G. Gimel'farb, and A. El-Baz. Fully automated framework for the analysis of myocardial first-pass perfusion MR images. *Medical Physics*, 41(10):1–18, 2014.
- [198] A. Elnakib, G. M. Beache, G. Gimel'farb, and A. El-Baz. A new framework for automated segmentation of left ventricle wall from contrast enhanced cardiac magnetic resonance images. In *Proceeding of International Conference on Image Processing (ICIP'2011)*, pages 2289–2292. IEEE, 2011.
- [199] A. Elnakib, G. Beache, G. G. T. Inanc, and A. El-Baz. Validating a new methodology for strain estimation from cardiac cine MRI. In *Proceedings of International Symposium on Computational Models for Life Science (CMLS'13)*, 2013.
- [200] A. Elnakib, G. Beache, M. Nitzken, G. Gimel'farb, and A. El-Baz. A new framework for automated identification of pathological tissues in contrast enhanced cardiac magnetic resonance images. In *Proceedings of IEEE International Symposium on Biomedical Imaging: From Nano to Macro (ISBI'2011)*, pages 1272–1275. IEEE, 2011.
- [201] A. Elnakib, G. Beache, H. Sliman, G. Gimel'farb, T. Inanc, and A. El-Baz. A novel Laplace-based method to estimate the strain from cine cardiac magnetic resonance images. In *Proceedings of IEEE International Conference on Image Processing (ICIP'2013)*. IEEE, 2013.

- [202] F. Khalifa, G. Beache, A. El-Baz, and G. Gimel'farb. Deformable model guided by stochastic speed with application in cine images segmentation. In *Proceedings of IEEE International Conference on Image Processing, (ICIP'10)*, pages 1725–1728, Hong Kong, September 26–29, 2010.
- [203] F. Khalifa, G. Beache, A. Elnakib, H. Sliman, G. Gimel'farb, K. C. Welch, and A. El-Baz. A new shape-based framework for the left ventricle wall segmentation from cardiac first-pass perfusion MRI. In *Proceedings of IEEE International Symposium on Biomedical Imaging: From Nano to Macro, (ISBI'13)*, pages 41–44, San Francisco, CA, April 7–11, 2013.
- [204] F. Khalifa, G. Beache, A. Elnakib, H. Sliman, G. Gimel'farb, K. Welch, and A. El-Baz. A new nonrigid registration framework for improved visualization of transmural perfusion gradients on cardiac first-pass perfusion MRI. In *Proceedings of IEEE International Symposium on Biomedical Imaging: From Nano to Macro, (ISBI'12)*, pages 828–831, Barcelona, Spain, May 2–5, 2012.
- [205] F. Khalifa, G. Beache, A. Firjani, K. Welch, G. Gimel'farb, and A. El-Baz. A new nonrigid registration approach for motion correction of cardiac first-pass perfusion MRI. In *Proceedings of IEEE International Conference on Image Processing, (ICIP'12)*, pages 1665–1668, Lake Buena Vista, Florida, September 30–October 3, 2012.
- [206] F. Khalifa, G. Beache, G. Gimel'farb, and A. El-Baz. A novel CAD system for analyzing cardiac first-pass MR images. In *Proceedings of IAPR International Conference on Pattern Recognition (ICPR'12)*, pages 77–80, Tsukuba Science City, Japan, November 11–15, 2012.
- [207] F. Khalifa, G. M. Beache, G. Gimel'farb, and A. El-Baz. A novel approach for accurate estimation of left ventricle global indexes from short-axis cine MRI. In *Proceedings of IEEE International Conference on Image Processing, (ICIP'11)*, pages 2645–2649, Brussels, Belgium, September 11–14, 2011.
- [208] F. Khalifa, G. Beache, G. Gimel'farb, G. Giridharan, and A. El-Baz. A new image-based framework for analyzing cine images. In A. El-Baz, U. Acharya, M. Mirmehdi, and J. Suri, editors, *Handbook of Multi Modality State-of-the-Art Medical Image Segmentation and Registration Methodologies*, volume 2, chapter 3, pages 69–98. Springer, New York, 2011.
- [209] F. Khalifa, G. Beache, G. Gimel'farb, G. Giridharan, and A. El-Baz. Accurate automatic analysis of cardiac cine images. *IEEE Transactions on Biomedical Engineering*, 59(2):445–455, 2012.
- [210] F. Khalifa, G. Beache, M. Nitzken, G. Gimel'farb, G. Giridharan, and A. El-Baz. Automatic analysis of left ventricle wall thickness using short-axis cine CMR images. In *Proceedings of IEEE International Symposium on Biomedical Imaging: From Nano to Macro, (ISBI'11)*, pages 1306–1309, Chicago, Illinois, March 30–April 2, 2011.

- [211] M. Nitzken, G. Beache, A. Elnakib, F. Khalifa, G. Gimel'farb, and A. El-Baz. Accurate modeling of tagged cmr 3D image appearance characteristics to improve cardiac cycle strain estimation. In *Proceedings of 19th IEEE International Conference on Image Processing (ICIP'12)*, pages 521–524, Orlando, Florida, USA, September 2012. IEEE.
- [212] M. Nitzken, G. Beache, A. Elnakib, F. Khalifa, G. Gimel'farb, and A. El-Baz. Improving full-cardiac cycle strain estimation from tagged cmr by accurate modeling of 3D image appearance characteristics. In *Proceedings 9th IEEE International Symposium on Biomedical Imaging (ISBI'12)*, pages 462–465, Barcelona, Spain, May 2012. IEEE. (Selected for oral presentation).
- [213] M. Nitzken, A. El-Baz, and G. Beache. Markov-gibbs random field model for improved full-cardiac cycle strain estimation from tagged CMR. *Journal of Cardiovascular Magnetic Resonance*, 14(1):1–2, 2012.
- [214] H. Sliman, A. Elnakib, G. Beache, A. Elmaghraby, and A. El-Baz. Assessment of myocardial function from cine cardiac MRI using a novel 4D tracking approach. *Journal of Computer Science and System Biology*, 7:169–173, 2014.
- [215] H. Sliman, A. Elnakib, G. Beache, A. Soliman, F. Khalifa, G. Gimel'farb, A. Elmaghraby, and A. El-Baz. A novel 4D PDE-based approach for accurate assessment of myocardium function using cine cardiac magnetic resonance images. In *Proceeding of IEEE International Conference on Image Processing (ICIP'14)*, pages 3537–3541, Paris, France, October 27–30, 2014.
- [216] H. Sliman, F. Khalifa, A. Elnakib, G. Beache, A. Elmaghraby, and A. El-Baz. A new segmentation-based tracking framework for extracting the left ventricle cavity from cine cardiac MRI. In *Proceedings of IEEE International Conference on Image Processing, (ICIP'13)*, pages 685–689, Melbourne, Australia, September 15–18, 2013.
- [217] H. Sliman, F. Khalifa, A. Elnakib, A. Soliman, G. Beache, A. Elmaghraby, G. Gimel'farb, and A. El-Baz. Myocardial borders segmentation from cine MR images using bi-directional coupled parametric deformable models. *Medical Physics*, 40(9):1–13, 2013.
- [218] H. Sliman, F. Khalifa, A. Elnakib, A. Soliman, G. Beache, G. Gimel'farb, A. Emam, A. Elmaghraby, and A. El-Baz. Accurate segmentation framework for the left ventricle wall from cardiac cine MRI. In *Proceedings of International Symposium on Computational Models for Life Science, (CMLS'13)*, volume 1559, pages 287–296, Sydney, Australia, November 27–29, 2013.
- [219] A. Soliman, F. Khalifa, N. Dunlap, B. Wang, M. Abou El-Ghar, and A. El-Baz. An iso-surfaces based local deformation handling framework of lung tissues. In *Proceedings of IEEE 13th International Symposium on Biomedical Imaging (ISBI'16)*, pages 1253–1259. IEEE, 2016.
- [220] A. Soliman, F. Khalifa, A. Shaffie, N. Dunlap, B. Wang, A. Elmaghraby, and A. El-Baz. Detection of lung injury using 4D-CT chest images. In *Proceedings of IEEE 13th International Symposium on Biomedical Imaging (ISBI'16)*, pages 1274–1277. IEEE, 2016.

- [221] N. Liu, A. Soliman, G. Gimelfarb, and A. El-Baz. Segmenting kidney DCE-MRI using 1st-order shape and 5th-order appearance priors. In *Proceedings of International Conference on Medical Image Computing and Computer-Assisted Intervention, (MICCAI'15)*, pages 77–84. Springer, 2015.
- [222] B. Abdollahi, A. Civelek, X.-F. Li, J. Suri, and A. El-Baz. PET/CT nodule segmentation and diagnosis: A survey. In L. Saba and J. Suri, editors, *Multi Detector CT Imaging*, chapter 30, pages 639–651. Taylor , Francis, 2014.
- [223] B. Abdollahi, A. El-Baz, and A. A. Amini. A multi-scale non-linear vessel enhancement technique. In *Proceedings of IEEE Annual International Conference on Engineering in Medicine and Biology Society (EMBC'11)*, pages 3925–3929. IEEE, 2011.
- [224] B. Abdollahi, A. Soliman, A. Civelek, X.-F. Li, G. Gimel'farb, and A. El-Baz. A novel gaussian scale space-based joint MGRF framework for precise lung segmentation. In *Proceedings of IEEE International Conference on Image Processing, (ICIP'12)*, pages 2029–2032. IEEE, 2012.
- [225] B. Abdollahi, A. Soliman, A. Civelek, X.-F. Li, G. Gimelfarb, and A. El-Baz. A novel 3D joint MGRF framework for precise lung segmentation. In *Machine Learning in Medical Imaging*, pages 86–93. Springer, 2012.
- [226] A. Ali, A. El-Baz, and A. Farag. A novel framework for accurate lung segmentation using graph cuts. In *Proceedings of IEEE International Symposium on Biomedical Imaging: From Nano to Macro, (ISBI'07)*, pages 908–911. IEEE, 2007.
- [227] A. El-Baz, G. Beache, G. Gimel'farb, K. Suzuki, and K. Okada. Lung imaging data analysis. *International Journal of Biomedical Imaging*, 2013, 2013.
- [228] A. El-Baz, G. Beache, G. Gimel'farb, K. Suzuki, K. Okada, A. Elnakib, A. Soliman, and B. Abdollahi. Computer-aided diagnosis systems for lung cancer: Challenges and methodologies. *International Journal of Biomedical Imaging*, 2013, 2013.
- [229] A. El-Baz, A. Elnakib, M. Abou El-Ghar, G. Gimel'farb, R. Falk, and A. Farag. Automatic detection of 2D and 3D lung nodules in chest spiral CT scans. *International Journal of Biomedical Imaging*, 2013, 2013.
- [230] A. El-Baz, A. Farag, R. Falk, and R. La Rocca. A unified approach for detection, visualization, and identification of lung abnormalities in chest spiral CT scans. In *International Congress Series*, volume 1256, pages 998–1004. Elsevier, 2003.
- [231] A. El-Baz, A. Farag, R. Falk, and R. La Rocca. Detection, visualization and identification of lung abnormalities in chest spiral CT scan: Phase-I. In *Proceedings of International conference on Biomedical Engineering, Cairo, Egypt*, volume 12, 2002.
- [232] A. El-Baz, A. Farag, G. Gimel'farb, R. Falk, M. Abou El-Ghar, and T. Eldiasty. A framework for automatic segmentation of lung nodules from low dose chest CT scans. In *Proceedings of International Conference on Pattern Recognition, (ICPR'06)*, volume 3, pages 611–614. IEEE, 2006.

- [233] A. El-Baz, A. Farag, G. Gimelfarb, R. Falk, and M. Abou El-Ghar. A novel level set-based computer-aided detection system for automatic detection of lung nodules in low dose chest computed tomography scans. *Lung Imaging and Computer Aided Diagnosis*, 10:221–238, 2011.
- [234] A. El-Baz, G. Gimel'farb, M. Abou El-Ghar, and R. Falk. Appearance-based diagnostic system for early assessment of malignant lung nodules. In *Proceedings of IEEE International Conference on Image Processing, (ICIP'12)*, pages 533–536. IEEE, 2012.
- [235] A. El-Baz, G. Gimel'farb, and R. Falk. A novel 3D framework for automatic lung segmentation from low dose CT images. In A. El-Baz and J. Suri, editors, *Lung Imaging and Computer Aided Diagnosis*, chapter 1, pages 1–16. Taylor , Francis, 2011.
- [236] A. El-Baz, G. Gimel'farb, R. Falk, and M. Abou El-Ghar. Appearance analysis for diagnosing malignant lung nodules. In *Proceedings of IEEE International Symposium on Biomedical Imaging: From Nano to Macro (ISBI'10)*, pages 193–196. IEEE, 2010.
- [237] A. El-Baz, G. Gimel'farb, R. Falk, and M. A. El-Ghar. A novel level set-based CAD system for automatic detection of lung nodules in low dose chest CT scans. In A. El-Baz and J. Suri, editors, *Lung Imaging and Computer Aided Diagnosis*, volume 1, chapter 10, pages 221–238. Taylor , Francis, 2011.
- [238] A. El-Baz, G. Gimel'farb, R. Falk, and M. Abou El-Ghar. A new approach for automatic analysis of 3D low dose CT images for accurate monitoring the detected lung nodules. In *Proceedings of International Conference on Pattern Recognition, (ICPR'08)*, pages 1–4. IEEE, 2008.
- [239] A. El-Baz, G. Gimel'farb, R. Falk, and t. . A. b. . P. y. . . v. . . p. . V. o. . I. Abou El-Ghar, Mohamed.
- [240] A. El-Baz, G. Gimel'farb, R. Falk, and M. Abou El-Ghar. A new CAD system for early diagnosis of detected lung nodules. In *Proceedings of IEEE International Conference on Image Processing (ICIP 2007)*, volume 2, pages II–461. IEEE, 2007.
- [241] A. El-Baz, G. Gimel'farb, R. Falk, M. Abou El-Ghar, and H. Refaie. Promising results for early diagnosis of lung cancer. In *Proceedings of IEEE International Symposium on Biomedical Imaging: From Nano to Macro, (ISBI'08)*, pages 1151–1154. IEEE, 2008.
- [242] A. El-Baz, G. L. Gimel'farb, R. Falk, M. Abou El-Ghar, T. Holland, and T. Shaffer. A new stochastic framework for accurate lung segmentation. In *Proceedings of Medical Image Computing and Computer-Assisted Intervention, (MICCAI'08)*, pages 322–330, 2008.
- [243] A. El-Baz, G. L. Gimel'farb, R. Falk, D. Heredis, and M. Abou El-Ghar. A novel approach for accurate estimation of the growth rate of the detected lung nodules. In *Proceedings of International Workshop on Pulmonary Image Analysis*, pages 33–42, 2008.

- [244] A. El-Baz, G. L. Gimel'farb, R. Falk, T. Holland, and T. Shaffer. A framework for unsupervised segmentation of lung tissues from low dose computed tomography images. In *Proceedings of British Machine Vision, (BMVC'08)*, pages 1–10, 2008.
- [245] A. El-Baz, G. Gimelfarb, R. Falk, and M. Abou El-Ghar. 3D MGRF-based appearance modeling for robust segmentation of pulmonary nodules in 3D LDCT chest images. In *Lung Imaging and Computer Aided Diagnosis*, chapter 3, pages 51–63. chapter, 2011.
- [246] A. El-Baz, G. Gimelfarb, R. Falk, and M. Abou El-Ghar. Automatic analysis of 3D low dose CT images for early diagnosis of lung cancer. *Pattern Recognition*, 42(6):1041–1051, 2009.
- [247] A. El-Baz, G. Gimelfarb, R. Falk, M. Abou El-Ghar, S. Rainey, D. Heredia, and T. Shaffer. Toward early diagnosis of lung cancer. In *Proceedings of Medical Image Computing and Computer-Assisted Intervention, (MICCAI'09)*, pages 682–689. Springer, 2009.
- [248] A. El-Baz, G. Gimelfarb, R. Falk, M. Abou El-Ghar, and J. Suri. Appearance analysis for the early assessment of detected lung nodules. In *Lung Imaging and Computer Aided Diagnosis*, chapter 17, pages 395–404. chapter, 2011.
- [249] A. El-Baz, F. Khalifa, A. Elnakib, M. Nitzken, A. Soliman, P. McClure, G. Gimel'farb, and M. A. El-Ghar. A novel approach for global lung registration using 3D Markov Gibbs appearance model. In *Proceedings of International Conference Medical Image Computing and Computer-Assisted Intervention, (MICCAI'12)*, pages 114–121, Nice, France, October 1–5, 2012.
- [250] A. El-Baz, M. Nitzken, A. Elnakib, F. Khalifa, G. Gimel'farb, R. Falk, and M. A. El-Ghar. 3D shape analysis for early diagnosis of malignant lung nodules. In *Proceedings of International Conference Medical Image Computing and Computer-Assisted Intervention, (MICCAI'11)*, pages 175–182, Toronto, Canada, September 18–22, 2011.
- [251] A. El-Baz, M. Nitzken, G. Gimelfarb, E. Van Bogaert, R. Falk, M. Abou El-Ghar, and J. Suri. Three-dimensional shape analysis using spherical harmonics for early assessment of detected lung nodules. In *Lung Imaging and Computer Aided Diagnosis*, chapter 19, pages 421–438. chapter, 2011.
- [252] A. El-Baz, M. Nitzken, F. Khalifa, A. Elnakib, G. Gimel'farb, R. Falk, and M. A. El-Ghar. 3D shape analysis for early diagnosis of malignant lung nodules. In *Proceedings of International Conference on Information Processing in Medical Imaging, (IPMI'11)*, pages 772–783, Monastery Irsee, Germany (Bavaria), July 3–8, 2011.
- [253] A. El-Baz, M. Nitzken, E. Vanbogaert, G. Gimel'Farb, R. Falk, and M. Abou El-Ghar. A novel shape-based diagnostic approach for early diagnosis of lung nodules. In *Biomedical Imaging: From Nano to Macro, 2011 IEEE International Symposium on*, pages 137–140. IEEE, 2011.

- [254] A. El-Baz, P. Sethu, G. Gimel'farb, F. Khalifa, A. Elnakib, R. Falk, and M. Abou El-Ghar. Elastic phantoms generated by microfluidics technology: Validation of an imaged-based approach for accurate measurement of the growth rate of lung nodules. *Biotechnology Journal*, 6(2):195–203, 2011.
- [255] A. El-Baz, P. Sethu, G. Gimel'farb, F. Khalifa, A. Elnakib, R. Falk, and M. A. El-Ghar. A new validation approach for the growth rate measurement using elastic phantoms generated by state-of-the-art microfluidics technology. In *Proceedings of IEEE International Conference on Image Processing, (ICIP'10)*, pages 4381–4383, Hong Kong, September 26–29, 2010.
- [256] A. El-Baz, P. Sethu, G. Gimel'farb, F. Khalifa, A. Elnakib, R. Falk, M. A. El-Ghar, and J. Suri. Validation of a new imaged-based approach for the accurate estimating of the growth rate of detected lung nodules using real CT images and elastic phantoms generated by state-of-the-art microfluidics technology. In A. El-Baz and J. Suri, editors, *Handbook of Lung Imaging and Computer Aided Diagnosis*, volume 1, chapter 18, pages 405–420. Taylor & Francis, New York, 2011.
- [257] A. El-Baz, A. Soliman, P. McClure, G. Gimel'farb, M. Abou El-Ghar, and R. Falk. Early assessment of malignant lung nodules based on the spatial analysis of detected lung nodules. In *Proceedings of IEEE International Symposium on Biomedical Imaging: From Nano to Macro, (ISBI'12)*, pages 1463–1466. IEEE, 2012.
- [258] A. El-Baz, S. E. Yuksel, S. Elshazly, and A. Farag. Non-rigid registration techniques for automatic follow-up of lung nodules. In *Proceedings of Computer Assisted Radiology and Surgery, (CARS'05)*, volume 1281, pages 1115–1120. Elsevier, 2005.
- [259] A. El-Baz and J. Suri. *Lung Imaging and Computer Aided Diagnosis*. CRC Press, 2011.
- [260] A. El-Bazl, A. Farag, R. Falk, and R. La Rocca. Automatic identification of lung abnormalities in chest spiral CT scans. In *Proceedings of IEEE International Conference on Acoustics, Speech, and Signal Processing, (ICASSP'03)*, volume 2, pages II–261. IEEE, 2003.
- [261] A. Farag, A. El-Baz, G. Gimel'farb, and R. Falk. Detection and recognition of lung abnormalities using deformable templates. In *Proceedings of the 17th International Conference on Pattern Recognition, (ICPR'04)*, volume 3, pages 738–741. IEEE, 2004.
- [262] A. Farag, A. El-Baz, G. Gimelfarb, R. Falk, M. Abou El-Ghar, T. Eldiasty, and S. Elshazly. Appearance models for robust segmentation of pulmonary nodules in 3D Idct chest images. In *Proceedings of Medical Image Computing and Computer-Assisted Intervention (MICCAI'06)*, pages 662–670. Springer, 2006.
- [263] A. Farag, A. El-Baz, G. Gimelfarb, R. Falk, and S. Hushek. Automatic detection and recognition of lung abnormalities in helical CT images using deformable templates. In *Proceedings of Medical Image Computing and Computer-Assisted Intervention, (MICCAI'04)*, pages 856–864. Springer, 2004.

- [264] E. Hosseini-Asl, J. Zurada, and A. El-Baz. Lung segmentation based on nonnegative matrix factorization. In *Proceedings of IEEE International Conference on Image Processing (ICIP'14)*, pages 877–881. IEEE, 2014.
- [265] M. Kondapaneni, M. Nitzken, E. Bogaert, G. Gimelfarb, R. Falk, M. Abou El-Ghar, and A. El-Baz. A novel shape-based diagnostic approach for early diagnosis of lung nodules. *CHEST Journal*, 140(4.MeetingAbstracts):655A–655A, 2011.
- [266] A. Soliman, F. Khalifa, A. Alansary, G. Gimel'farb, and A. El-Baz. Performance evaluation of an automatic MGRF-based lung segmentation approach. In *Proceedings of International Symposium on Computational Models for Life Sciences, (CMLS'13)*, volume 1559, page 323, 2013.
- [267] A. Soliman, F. Khalifa, A. Alansary, G. Gimel'farb, and A. El-Baz. Segmentation of lung region based on using parallel implementation of joint MGRF: Validation on 3D realistic lung phantoms. In *Proceedings of International Symposium on Biomedical Imaging: From Nano to Macro, (ISBI'13)*, pages 864–867. IEEE, 2013.
- [268] M. Ismail, R. Keynton, M. Mostapha, A. ElTanboly, M. Casanova, G. Gimel'farb, and A. El-Baz. Studying autism spectrum disorder with structural and diffusion magnetic resonance imaging: A survey. *Frontiers in Human Neuroscience*, 10, 2016.
- [269] M. Ismail, A. Soliman, A. ElTanboly, A. Switala, M. Mahmoud, F. Khalifa, G. Gimel'farb, M. F. Casanova, R. Keynton, and A. El-Baz. Detection of white matter abnormalities in mr brain images for diagnosis of autism in children. In *Proceedings of IEEE 13th International Symposium on Biomedical Imaging (ISBI'16)*, pages 6–9. IEEE, 2016.
- [270] A. Alansary, A. Soliman, F. Khalifa, A. Elnakib, M. Mostapha, M. Nitzken, M. Casanova, and A. El-Baz. MAP-based framework for segmentation of MR brain images based on visual appearance and prior shape. *MIDAS J*, 1:1, 2013.
- [271] A. Alansary, A. Soliman, M. Nitzken, F. Khalifa, A. Elnakib, M. Mostapha, M. Casanova, and A. El-Baz. An integrated geometrical and stochastic approach for accurate infant brain extraction. In *Proceedings of IEEE International Conference on Image Processing (ICIP'14)*, pages 3542–3546. IEEE, 2014.
- [272] M. Casanova, A. El-Baz, M. Mott, G. Mannheim, H. Hassan, R. Fahmi, J. Giedd, J. Rumsey, A. Switala, and A. Farag. Reduced gyral window and corpus callosum size in autism: Possible macroscopic correlates of a minicolumnopathy. *Journal of Autism and Developmental Disorders*, 39(5):751–764, 2009.
- [273] M. Casanova, A. El-Baz, and A. Switala. Laws of conservation as related to brain growth, aging, and evolution: symmetry of the minicolumn. *Frontiers in Neuroanatomy*, 5, 2011.
- [274] M. Casanova, A. El-Baz, E. Vanbogaert, P. Narahari, and A. Switala. A topographic study of minicolumnar core width by lamina comparison between autistic subjects and controls: Possible minicolumnar disruption due to an anatomical element in-common to multiple laminae. *Brain Pathology*, 20(2):451–458, 2010.

- [275] M. Casanova, A. El-Baz, E. Vanbogaert, P. Narahari, and J. Trippe. Minicolumnar width: comparison between supragranular and infragranular layers. *Journal of Neuroscience Methods*, 184(1):19–24, 2009.
- [276] M. Casanova, A. El-Baz, S. Kamat, B. Dombroski, F. Khalifa, A. Elnakib, A. Soliman, A. Allison-McNutt, and A. Switala. Focal cortical dysplasias in autism spectrum disorders. *Acta Neuropathologica Communications*, 1(1):67, 2013.
- [277] M. Casanova, A. El-Baz, and J. Suri. *Imaging the Brain in Autism*. Springer, 2013.
- [278] M. Casanova, A. Farag, E.-B. Ayman, M. Meghan, H. Hassan, R. Fahmi, and A. Switala. Abnormalities of the gyral window in autism: A macroscopic correlate to a putative minicolumnopathy. *Journal of Special Education and Rehabilitation*, 7(1-2), 2006.
- [279] A. Chowdhury, A. Rudra, M. Sen, A. Elnakib, and A. El-Baz. Cerebral white matter segmentation from MRI using probabilistic graph cuts and geometric shape priors. In *ICIP*, pages 3649–3652, 2010.
- [280] B. Dombroski, A. Switala, A. El-Baz, and M. Casanova. Gyral window mapping of typical cortical folding using MRI. *Translational neuroscience*, 2(2):142–147, 2011.
- [281] B. Dombroski, M. Nitzken, A. Elnakib, F. Khalifa, A. El-Baz, and M. Casanova. Cortical surface complexity in a population-based normative sample. *Translational Neuroscience*, 5(1):17–24, 2014.
- [282] A. El-Baz, M. Casanova, G. Gimel’farb, M. Mott, and A. Switala. An MRI-based diagnostic framework for early diagnosis of dyslexia. *International Journal of Computer Assisted Radiology and Surgery*, 3(3-4):181–189, 2008.
- [283] A. El-Baz, M. Casanova, G. Gimel’farb, M. Mott, A. Switala, E. Vanbogaert, and R. McCracken. A new CAD system for early diagnosis of dyslexic brains. In *Proceedings of International Conference on Image Processing (ICIP’2008)*, pages 1820–1823. IEEE, 2008.
- [284] A. El-Baz, M. Casanova, G. Gimel’farb, M. Mott, and A. Switala. Autism diagnostics by 3D texture analysis of cerebral white matter gyrifications. In *Proceedings of International Conference on Medical Image Computing and Computer-Assisted Intervention (MICCAI’2007)*, pages 882–890. Springer, 2007.
- [285] A. El-Baz, M. Casanova, G. Gimel’farb, M. Mott, and A. Switwala. A new image analysis approach for automatic classification of autistic brains. In *Proceedings of IEEE International Symposium on Biomedical Imaging: From Nano to Macro (ISBI’2007)*, pages 352–355. IEEE, 2007.
- [286] A. El-Baz, A. Farag, G. Gimel’farb, M. Abou El-Ghar, and T. Eldiasty. Probabilistic modeling of blood vessels for segmenting mra images. In *ICPR (3)*, pages 917–920, 2006.

- [287] A. El-Baz, A. Farag, G. Gimelfarb, M. Abou El-Ghar, and T. Eldiasty. A new adaptive probabilistic model of blood vessels for segmenting mra images. In *Proceedings of Medical Image Computing and Computer-Assisted Intervention (MICCAI'06)*, volume 4191, pages 799–806. Springer, 2006.
- [288] A. El-Baz, A. Farag, G. Gimelfarb, and S. Hushek. Automatic cerebrovascular segmentation by accurate probabilistic modeling of tof-mra images. In *Medical Image Computing and Computer-Assisted Intervention (MICCAI'05)*, pages 34–42. Springer, 2005.
- [289] A. El-Baz, A. Farag, A. Elnakib, M. Casanova, G. Gimel'farb, A. Switala, D. Jordan, and S. Rainey. Accurate automated detection of autism related corpus callosum abnormalities. *Journal of Medical Systems*, 35(5):929–939, 2011.
- [290] A. El-Baz, A. G. G. M. Casanova G. Gimel'farb M. Mott El-Baz, M. Mott, A. Switala, E. Vanbogaert, and R. McCracken. Dyslexia diagnostics by 3D texture analysis of cerebral white matter gyrifications. In *Proceedings of International Conference on Pattern Recognition (ICPR'2008)*, pages 1–4. IEEE, 2008.
- [291] G. G.-M. M. A. El-Baz, M. Casanova and A. Switala. A new image-based diagnostic framework for early diagnosis of dyslexic brains. In *Proceedings of of Computer Assisted Radiology and Surgery (CARS'08)*, pages 46–47, 2008.
- [292] A. Elnakib, A. El-Baz, M. Casanova, G. Gimel'farb, and A. Switala. Image-based detection of corpus callosum variability for more accurate discrimination between dyslexic and normal brains. In *Proceedings of IEEE International Symposium on Biomedical Imaging: From Nano to Macro (ISBI'2010)*, pages 109–112. IEEE, 2010.
- [293] A. Elnakib, A. El-Baz, M. F. Casanova, G. Gimel'farb, and A. Switala. Image-based detection of corpus callosum variability for more accurate discrimination between autistic and normal brains. In *Proceedings of IEEE International Conference on Image Processing (ICIP'2010)*, pages 4337–4340. IEEE, 2010.
- [294] A. Elnakib, A. El-Baz, M. Casanova, and A. Switala. Dyslexia diagnostics by centerline-based shape analysis of the corpus callosum. In *Proceedings of International Conference on Pattern Recognition (ICPR'2010)*, pages 261–264. IEEE, 2010.
- [295] A. Elnakib, M. Casanova, G. Gimel'farb, A. Switala, and A. El-Baz. Dyslexia diagnostics by 3-D shape analysis of the corpus callosum. *IEEE Transactions on Information Technology in Biomedicine*, 16(4):700–708, 2012.
- [296] A. Elnakib, M. Casanova, G. Gimel'farb, A. Switala, and A. El-Baz. Autism diagnostics by centerline-based shape analysis of the corpus callosum. In *Proceedings of IEEE International Symposium on Biomedical Imaging: From Nano to Macro (ISBI'2011)*, pages 1843–1846. IEEE, 2011.
- [297] A. Elnakib, M. Casanova, G. Gimel'farb, and A. El-Baz. Autism diagnostics by 3D shape analysis of the corpus callosum. In K. Suzuki, editor, *Machine Learning in*

Computer-aided Diagnosis: Medical Imaging Intelligence and Analysis, chapter 15, pages 315–335. IGI Global, Berlin, 2012.

- [298] R. Fahmi, A. Elbaz, H. Hassan, A. Farag, and M. Casanova. Structural MRI-based discrimination between autistic and typically developing brain. In *Proceedings of Computer Assisted Radiology and Surgery (CARS'2007)*, pages 24–26, 2007.
- [299] A. Farag, R. Fahmi, M. Casanova, A. Abdel-Hakim, H. Abd El-Munim, and A. El-Baz. Robust neuroimaging-based classification techniques of autistic vs. typically developing brain. In *Deformable Models*, chapter 16, pages 535–566. Springer, 2007.
- [300] M. Casanova, A. El-Baz, A. Elnakib, A. Switala, E. Williams, D. Williams, N. Minshew, and T. Conturo. Quantitative analysis of the shape of the corpus callosum in patients with autism and comparison individuals. *Autism*, 15(2):223–238, 2011.
- [301] M. Casanova, A. El-Baz, A. Elnakib, J. Giedd, J. Rumsey, E. Williams, and A. Switala. Corpus callosum shape analysis with application to dyslexia. *Translational Neuroscience*, 1(2):124–130, 2010.
- [302] M. Casanova, A. El-Baz, J. Giedd, J. Rumsey, and A. Switala. Increased white matter gyral depth in dyslexia: Implications for corticocortical connectivity. *Journal of Autism and Developmental Disorders*, 40(1):21–29, 2010.
- [303] M. Mostapha, A. Alansary, A. Soliman, F. Khalifa, M. Nitzken, R. Khodeir, M. Casanova, and A. El-Baz. Atlas-based approach for the segmentation of infant DTI MR brain images. In *Proceedings of IEEE 11th International Symposium on Biomedical Imaging (ISBI'14)*, pages 1255–1258. IEEE, 2014.
- [304] M. Mostapha, A. Soliman, F. Khalifa, A. Elnakib, A. Alansary, M. Nitzken, M. F. Casanova, and A. El-Baz. A statistical framework for the classification of infant DT images. In *Proceedings of IEEE International Conference Image Processing (ICIP'14)*, pages 2222–2226. IEEE, 2014.
- [305] M. Nitzken, M. Casanova, G. Gimel'farb, A. Elnakib, F. Khalifa, A. Switala, and A. El-Baz. 3D shape analysis of the brain cortex with application to dyslexia. In *Proceedings of 18th IEEE International Conference on Image Processing (ICIP)'11*, pages 2657–2660, Brussels, Belgium, September 2011. IEEE.
- [306] M. Nitzken, M. Casanova, G. Gimel'farb, F. Khalifa, A. Elnakib, A. Switala, and A. El-Baz. 3D shape analysis of the brain cortex with application to autism. In *Proceedings of IEEE International Symposium on Biomedical Imaging: From Nano to Macro (ISBI'13)*, pages 1847–1850, Chicago, Illinois, USA, March 2011. IEEE.
- [307] M. Nitzken, M. Casanova, F. Khalifa, G. Sokhadze, and A. El-Baz. Shape-based detection of cortex variability for more accurate discrimination between autistic and normal brains. In A. El-Baz, R. Acharya, A. Laine, and J. Suri, editors, *Handbook of Multi-Modality State-of-the-Art Medical Image Segmentation and Registration Methodologies*, volume 2, chapter 7, pages 161–185. Springer Verlag, New York, March 2011.

- [308] M. Nitzken, M. Casanova, and A. El-Baz. Spharm analysis of the brain cortex for diagnosing dyslexia. In *Proceedings of IEEE 11th International Symposium on Biomedical Imaging (ISBI'14)*, Beijing, China, April 2014. IEEE.
- [309] M. Nitzken, G. Casanova, Mand Gimelfarb, T. Inanc, J. Zurada, and A. El-Baz. Shape analysis of the human brain: a brief survey. *Journal of Biomedical and Health Informatics*, 18(4):1337–1354, 2014.
- [310] A. Rudra, M. Sen, A. Chowdhury, A. Elnakib, and A. El-Baz. 3D graph cut with new edge weights for cerebral white matter segmentation. *Pattern Recognition Letters*, 32(7):941–947, 2011.
- [311] E. Williams, A. El-Baz, M. Nitzken, A. Switala, and M. Casanova. Spherical harmonic analysis of cortical complexity in autism and dyslexia. *Translational Neuroscience*, 3(1):36–40, 2012.
- [312] T. Fawcett. An introduction to ROC analysis. *Pattern Recognition Letters*, 27(8):861–874, 2006.

APPENDIX

A. Evaluating Segmentation Accuracy

Performance of the proposed segmentation was evaluated by using three accuracy metrics: (i) the Dice similarity coefficient (DSC) [175, 176], (ii) the 95-percentile modified Hausdorff distance (MHD) [177], and (iii) the absolute kidney volume difference (AKVD), which are detailed below.

The Dice similarity coefficient (DSC), shown in Figure 23, measures the relative overlap between the segmented and ground truth kidney in terms of true positive (TP), false positive (FP), and false negative (FN) absolute volumes of the correctly segmented kidney voxels, background voxels segmented as the kidney, and kidney voxels segmented as the background, respectively:

$$DSC = \frac{2TP}{2TP + FP + FN}; \quad 0 \leq DSC \leq 1 \quad (\text{A-1})$$

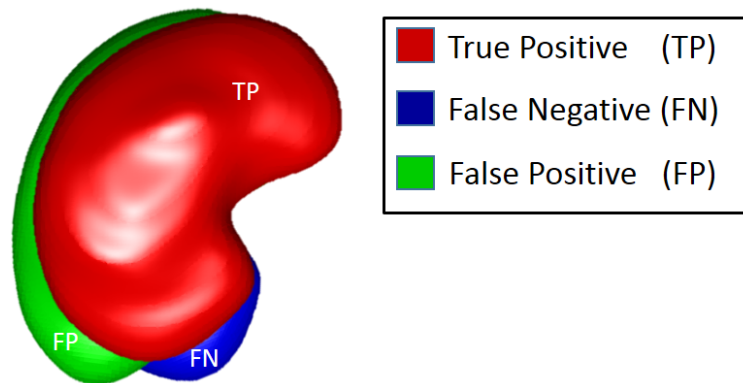


FIGURE 23: 2D illustration of segmentation errors calculation between the segmented and ground truth objects for the DSC determination.

The higher the DSC, the better the segmentation (zero and unit DSC indicate no overlap and ideal overlap, respectively).

The modified Hausdorff distance (MHD), shown in Figure 24, measures the largest surface-to-surface distance between the segmented and ground truth kidney borders. The conventional asymmetric Hausdorff distance (HD) [177] from a set of points A_1 to a set of points A_2 is defined as the maximum Euclidean distance $d(\mathbf{p}_1, \mathbf{p}_2)$ between the points \mathbf{p}_1 of A_1 to their nearest points \mathbf{p}_2 in A_2 :

$$HD(A_1, A_2) = \max_{\mathbf{p}_1 \in A_1} \left\{ \min_{\mathbf{p}_2 \in A_2} \{d(\mathbf{p}_1, \mathbf{p}_2)\} \right\} \quad (\text{A-2})$$

Generally $HD(A_1, A_2) \neq HD(A_2, A_1)$. Therefore, the symmetric bidirectional HD (BHD) is defined as $BHD(A_1, A_2) = \max\{HD(A_1, A_2), HD(A_2, A_1)\}$.

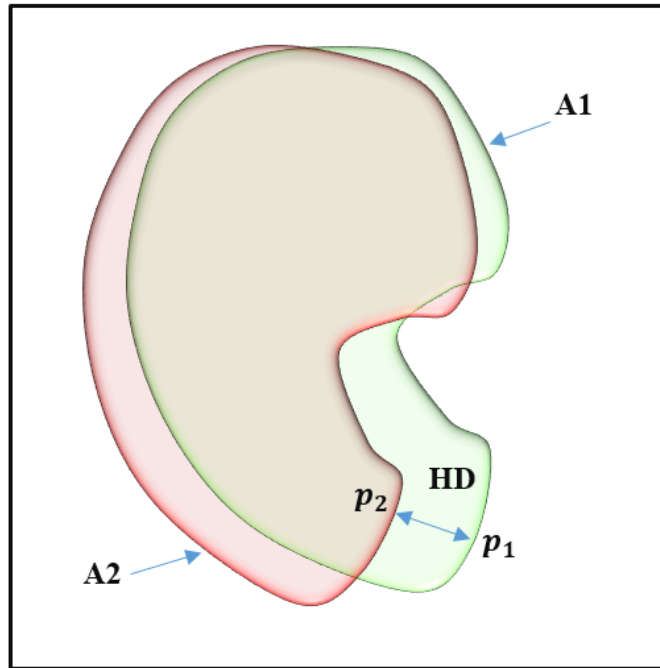


FIGURE 24: 2D schematic illustration for the HD calculation.

To escape possible outliers, affecting both the HD and BHD, and measure more robustly the segmentation accuracy, the 95-percentile BHD, called the modified HD (MHD), is used in this paper. In this case, the maximum distance in Equation (A-2) is replaced with the 95-percentile of all the point-to-point distances $d(\mathbf{p}_1, \mathbf{p}_2)$.

The absolute kidney volume difference (AKVD), shown in Figure 25, measures the relative volumetric difference between the segmented and ground truth kidney (their absolute volumes are equal to $V_{\text{segm}} = TP + FN$ and $V_{\text{true}} = TP + FP$, respectively):

$$AKVD = 100 \frac{|V_{\text{segm}}| - |V_{\text{true}}|}{|V_{\text{true}}|} \% \quad (\text{A-3})$$

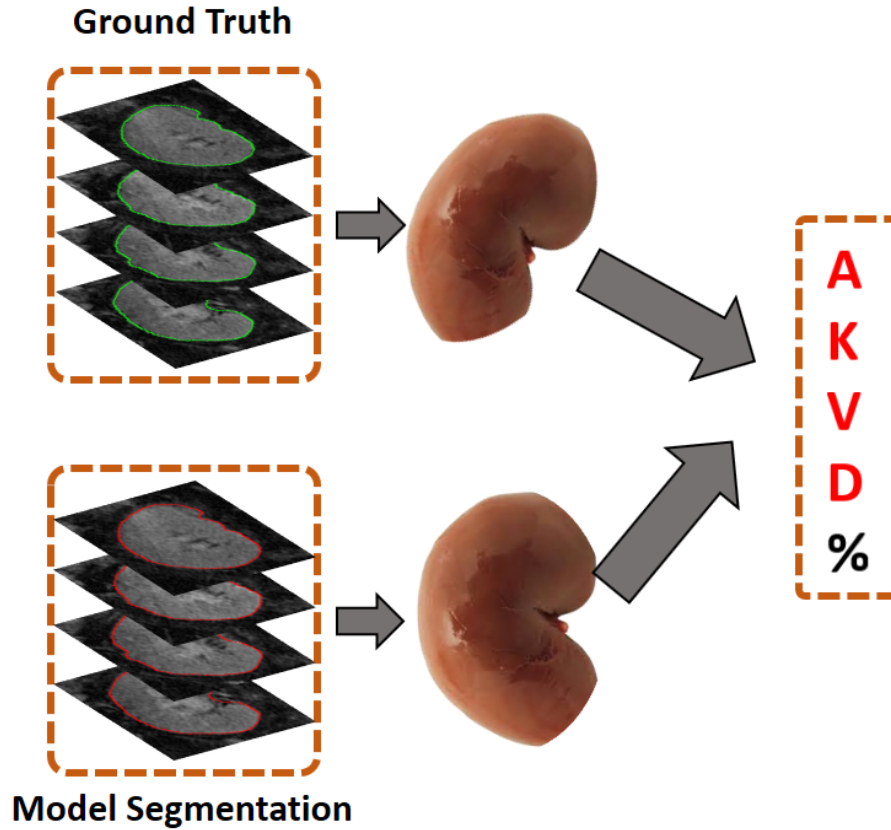


FIGURE 25: 3D schematic illustration for the AKVD estimation.

The receiver operating characteristic (ROC) [312] is an alternative metric to further test the classification accuracy and robustness of a CAD system compared to other classifiers. The sensitivity and discriminability of a classifier is evaluated in a Cartesian plane of relative true positive and false positive rates by its ROC curve for different operating points, e.g., various decision thresholds. The area under the ROC curve (AUC) characterizes the classification accuracy, namely, the probability of the correct renal transplant status detection for a randomly chosen pair of patients.

B. List of Abbreviations

TABLE 8: List of abbreviations that have been used in this thesis.

Abbreviation	Full Definition
CKD	Chronic Kidney Disease
NKF	National Kidney Foundation
GFR	Glomerular Filtration Rate
MRI	Magnetic Resonance Imaging
UNOS	United Network of Organ Sharing
AKR	Acute Kidney Rejection
ATN	Acute Tubular Necrosis
ITox	Immunosuppressive Toxicity
VI	Viral Infection
CT	Computed Tomography
US	Ultrasound
PI	Pulsatility Index
RI	Resistance Index
PD	Power Doppler
CD	Color Doppler
CE	Contrast Enhanced
IGF	Immediate Graft Function
SGF	Slow Graft Function
DGF	Delayed Graft Function
DKT	Dual Kidney Transplantation
SKT	Single Kidney Transplantation
AR	Acute Rejection
ROI	Regions of Interest

continued on the next page ...

Table 8 – continued from the previous page

Abbreviation	Full Definition
CP	Cortical perfusion
SCr	Serum Creatinine
USCM	Ultrasound Contrast Media
CEUS	Contrast Enhanced Ultrasound
CES	Contrast Enhanced Sonography
CDUS	Contrast Enhanced UltraSonography
RBF	Renal Blood Flow
AKI	Acute Kidney Injury
TIC	Time-Intensity Curves
ATPI	Arrival Time Parametric Imaging
IT	Inflow Time
RisT	Rising Time
AT	Arrival Time
TTP	Time to Peak
DCE-MRI	Dynamic Contrast Enhanced MRI
RBF	Renal Plasma Flow
NGF	Normalized Gradient Field
LS-SVM	Least Square Support Vector Machine
MTT	Mean Transit Time
BOLD-MRI	Blood Oxygen Level Dependant MRI
R2*	Apparent Relaxation Rate
CR2*	Cortical R2*
MR2*	Medullary R2*
MCR2*	Medullary to Cortical R2*
SNR	Signal-to-Noise Ratio

continued on the next page ...

Table 8 – continued from the previous page

Abbreviation	Full Definition
DW-MRI	Diffusion-Weighted MRI
ADC	Apparent Diffusion Coefficient
CRCL	Creatinine Clearance
IniGF	Initial Graft Function
ARTR	Acute Renal Transplant Rejection
TD	True Diffusion
ACR	Acute Cellular Rejection
CAD	Computer-Aided Diagnostic
SPCR	Serum Plasma Creatinine
CDF	Cumulative Distribution Function
NCAE	Non-negativity Constrained Autoencoder
NMF	Nonnegative Matrix Factorization
SVM	Support Vector Machine
RVM	Relevant Vector Machine
MRF	Markov Random Field
MHD	Modified Housdorff Distance
MGRF	Markov-Gibbs random field
FGM	Finite Gaussian Mixture
LCDG	Linear Combination of Discrete Gaussians
PDF	Probability Distribution Function
SNCAE	Stacked Non-negativity Constrained Autoencoder
ANN	Artificial Neural Network
RF	Random Forest
DT	Decision Tree
kNN	K-nearest Neighbor

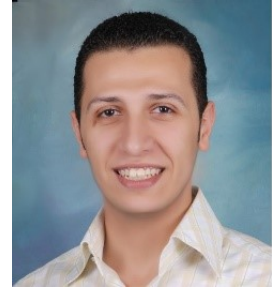
continued on the next page ...

Table 8 – continued from the previous page

Abbreviation	Full Definition
AE	Auto-encoder
KL	Kullback-Leibler
DSC	Dice Similarity Coefficient
AKVD	Absolute Kidney Volume Difference
BHD	Bidirectional Hausdorff Distance
NBT	Naive Bayes Tree
MCC	Multi-class Classifier
RT	Random Tree
ROC	Receiver Operating Characteristic
AUC	Area Under the Curve

CURRICULUM VITAE

Mohamed Nazih Shehata
Paul C. Lutz Hall, Room # 309
BioImaging Laboratory
Department of Bioengineering
University of Louisville, Louisville, KY, USA
University E-mail: *mnsheh01@louisville.edu*
Personal E-mail: *eng.mohamednazeeh@hotmail.com*
Office: (502) 852-4032
Cell: (502) 797-1805



Current Research Interest

I am a graduate student at Electrical and Computer Engineering Department at the University of Louisville, Louisville, KY, USA. My general research interests are in digital image processing, medical imaging, and computer vision. In August 2014, I have joined the BioImaging Lab and have actively been working on developing a novel computer-aided diagnostic (CAD) systems for early detection of acute renal transplant rejection from 4D diffusion-weighted MRIs. This research includes developing new computer aided diagnostic systems, image modeling, and image segmentation and registration.

Education

- 2016 M.Sc., Electrical and Computer Engineering Department, Speed School of Engineering, University of Louisville, Louisville, KY 40292
M.Sc. Thesis: *A Non-Invasive Diagnostic System for Early Assessment of Acute Renal Transplant Rejection-* Prof. Ayman S. El-Baz, Thesis Advisor.
GPA = 4.0 (*Graduation date: Summer 2016*)
- 2009 B.Sc., Computers Engineering and Control Systems, Mansoura University, Mansoura 35516, Egypt.
Sr. Project: *Remote Controlling of Moving Objects Via Mobile or Fixed Phones-* Prof. Aly El-Desouky, Project Supervisor.
GPA = 4.0 (*Graduated with **excellence with honor** and ranked the **first** in a class of 200*)

Experience

- Fall 2014–Present Graduate Research Assistant, BioImaging laboratory, Department of Bioengineering, University of Louisville, Louisville, KY 40292, USA.
- 2010–2014 Graduate Research Assistant, Department of Computers Engineering and Control Systems, Mansoura University, Mansoura 35516, Egypt.

Teaching/Administration Experience

Assist in teaching, laboratory demonstration, conducting tutorials, grading, and senior graduation projects of the following Electrical Engineering undergraduate courses:

Place	Course Subject	Semester/Year
Mansoura University	Artificial Neural Networks Artificial Intelligence Machine Learning Fuzzy Control Systems Advanced Control Systems Digital Control Systems Computer Architecture Computer Maintenance	2010-2014
Mansoura University	Supervision support for an undergraduate final project (Smart Modern Automatic Control Restaurant trend) using PAC	2012-2013
Mansoura University	Summer trainer for undergraduate student on Matlab basic tools and PAC controller	2011-2012
Mansoura University	Supervision support for an undergraduate final project (Smart Gate) using image processing techniques; specifically, face recognition	2010-2011

Professional Affiliations and Memberships

- Young Professional Member, Institute of Electrical and Electronics Engineers (IEEE).
- Member, IEEE Signal Processing (SPS) Society.
- Member, IEEE Engineering in Medicine and Biology (EMBS) Society.
- Member, IEEE Biometrics Council.
- Member, IEEE Sensors Council.
- Member, IEEE Nanotechnology Council.
- Member, IEEE Electronic Design Automation Council.
- Member, IEEE Cloud Computing Community.
- Member, IEEE Systems Council.
- Member, Egyptian Engineers Syndicate, Electrical Engineering.

Awards and Recognition

- *Merit of Excellence Certificate* from Graduate Student Council (GSC) at the University of Louisville, in the area of community engagement in Graduate Student Regional Research Conference (GSRRC), April 2016.
- *One of The Best 39 papers* in the International Symposium on Biomedical Imaging: From Nano to Macro, Prague, Czech Republic, April 16–20, 2016 (ISBI'16).
- *IEEE Signal Processing Society (SPS) Travel Award 2015* to attend the IEEE International Conference on Image processing, Quebec City, Canada, September 27–30, 2015 (ICIP'15).
- *GSC at the University of Louisville Travel Award 2015*.
- *Theobald Scholarship Award* in the Electrical and Computer Engineering Department, Speed school of Engineering, University of Louisville, 2015.
- *Discretionary Certificate* for distinct participation in student activities (Robocon Competition supervision), 2009–2010.

- *Higher Education Enhancement Project Fund Discretionary Certificate* for distinct students in the Department of Communications and Electronics Engineering for Excellent grade ranked **third** in the second undergraduate year of education, Mansoura University , 2005–2006.

Class Work Grade

A total of **30** credit hours in Electrical Engineering and Bioengineering subjects with a cumulative *GPA of 4*. Particular course concentration has been in medical image analysis and machine learning.

Research Activities

- Image modeling, 2D and 3D image segmentation and registration.
- Development of computer-aided diagnostic (CAD) system using diffusion-weighted magnetic resonance imaging (DW-MRI) for the early assessment of acute renal transplant rejection.
- Development of a CAD system for the early detection of different types of kidney rejection using DW-MRIs.
- Development of a cascaded two-stage CAD system for differentiating nonrejection renal transplants from transplanted kidneys with abnormalities using DW-MRIs and then, classifying abnormal kidney transplants into early rejection and other kidney diseases including: tubular inflammation, acute tubular injury, graft amyloidosis, and acute tubular necrosis.
- Assisted in grants writing and preparing primary results for the BioImaging Lab, University of Louisville.

Out of Reach Connectivity

- I have trained one of the high school students during Fall and Spring of 2015 and we had two published conference papers.
- I have trained one of the middle school students during Fall and Spring of 2016 and we had one published conference paper.

Publications

During Fall 2014–Summer 2016, I have authored or co-authored 2 journal articles, 1 book chapter, 6 peer-reviewed conference papers, 1 abstract in proceedings. The first article have been submitted to Medical Image Analysis Journal (5-year impact factor 4.950); current status (under-review) and the second one to be submitted to The Egyptian Journal of Radiology and Nuclear Medicine. The conference papers were reported as top-rank international conferences in medical imaging, image processing, and pattern recognition e.g., MICCAI, ISBI, and ICIP with acceptance rate less than 30%.

• Journal Articles (Total = 2)

1. **M. Shehata**, F. Khalifa, A. Soliman, E. Hossini-Asl, M. Abou El-Ghar, A. C. Dwyer, G. Gimel'farb, R. Keynton, and A. El-Baz, "Computer-Aided Diagnostic System for Early Detection of Acute Renal Transplant Rejection Using Diffusion-Weighted MRI," *Medical Image Analysis*, 2016 (under-review).
2. E. Hollis, **M. Shehata**, F. Khalifa, M. Abou El-Ghar, T. El-Diasty, G. Gimel'farb, and A. El-Baz, "Towards Non-invasive Diagnostic Techniques for Early Detection of Acute Renal Rejection: A Review," *The Egyptian Journal of Radiology and Nuclear Medicine*, 2016 (to-be-submitted).

• Book Chapters (Total = 1)

1. **M. Shehata**, F. Khalifa, A. Soliman, A. Taki Eldeen, M. Abou El-Ghar, T. El-Diasty, A. El-Baz, and R. Keynton, “An appearance-guided deformable model for 4D kidney segmentation using diffusion MRI,” *Biomedical Image Segmentation: Advances and Trends*, A. El-Baz, X. Jiang, and J. Suri, Eds, Taylor & Francis, 2016, ch. 12, pp. 269–283.

• **Peer-Reviewed Conference Proceedings (Total = 6)**

1. **M. Shehata**, F. Khalifa, A. Soliman, R. Alrefai, M. Abou El-Ghar, A. C. Dwyer, R. Ouseph, and A. El-Baz, “A Novel Framework for Automatic Segmentation of Kidney from DW-MRI,” In: *Proceedings of IEEE International Symposium on Biomedical Imaging: From Nano to Macro (ISBI’15)*, New York, USA, April 16–19, 2015, pp. 951–954.
2. **M. Shehata**, F. Khalifa, A. Soliman, R. Alrefai, M. Abou El-Ghar, A. C. Dwyer, R. Ouseph, and A. El-Baz, “A Level Set-Based Framework for 3D Kidney Segmentation from Diffusion MR Images,” In: *Proceedings of International Conference on Image Processing (ICIP’15)*, Quebec, Canada, September 27–30, 2015, pp. 4441–4445.
3. **M. Shehata**, F. Khalifa, A. Soliman, A. Takieldeen, M. Abou El-Ghar, A. Shaffie, A. C. Dwyer, R. Ouseph, A. El-Baz, and R. Keynton, “3D Diffusion MRI-Based CAD System for Early Diagnosis of Acute Renal Rejection,” In: *Proceedings of IEEE International Symposium on Biomedical Imaging: From Nano to Macro (ISBI’16)*, Prague, Czech Republic, April 13–16, 2016, pp. 1177–1180. (***Selected as One of the Best 39 papers from around 340 accepted papers***).
4. F. Khalifa, A. Soliman, A. Takieldeen, **M. Shehata**, M. Mostapha, A. Shaffie, R. Ouseph, A. Elmaghraby, and A. El-Baz, “Kidney Segmentation from CT Images Using A 3D NMF-Guided Active Contour Model,” In: *Proceedings of IEEE International Symposium on Biomedical Imaging: From Nano to Macro (ISBI’16)*, Prague, Czech Republic, April 13–16, 2016, pp. 432–435.
5. **M. Shehata**, F. Khalifa, E. Hollis, A. Soliman, E. Hosseini-Asl, M. Abou El-Ghar,

M. El-Baz, A. C. Dwyer, A. El-Baz, and R. Keynton, “A New Non-Invasive Approach for Early Classification of Renal Rejection Types Using Diffusion-Weighted MRI,” In: *Proceedings of International Conference on Image Processing (ICIP’16)*, Phoenix, Arizona, USA, September 25–28, 2016 (In Press). (*Selected for Oral Presentation*).

6. **M. Shehata**, F. Khalifa, A. Soliman, M. Abou El-Ghar, A. C. Dwyer, G. Gimel’farb, R. Keynton, and A. El-Baz, “A Promising Non-Invasive CAD System for Kidney Function Assessment,” In: *Proceedings of Medical Image Computing and Computer Assisted Intervention (MICCAI’16)*, Athens, Greek, October 17–21, 2016 (In Press).

- **Abstracts Published in Proceedings (Total = 1)**

1. **M. Shehata**, F. Khalifa, A. Soliman, M. Abou El-Ghar, A. C. Dwyer, R. Ouseph, and A. El-Baz, “Early Assessment of Acute Renal Rejection,” In: *Proceedings of 12th Annual Scientific Meeting of American Society for Diagnostics and Interventional Nephrology (ASDIN’16)*, Phoenix, Arizona, USA, February 19–21, 2016.

- **Patents and Disclosures (Total = 1)**

1. A. El-Baz, A. C. Dwyer, R. Ouseph, F. Khalifa, A. Soliman, **M. Shehata**, “COMPUTER AIDED DIAGNOSTIC SYSTEM FOR CLASSIFYING KIDNEYS,” *US Non-Provisional Patent Publication 20150286786*, October 8th, 2015.

Graduate Advisor

Dr. Ayman S. El-Baz, Department of Bioengineering, University of Louisville, KY.

Personal Skills, Hobbies, and Activities

- Active, self-motivated, ability to work alone and in a team, ability to work under pressure, Internet browsing, reading, swimming, and football.